Computer Modeling and Simulations of Biological Systems

by

© **Abd Al-Aziz A. Abu-Saleh**

A thesis submitted to the School of Graduate Studies in partial fulfillment of the requirements for the degree of Doctor of Philosophy.

Department of Chemistry

Memorial University

August 2021

St. John's, Newfoundland and Labrador, Canada

Abstract

Computational chemistry plays a central role in chemistry and biophysics. By leveraging supercomputers, theoretical chemists can elucidate the atomic resolution of biological systems and solve chemical problems. This thesis consists of two parts: First, I worked on the challenging problem of understanding the enzymatic modification of aminoglycoside antibiotics by means of molecular modeling and simulation techniques. Aminoglycoside antibiotics were among the first tools of bacterial warfare found and used clinically and still have a central role in the treatment of acute bacterial infections. However, aminoglycoside modifying enzymes such as aminoglycoside phosphotransferases alter aminoglycoside antibiotics and, therefore, inactivate the drug. I elucidated the phosphorylation mechanism using quantum mechanical methods and molecular dynamics simulations. The results provide a new understanding of the aminoglycoside phosphotransferase catalytic function, which agrees with the available experimental data. Second, due to the emergence of the severe acute repository syndrome coronavirus SARS-CoV-2 in late 2019, I pivoted my efforts to try to gain insight into the rational design of potent inhibitors that target key proteins (e.g., the spike protein and the main protease) of SARS-CoV-2 coronavirus. The structure-based and ligand-based drug design were used to find effective therapeutics of SARS-CoV-2 disease. Interestingly, our results suggest several promising approved and bioactive inhibitors of SARS-CoV-2 main protease. Moreover, a comprehensive protocol including molecular docking, molecular dynamics simulations, standard binding energy calculations, and steered molecular dynamics simulations was performed to accelerate the discovery of compounds that would strongly bind to SARS-CoV-2 spike receptor binding domain (RBD), therefore, blocking viral attachment to the host cell. The discovered top hits identify critical interactions associated with the spike RBD protein, which in turn disrupt binding of the RBD protein to the host cell.

Dedicated to the soul of my mother.

Acknowledgements

I would like to take the moment to thank all the people who have supported me and provided me a great assistance along the way of this journey.

First, I thank my supervisor, Prof. Raymond A. Poirier, for teaching and mentoring me to be a good researcher and scientist. Your insightful and constructive feedback pushed me to sharpen my ideation and guided my work to a higher level. I am very grateful for your continuous support, encouragement, and invaluable advice during my study. Second, I thank my co-superviser Dr. Mansour Almatarneh for his great support and help during my study.

Also, I would like to thank my supervisory committee members: Dr. Christopher Flinn and Dr. Mansour Almatarneh, for their feedback and suggestions of my research work. I also acknowledge my thesis examiners: Prof. James Gauld, Prof. Yuming Zhao, and Dr. Karl Jobst, who provided useful suggestions to embellish the final version of this thesis. Besides, I thank Dr. Arpita Yadav for the productive collaboration, the help, and the feedback throughout my study.

To all former and present members of the computational and theoretical chemistry group at Poirier's lab, I am thankful for the beautiful memories and insightful discussions we had. Special mention to Ibrahim Awad (PhD, 2019), Ahmad Alrawashdeh (PhD, 2015), and Matyas Csongor (PhD candidate).

Special thanks to Ernest Awoonor-Williams (PhD, 2020), who has been very friendly and thoughtful person. I have really enjoyed the time we spent discussing about research. Your expertise about enhanced MD simulations are very honorable. You was a good workout buddy as well. I hope you all the best in your life.

My dear wife, I am so glad of having you. Thank you for your unending support

and love. I am highly appreciative for all efforts you have done for me to reach my goal.

To my father and siblings: Thank you so much for supporting me with no limits. I love you all. I hope to see you soon and have wonderful times together.

I am thankful for Dr. Liqin Chen scholarships in Chemistry and the School of Graduate Studies of Memorial University for funding. I am also grateful to Compute Canada for computer time.

Last but not least, I thank all colleagues, lab instructors, technicians, faculty and staff members of the Chemistry Department.

Statement of contribution

The first chapter gives a general demo of aminoglycoside modifying enzymes and key proteins of SARS-CoV-2. Moreover, a theoretical background is also provided including molecular docking, molecular dynamics simulations and quantum mechanical calculations. I was responsible for writing all sections of this chapter.

The second chapter provides a detailed mechanistic study of the phosphorylation of kanamycin A antibiotic catalyzed by the aminoglycoside phosphotransferase enzyme. This chapter was adapted with permission from: Abu-Saleh, A.A.A.; Sharma,S.; Yadav, A.; Poirier, R.A. Role of Asp190 in the Phosphorylation of the Antibiotic Kanamycin Catalyzed by the Aminoglycoside Phosphotransferase Enzyme: A Combined QM:QM and MD Study. *J. Phys. Chem. B*, **2020**, *124*, 3494–3504. I was responsible for writing all sections of this chapter. I received guidance and assistant from Prof. Poirier and Dr. Yadav.

The third chapter provides an *in silico* study for the discovery of potent inhibitors against SARS-CoV-2's main protease. This chapter was adapted with permission from: Abu-Saleh, A.A.A.; Sharma, S.;Yadav, A.; Poirier, R.A. Discovery of potent inhibitors for SARS-CoV-2's main protease by ligand-based/structure-based virtual screening, MD simulations, and binding energy calculations. *Phys. Chem. Chem. Phys.*, **2020**, *22*, 23099–23106. I was responsible for writing all sections of this chapter. I received guidance and feedback from Prof. Poirier and Dr. Yadav.

The forth chapter provides an *in silico* study for the discovery of potent inhibitors against SARS-CoV-2's spike protein. This chapter was adapted from: Abu-Saleh, A.A.A.; Yadav, A.; Poirier, R.A. Accelerating the Discovery of the Beyond Rule of Five Compounds That Have High Affinities Toward SARS-CoV-2 Spike RBD. *ChemRxiv*, **2020**, DOI: 10.26434/chem-rxiv.14130353.v2. I was responsible for writing all

sections of this chapter. I received guidance and feedback from Prof. Poirier and Dr. Yadav.

The fifth chapter gives a brief summary of the results presented herein and future work. I was responsible for writing this chapter.

Table of contents

List of tables

List of figures

"The purpose of computing is insight not numbers."

—Richard Hamming

1 Introduction

1.1 General Background

1.1.1 Modification of Aminoglycoside Antibiotics

Antibiotics are natural or synthetic molecules that kill or inhibit the growth of microorganisms. The first antibiotic, penicillin, was discovered by Alexander Fleming in 1928. In 1945, Fleming, Chain, and Florey were jointly awarded the Nobel Prize in physiology or medicine for their discovery of penicillin and its curative effect in various infectious diseases. In 1952, Waksman was awarded the Nobel Prize in physiology or medicine for his discovery of streptomycin, the first aminoglycoside antibiotic effective against tuberculosis. Later, several other aminoglycosides were also developed including neomycin, kanamycin, amikacin, gentamycin, and tobramycin.

Aminoglycosides contain many hydroxyl and amino groups, which facilitate the binding of aminoglycosides to the negatively charged phosphate groups and the base pairs of the 16S ribosomal RNA at the A-site of the 30S subunit (see Figure 1.1)

This receptor–ligand binding event prevents the binding of the 30S subunit to the 50S subunit, and hence, inhibits protein synthesis of bacteria.

Antibiotic resistance is one of the biggest global health challenges nowadays. It is progressively threatening our ability to treat bacterial infectious diseases as well as to perform several medical treatment and procedures, including surgery, transplants, and chemotherapy, which need operative antibiotics to solve problems. In good time, awareness is becoming more intense, and actions to deal with antibiotic resistance are discussed globally. As with other antibiotics, the emergence of aminoglycoside-resistance bacteria raises serious complications.[1] The main mechanisms of bacterial resistance consist of preventing antibiotics accumulation inside the bacterial cell via efflux pumps or changes in membrane permeability, chemical modification of the target of the antibiotic (e.g. mutations occur at the A-site region of the ribosomal RNA), and enzymatic modifications of the drug.[2] The latter is the most important one due to its predominance among different pathogenic bacteria. Three families of aminoglycoside modifying enzymes classification depends on the reactions that they catalyze: (1) aminoglycoside acetyltransferases (AACs); (2) aminoglycoside nucleotidyltransferases(ANTs); (3) aminoglycoside phosphotransferases (APHs). Figure 1.2 illustrates the modification reactions of kanamycin A antibiotic catalyzed by aminoglycoside modifying enzymes. AACs catalyze the acetylation of the aminoglycoside's amino groups by the acetyl-CoA cofactor. On the other hand, ANTs catalyze the adenylylation of the aminoglycoside's hydroxyl groups by the ATP, forming the adenylylated aminoglycoside and the inorganic pyrophosphate. Many of aminoglycoside modifying enzymes are able to confer bacterial resistance, particularly, APHs that show high levels of resistance.[3] Chapter 2 is aimed mainly at understanding the enzymatic modification of aminoglycoside antibiotics that are catalyzed by APHs. Information about the modification of aminoglycosides by AACs and ANTs is provided in the references.[4–7]

Phosphorylation of the aminoglycosides by APHs introduces a negative charge to the antibiotic molecule, which results in a dramatic change in their potency to bind to the A-site of the bacterial ribosome. In Chapter 2, I will focus on the phosphorylation of kanamycin A that is catalyzed by APHs in atomistic details.

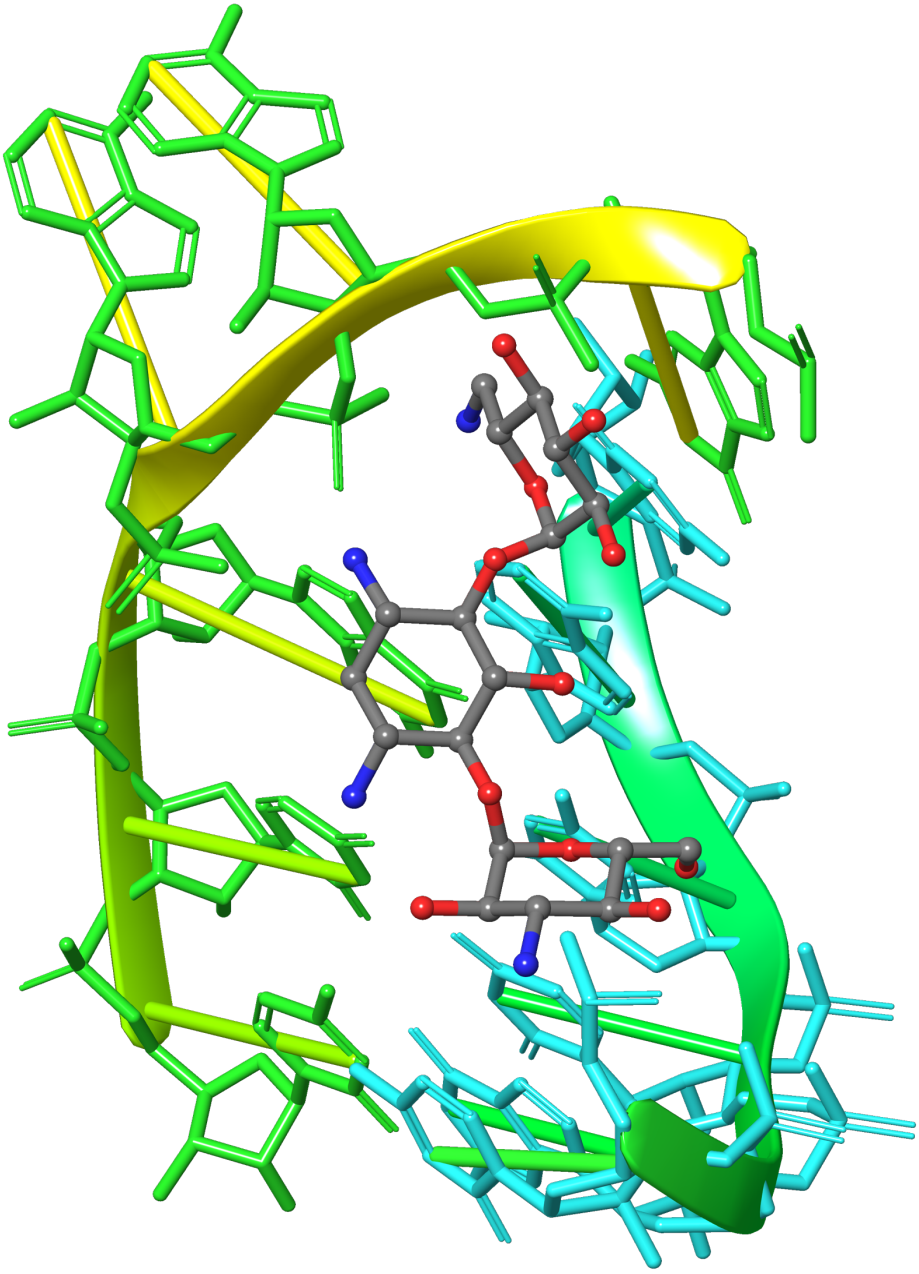

Figure 1.1: The binding site of kanamycin A with the 16S ribosomal RNA (PDB code: 2ESI).

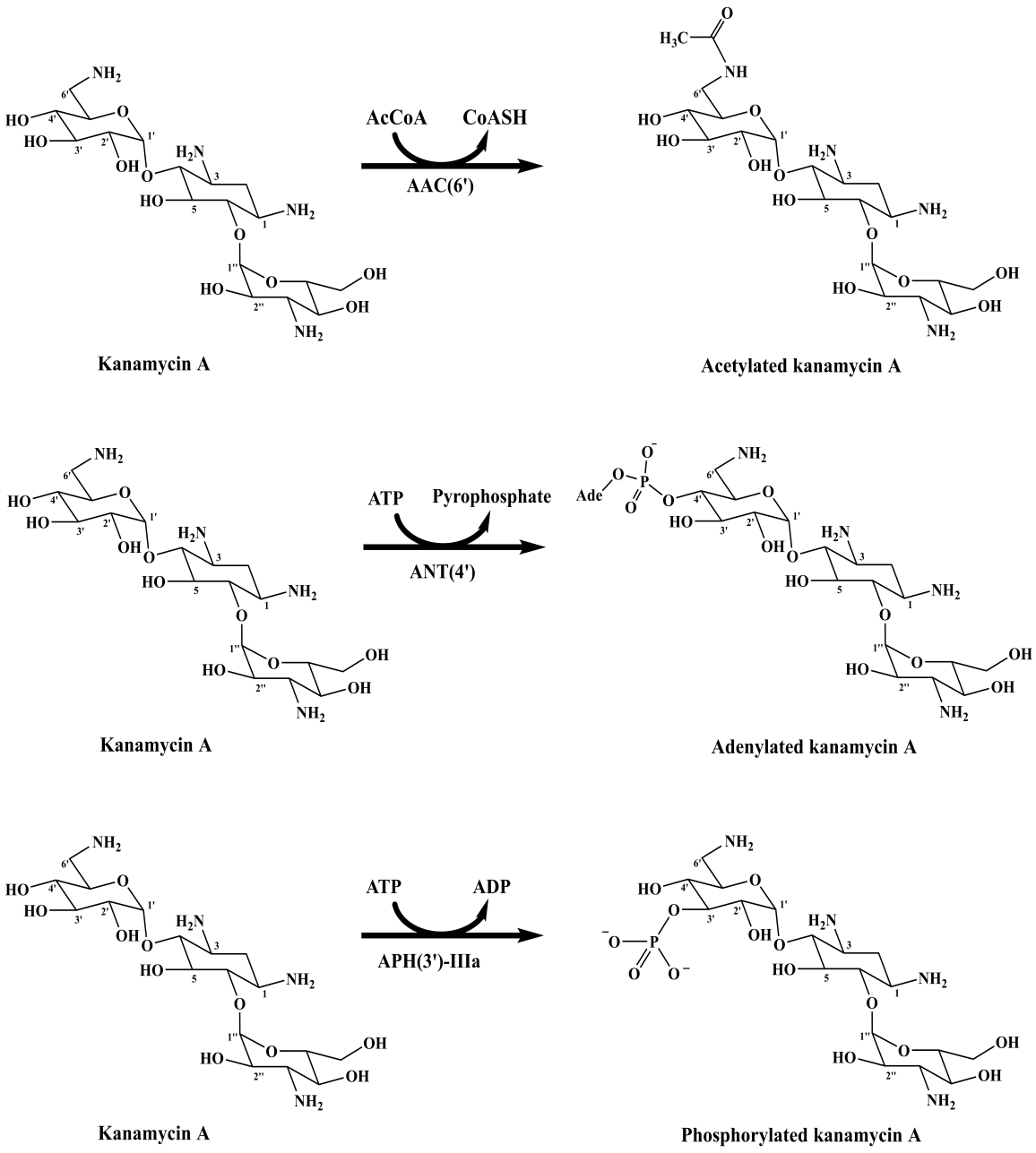

Figure 1.2: Kanamycin A modification reactions catalyzed by aminoglycoside modifying enzymes: AAC (top), ANT (middle), and APH (bottom).

1.2 Key Proteins of SARS-CoV-2

Coronaviruses are spherical-like shape enveloped viruses containing a single-stranded RNA genome. The outer surface of the viral membrane is decorated with glycoprotein spikes, which results in crown-like appearance of the coronaviruses. There are four different groups of coronaviruses designated alpha-, beta-, gamma-, and delta-coronavirus (i.e., α-CoV, β-CoV, γ-CoV, and δ-CoV).[8] Coronaviruses that are able to infect humans are classified under the groups α-CoV and β-CoV, whereas coronaviruses classified under γ-CoV and δ-CoV groups are mostly known to spread among avians and pigs.[9]

The beta group of coronaviruses includes severe acute respiratory syndrome (SARS-CoV) that emerged in 2003, Middle East respiratory syndrome (MERS) that emerged in 2012, and the newly emerged SARS-CoV-2 in late 2019. Similar to both MERS-CoV and SARS-CoV, SARS-CoV-2 attacks the lower respiratory system, which results in severe viral pneumonia.[10] Other human coronaviruses such as HKU1, HCoV-OC43, HCoV-NL63, or HCoV-229E, generally cause mild upper respiratory diseases.[11] The genome of SARS-CoV-2 shares about 82% sequence identity with SARS-CoV and more than 90% for key enzymes and structural proteins.[12, 13] However, it has been reported that SARS-CoV-2 is more contagious/transmissible than SARS-CoV.[14]

The coronavirus genome is typically in the order of 5′-ORF1a-ORF1b-S-E-M-N-3′.[9] The overlapping open reading frames ORF1a and ORF1b cover about two-thirds of the viral genome, which encode 16 non-structural proteins (NSPs). The last one-third of the genome encodes the structural proteins, namely, spike (S), envelope (E), membrane (M) and nucleocapsid (N). The viral genome also contains a number of ORFs coding for accessory proteins that are not important for virus replication, but may have a function in pathogenesis.[15] Figure 1.3 shows the structural and non-structural proteins of SARS-CoV-2. Although many proteins encoded by the SARS-CoV-2 genome can be considered as drug targets, some proteins play a key rule in the viral life-cycle. For instance, the spike protein, the main protease, the papain-like protease, and the RNA-dependent RNA-polymerase are considered as potential druggable targets. Chapter 3 is mainly focused on the computational design of potent inhibitors for the main protease of SARS-CoV-2. This will include ligand-based and structure-based molecular screening, molecular dynamics simulations, and relative binding energy calculations. In Chapter 4, computational discovery protocol

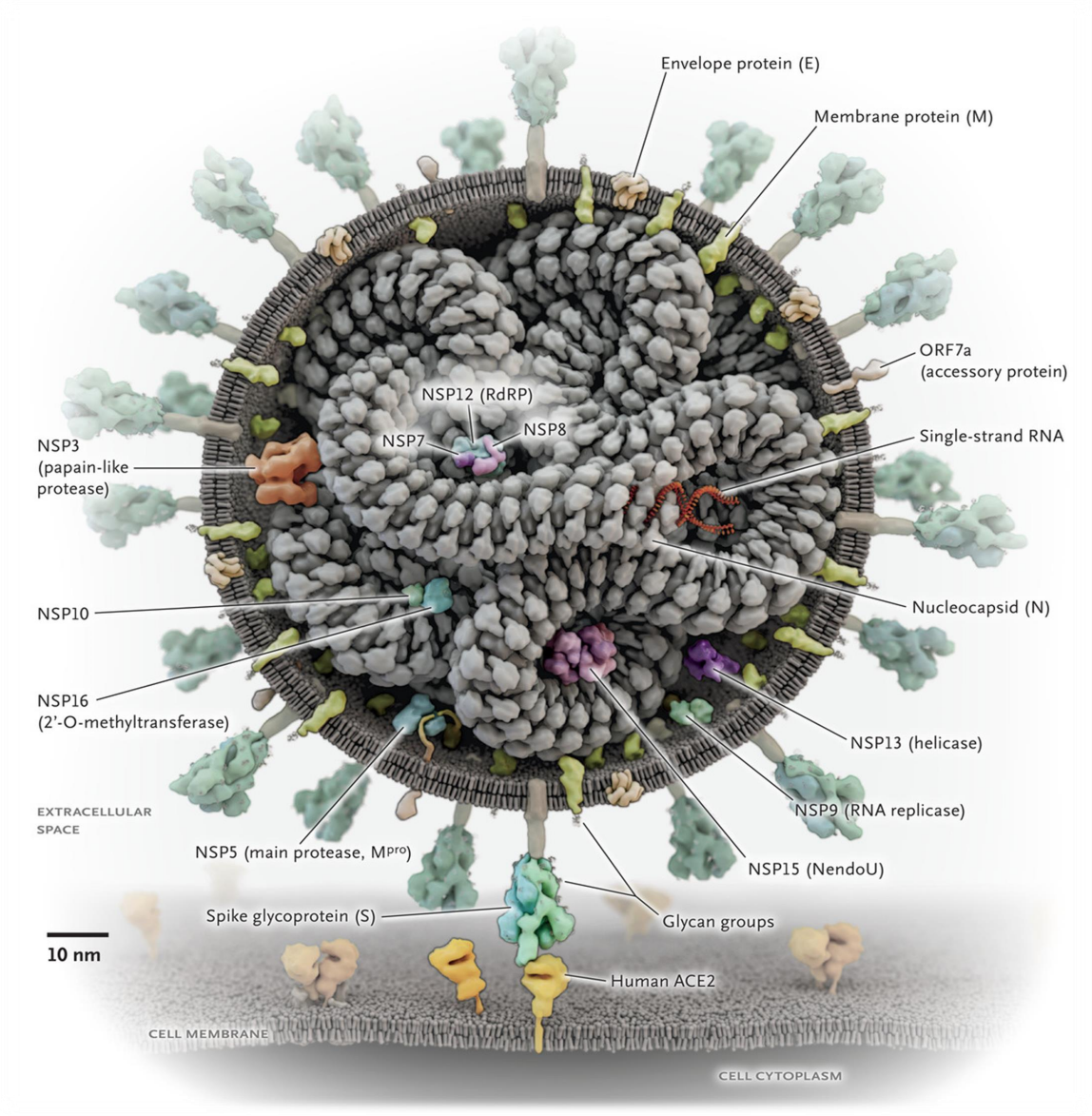

Figure 1.3: Representation of the SARS-CoV-2 virion and its proteins. Reproduced with permission from (*N. Engl. J. Med.* 2020, 382, 2261–2264). Copyright Massachusetts Medical Society.

including molecular docking, molecular dynamics simulations, absolute binding energy calculations, and steered molecular dynamics simulations for the discovery of relatively large compounds that would bind to the SARS-CoV-2 spike protein will be presented.

1.3 Theoretical Background

1.3.1 Molecular Docking

Molecular docking is one of the most widely used virtual screening methods to find potential compounds from the chemical space for drug discovery and development projects. The main goal of molecular docking is to predict the ligand bound conformations (i.e., poses) and their binding affinities to the receptor target of interest. Sampling algorithms and energy scoring functions are the tools used for generating and assessing the ligand conformations in the active site of the receptor. Many molecular docking software packages were developed based on the scoring functions and searching/sampling algorithms. Molecular docking methods can be categorized as systematic search techniques (e.g., exhaustive search, fragmentation, and conformational ensemble), stochastic methods (e.g., Monte Carlo and swarm optimization methods), and simulations methods (e.g., energy minimization methods). More details about the scoring functions and sampling algorithms are provided in the references.[16, 17] Generally, the receptor-ligand docking scores consist of contributions from the van der Waals, electrostatic, hydrogen bonding, and desolvation components. For instance, the scoring function of Autodock can be written as,[18]

$$\begin{aligned}\Delta G_{scoring} = W_{vdW} \sum_{i,j} \left(\frac{A_{ij}}{r_{ij}^{12}} - \frac{B_{ij}}{r_{ij}^{6}} \right) + W_{hbond} \sum_{i,j} E(t) \left(\frac{C_{ij}}{r_{ij}^{12}} - \frac{D_{ij}}{r_{ij}^{10}} \right) \\ + W_{elec} \sum_{i,j} \frac{q_i q_j}{\varepsilon(r_{ij}) r_{ij}} + W_{tor} N_{tor} + W_{sol} \sum_{i,j} (S_i V_j + S_j V_i) e^{(r_{ij}^2 2\sigma^2)}\end{aligned} \tag{1.1}$$

where the five W terms on the right-hand side of the equation are weighted coefficients empirically calculated using linear regression analysis from a set of receptor–ligand bound systems with known binding constants. i represents ligand atoms and j represents receptor atoms. The first three terms of the equation represent the contributions

of a Lennard–Jones potential, a directional hydrogen bonding term (where $E(t)$ is a directional weight based on the angle, t, between the probe and the target atom), and Coulombic electrostatic potential. Conformational degrees of freedom of the ligand is proportional to the number of sp^3 bonds in the ligand (N_{tor}). The last term represents the desolvation contribution.

1.3.2 Quantum Mechanical (QM) Calculations

The evolution of quantum mechanics started in 1925. The depiction of the particle and wave nature of electrons by Louis de Broglie led Erwin Schrödinger in 1926 to interpret electrons as standing waves that close around the nucleus.[19] The time-independent Schrödinger equation can be written as

$$\hat{H}(r;R)\Psi(r;R) = E\Psi(r;R) \tag{1.2}$$

where, $\hat{H}(r;R)$ represents the total Hamiltonian operator, $\Psi(r;R)$ represents the total wavefunction, E is the total energy of the system, while r and R stand for the electronic and nuclear coordinates, respectively. The non-relativistic Hamiltonian operator is the sum of the kinetic energy operators of the electrons and nuclei, and potential energy operators of the electron-electron repulsion, electron-nuclear attraction, and the nuclear-nuclear repulsion, as illustrated in the following equation:

$$\hat{H} = -\frac{1}{2}\sum_{i=1}^{N}\nabla_i^2 - \frac{1}{2}\sum_{A=1}^{M}\nabla_A^2 - \sum_{i=1}^{N}\sum_{A=1}^{M}\frac{Z_A}{r_{iA}} + \sum_{i=1}^{N}\sum_{j>i}^{N}\frac{1}{r_{ij}} + \sum_{A=1}^{M}\sum_{B>A}^{M}\frac{Z_A Z_B}{R_{AB}} \tag{1.3}$$

where N and M are the number of electrons and nuclei, respectively. i and j represent the electrons. A and B represent the nuclei. Z is the atomic number of the nuclei. r_{iA} and r_{ij} are the electron-nucleus and electron-electron distances, respectively.

Unfortunately, the time-independent Schrödinger equation can be solved only for one-electron systems. One of the main goals of molecular quantum mechanics is solving the time-independent Schrödinger equation, and it is often said that the first step to solve this equation is to invoke the Born-Oppenheimer approximation. The Born-Oppenheimer approximation is among the most basic approximations in the quantum mechanics of molecules and solids. This approximation relies on the fact that electrons typically move much faster than nuclei, thus the nuclei are considered to be

fixed and their kinetic energy can therefore be neglected. Using this approximation, the last term of Eq. (1.3) can be considered as constant, and the kinetic energy of the nuclei is zero. Therefore, the electronic Schrödinger equation can be written as,

$$\hat{H}_{elec}\Psi_{elec}(r) = E_{elec}\Psi_{elec}(r) \tag{1.4}$$

Consequently, the total energy of the system is

$$E_{total} = E_{elec} + \sum_{A=1}^{M}\sum_{B>A}^{M}\frac{Z_A Z_B}{R_{AB}} \tag{1.5}$$

The potential energy surface (PES) is the total molecular energy with respect to the geometric coordinates of the nuclei.[20] Exploring the PESs is significant for studying reaction energetics and dynamics. The electronic and nulclear Hamiltonian can be defined separately as,

$$\hat{H}_{elec} = -\frac{1}{2}\sum_{i=1}^{N}\nabla_i^2 - \sum_{i=1}^{N}\sum_{A=1}^{M}\frac{Z_A}{r_{iA}} + \sum_{i=1}^{N}\sum_{j>i}^{N}\frac{1}{r_{ij}} \tag{1.6}$$

$$\hat{H}_{nucl} = -\frac{1}{2}\sum_{A=1}^{M}\nabla_A^2 + E_{totol}(R) \tag{1.7}$$

By solving the nuclear Schrödinger equation,

$$\hat{H}_{nucl}\Psi_{nucl} = E\Psi_{nucl} \tag{1.8}$$

one can calculate the translational, rotational, and vibrational energies of molecular systems. More information about the QM methods are provided in the references.[21]

In the QM approach, the territory of methodologies extends from wavefunction theory to density functional theory (DFT), in addition to semi-empirical quantum mechanical approaches. Fifteen to twenty years ago, the study of some mechanistic problems for a chemical model system containing 50 atoms with the QM approach was very expensive. The rise of computer technology made QM calculations faster and cheaper over time, where a model system consisting of 200-300 atoms can be calculated.[22] Today, the study of active sites of enzymes by using the small model

approach, the so-called all-QM or quantum chemical cluster approach, is a very efficient and useful technique for the elucidation of reaction mechanisms of enzymes and their other properties.[22, 23] The main goal of this methodology is to concentrate on the key part of the enzyme around the active site (based on its rule of involvement in the reaction) and treat it with relatively accurate QM methods. In Chapter 2, understanding the catalytic mechanism of the aminoglycoside phosphotranferase using the ONIOM(QM:QM) method (so-called Our own N-layered Integrated molecular Orbital and molecular Mechanics, ONIOM) will be presented.

1.3.3 Molecular Dynamics Simulations

Molecular dynamics (MD) is the most widely used method for simulating biomolecular systems. MD simulations study the dynamic behavior of molecular systems as a function of time. The movement of atoms with respect to time is computed by the integration of Newton's laws of motion,

$$F_i(t) = m_i \frac{d^2 r_i(t)}{dt^2} = -\frac{d}{dr_i(t)} V(r(t)) \tag{1.9}$$

where the potential energy, $V(r(t))$, depends on the atomic coordinates of the system. Figure 1.4 shows the schematic description of the MD cycle.

Practically, MD simulations are carried out in time that is partitioned into time steps (δt). Therefore, Eq. (1.9) can be solved by a discrete-time numerical approximation. Verlet integration is used to calculate the position and the velocity at the time step, t+δt (one time step in the future from time t), by second-order Taylor series approximation,[24, 25]

$$r_i(t + \delta t) = 2r_i(t) - r_i(t - \delta t) + \frac{d^2 r_i(t)}{dt^2} \delta t^2 \tag{1.10}$$

$$v_i(t - \delta t) = v_i(t) + \frac{\delta t}{2} \left[\frac{d^2 r_i(t)}{dt^2} + \frac{d^2 r_i(t + \delta t)}{dt^2} \right] \tag{1.11}$$

where $r_i(t)$ and $v_i(t)$ are the position and the velocity, respectively, of atom i at time t. $r_i(t + \delta t)$ and $v_i(t + \delta t)$ are the position and the velocity, respectively, of atom i at time $t + \delta t$.

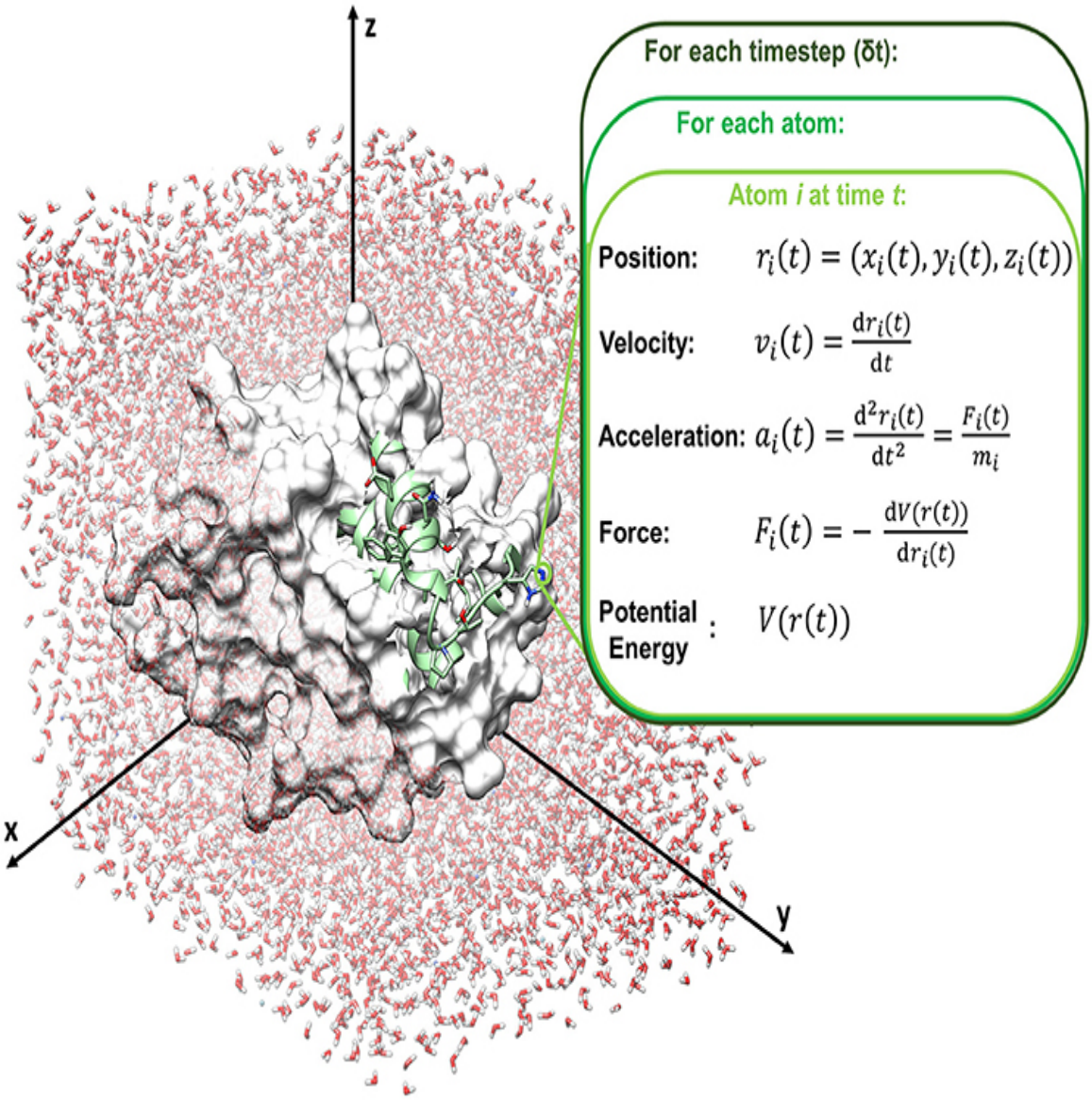

Figure 1.4: Schematic representation of the MD cycle. Reproduced with permission from (*Front. Pharmacol.* 2018, 9:923). Copyright© 2018 Salmaso and Moro.

The following equation describes the contributions of bonded and non-bonded molecular mechanical interactions to the potential energy of the system as defined by the CHARMM force field [26]:

$$V = \sum_{bonds} k_b(b-b_0)^2 + \sum_{angles} k_\theta(\theta-\theta_0)^2 + \sum_{dihedrals} k_\phi[1+cos(n\phi-\delta)] + \sum_{impropers} k_\omega(\omega-\omega_0)^2 + \sum_{Urey-Bradley} k_u(u-u_0)^2 + \sum_{non-bonded} \epsilon \left[\left(\frac{R_{min,ij}}{r_{ij}} \right)^{12} - \left(\frac{R_{min,ij}}{r_{ij}} \right)^{6} \right] + \frac{q_i q_j}{\epsilon r_{ij}} \tag{1.12}$$

where the first five summations represent the bonded interactions and the last summation represents the non-bonded interactions (i.e., van der Waals and electrostatic interactions). Standard all-atom force fields such as CHARMM, AMBER, and GROMOS are commonly used for proteins, in addition to lipids, carbohydrates, nucleic acids, and small molecules.[27]

There are many commercial and non-commercial packages available to conduct MD simulations. In my work, All MD simulations were carried out using the nanoscale molecular dynamics (NAMD) software.[28, 29]

References

(1) Magnet, S.; Blanchard, J. S. *Chemical reviews* **2005**, *105*, 477–498.

(2) Pokrovskaya, V.; Nudelman, I.; Kandasamy, J.; Baasov, T. *Methods in enzymology* **2010**, *478*, 437–462.

(3) Vakulenko, S. B.; Mobashery, S. *Clinical microbiology reviews* **2003**, *16*, 430–450.

(4) Ramirez, M. S.; Tolmasky, M. E. *Drug resistance updates* **2010**, *13*, 151–171.

(5) Vetting, M. W.; Park, C. H.; Hegde, S. S.; Jacoby, G. A.; Hooper, D. C.; Blanchard, J. S. *Biochemistry* **2008**, *47*, 9825–9835.

(6) Vong, K.; Auclair, K. *MedChemComm* **2012**, *3*, 397–407.

(7) Cox, G.; Stogios, P. J.; Savchenko, A.; Wright, G. D. *MBio* **2015**, *6*.

(8) Liu, C.; Zhou, Q.; Li, Y.; Garner, L. V.; Watkins, S. P.; Carter, L. J.; Smoot, J.; Gregg, A. C.; Daniels, A. D.; Jervey, S., et al. Research and development on therapeutic agents and vaccines for COVID-19 and related human coronavirus diseases, 2020.

(9) Lim, Y. X.; Ng, Y. L.; Tam, J. P.; Liu, D. X. *Diseases* **2016**, *4*, 26.

(10) Zhu, N.; Zhang, D.; Wang, W.; Li, X.; Yang, B.; Song, J.; Zhao, X.; Huang, B.; Shi, W.; Lu, R., et al. *New England journal of medicine* **2020**, *382*, 727–733.

(11) Cui, J.; Li, F.; Shi, Z.-L. *Nature Reviews Microbiology* **2019**, *17*, 181–192.

(12) Xu, J.; Zhao, S.; Teng, T.; Abdalla, A. E.; Zhu, W.; Xie, L.; Wang, Y.; Guo, X. *Viruses* **2020**, *12*, 244.

(13) Naqvi, A. A. T.; Fatima, K.; Mohammad, T.; Fatima, U.; Singh, I. K.; Singh, A.; Atif, S. M.; Hariprasad, G.; Hasan, G. M.; Hassan, M. I. *Biochimica et Biophysica Acta (BBA)-Molecular Basis of Disease* **2020**, 165878.

(14) Tang, B.; Bragazzi, N. L.; Li, Q.; Tang, S.; Xiao, Y.; Wu, J. *Infectious disease modelling* **2020**, *5*, 248–255.

(15) Michel, C. J.; Mayer, C.; Poch, O.; Thompson, J. D. *Virology journal* **2020**, *17*, 1–13.

(16) Meng, X.-Y.; Zhang, H.-X.; Mezei, M.; Cui, M. *Current computer-aided drug design* **2011**, *7*, 146–157.

(17) Salmaso, V.; Moro, S. *Frontiers in pharmacology* **2018**, *9*, 923.

(18) Morris, G. M.; Goodsell, D. S.; Halliday, R. S.; Huey, R.; Hart, W. E.; Belew, R. K.; Olson, A. J. *Journal of computational chemistry* **1998**, *19*, 1639–1662.

(19) Schrödinger, E. *Annalen der physik* **1926**, *385*, 437–490.

(20) Schlegel, H. B. *Journal of computational chemistry* **2003**, *24*, 1514–1527.

(21) Alrawashdeh, A. I. Generalized atoms in molecules approach (GAIM approach), Ph.D. Thesis, Memorial University of Newfoundland, 2015.

(22) Himo, F. *Journal of the American Chemical Society* **2017**, *139*, 6780–6786.

(23) Blomberg, M. R.; Borowski, T.; Himo, F.; Liao, R.-Z.; Siegbahn, P. E. *Chemical reviews* **2014**, *114*, 3601–3658.

(24) Verlet, L. *Physical review* **1967**, *159*, 98.

(25) Swope, W. C.; Andersen, H. C.; Berens, P. H.; Wilson, K. R. *The Journal of chemical physics* **1982**, *76*, 637–649.

(26) MacKerell Jr, A. D.; Bashford, D.; Bellott, M.; Dunbrack Jr, R. L.; Evanseck, J. D.; Field, M. J.; Fischer, S.; Gao, J.; Guo, H.; Ha, S., et al. *The journal of physical chemistry B* **1998**, *102*, 3586–3616.

(27) Guvench, O.; MacKerell, A. D. *Molecular modeling of proteins* **2008**, 63–88.

(28) Phillips, J. C.; Braun, R.; Wang, W.; Gumbart, J.; Tajkhorshid, E.; Villa, E.; Chipot, C.; Skeel, R. D.; Kale, L.; Schulten, K. *Journal of computational chemistry* **2005**, *26*, 1781–1802.

(29) Phillips, J. C.; Hardy, D. J.; Maia, J. D.; Stone, J. E.; Ribeiro, J. V.; Bernardi, R. C.; Buch, R.; Fiorin, G.; Hénin, J.; Jiang, W., et al. *The Journal of chemical physics* **2020**, *153*, 044130.

"It seems now clear that a belief in the functional importance of all enzymes found in bacteria is possible only to those richly endowed with Faith."

—Marjory Stephenson

2

Phosphorylation of the Antibiotic Kanamycin

This chapter is adapted with permission from: Abu-Saleh, A.A.A.; Sharma, S.; Yadav, A.; Poirier, R.A. Role of Asp190 in the Phosphorylation of the Antibiotic Kanamycin Catalyzed by the Aminoglycoside Phosphotransferase Enzyme: A Combined QM:QM and MD Study. *J. Phys. Chem. B*, **2020**, *124*, 3494–3504.

2.1 Abstract

The aminoglycoside phosphotransferase (APH(3′)-IIIa) kinases form a clinically central group of antibiotic-resistant enzymes. Computationally, we have studied the catalytic mechanism of the APH(3′)-IIIa enzyme at the atomic-level. The proposed

reaction mechanism involves protonation of Asp190 by the kanamycin 3′-hydroxyl group mediated through an explicit neighboring water molecule, which leads to a simultaneous nucleophilic attack on the γ- phosphate of the ATP by the deprotonated kanamycin 3′-hydroxyl group. The second step is a proton abstraction from the protonated Asp190 to the phosphate group of the phosphorylated kanamycin mediated by an explicit water molecule. The calculated Gibbs energy of activation ($\Delta G^{\ddagger}$) of the rate-determining step for the phosphorylation reaction is 77 kJ mol^{-1} at the M06-2X/6-311++G(2df,p)//ONIOM(M06-2X/6-31+G(d):HF/6-31G(d)) level of theory. This study has provided a new understanding of the APH(3′)-IIIa catalytic mechanism that agrees with the available experimental data ($\Delta G^{\ddagger} = 75 \pm 4$ kJ mol^{-1}) and could provide a starting point for the rational design of mechanism-based inhibitors of aminoglycoside modifying enzymes to circumvent antibiotic resistance.

2.2 Introduction

The curing of infections has become a global concern due to the emergence of antibiotic-resistant bacteria. Earlier this decade, the Director-General of the World Health Organization (WHO) clearly gave a serious warning about antimicrobial resistance with the report entitled "Antimicrobial resistance: no action today, no cure tomorrow".[1] This report triggered an alarm bell regarding the possible appearance of the "postantibiotic era", a stage when antibiotics no longer have any effect on bacterial diseases.[2, 3] Aminoglycoside antibiotics (AGAs) were among the first agents of bacterial warfare found and used clinically and, still, have a crucial role in the treatment of acute bacterial infections caused by both Gram-positive and Gram-negative bacteria.[4, 5] The essentials of AGAs in the treatment of viral infections[6] and human genetic diseases induced by premature termination codons (PTCs)[7] have been illustrated. More recently, they have been developed and used as antifungal agents.[8] Despite the complicated nature of AGAs, it is a well-known fact that AGAs exert their therapeutic effect by binding to the A-site in the decoding region of the 16 ribosomal RNAs (rRNAs); in turn they interfere with translational fidelity through protein synthesis resulting in bacterial cell death.[9–12]

AGAs involve a large number of compounds; however, the bulky number of resistance mechanisms grown by microorganisms have increased in correlation with the number

of AGAs available and the recurring need of their use.[13] A number of structural, biochemical, and genetic studies have been performed to understand the mechanisms of bacterial resistance and have been the focus of many reviews.[3, 13, 14] Among these resistance mechanisms, inhibition of the AGAs' activity by aminoglycoside modifying enzymes (AGMEs) is by far the most clinically important.[15] AGMEs exert enzymatic modification on the hydroxyl or amino groups of the AGAs. Modified AGAs bind weakly to the ribosome, allowing bacteria to recover in the presence of the drug.[16] There are three types of AGMEs found in bacterial pathogens: (i) aminoglycoside phosphotransferases (APHs); (ii) aminoglycoside acetyltransferases (AACs); and (iii) aminoglycoside nucleotidyltransferases (ANTs). The reactions catalyzed by these enzymes (AGMEs) are regioselective, and the sites of modification are represented in parentheses; Figure 2.1 shows kanamycin A antibiotic and sites of modification by AGMEs.

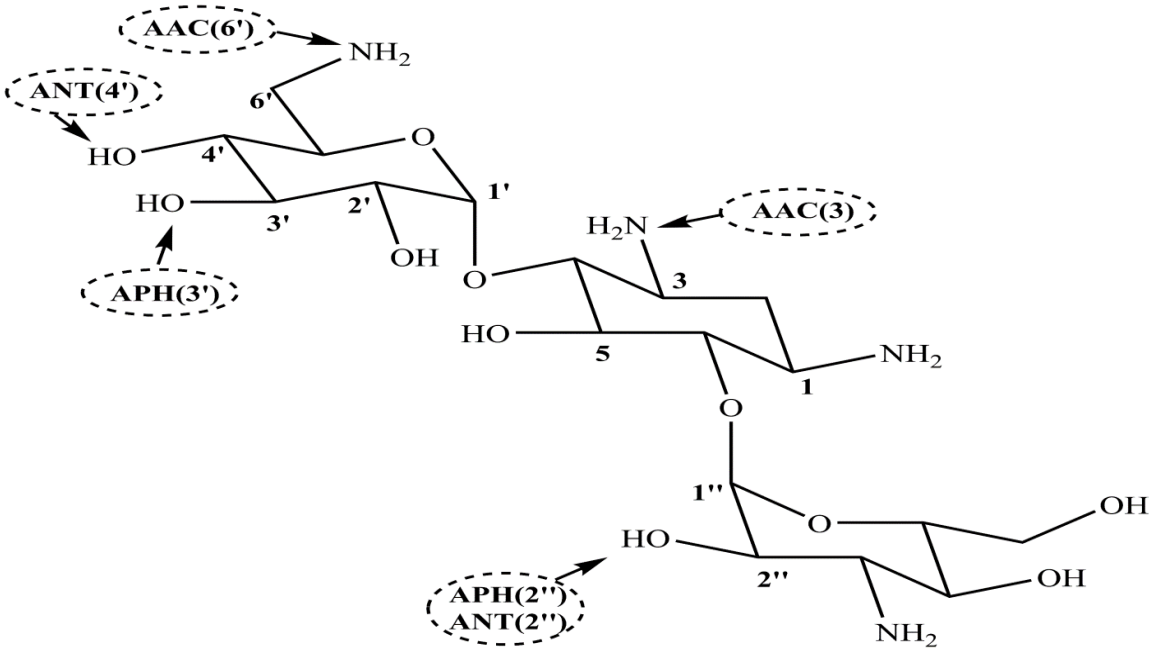

Figure 2.1: Sites of enzymatic modifications by AGMEs on kanamycin A.

The APHs comprise a large family of enzymes which exhibit resistance to a broad spectrum of aminoglycosides. These enzymes catalyze the transfer of γ-phosphate from adenosine triphosphate (ATP) to a hydroxyl group of the antibiotic. There have been several advancements as a result of research related to the structure-function of AGAs to circumvent resistance by bacteria.[15, 17–20] Furthermore, several routes

for the biosynthetic pathway of AGAs have been explored to facilitate the production of new antibiotics.[21–24] However, the struggle to obtain effective antibiotic drugs persists to this day.

Kim and Mobashery explained that the phosphorylation reaction mechanism by APHs may proceed through an associative (S_N2-type) mechanism or dissociative (S_N1-type) mechanism, which forms a metaphosphate-like species as an intermediate.[25] To date, no studies of the phosphorylation mechanism at the molecular level related to the phosphorylation reaction of the AGAs have been published. Mechanism-based developments may help circumvent the bacterial resistance problem. From this viewpoint, the current study explores the phosphorylation mechanism of the kanamycin A antibiotic. The specific kinase on which this study is performed is APH(3′)-IIIa, which phosphorylates 3′-hydroxyl in the streptamine ring of group III antibiotics (see Figure 2.2). This enzyme is found in enterococci and staphylococci and

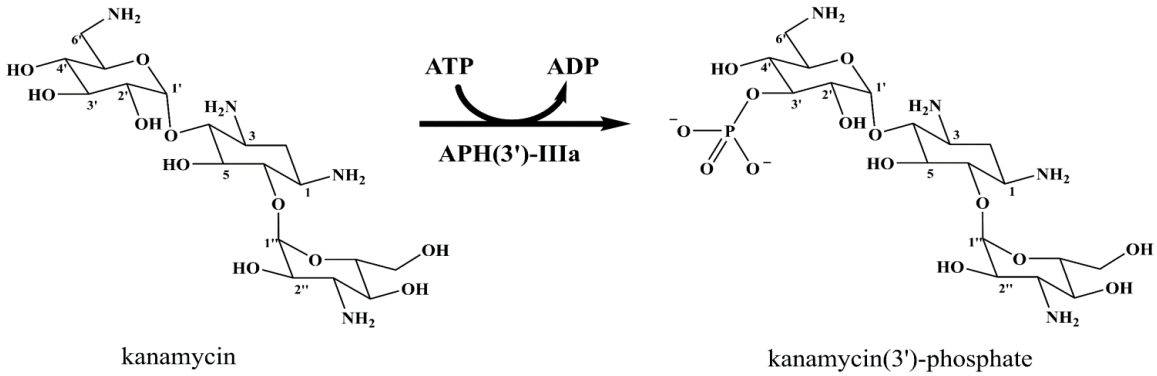

Figure 2.2: Schematic representation for the phosphorylation reaction of the kanamycin A antibiotic by the APH(3′)-IIIa enzyme.

confers resistance to a wide spectrum of antibiotics along with kanamycin, amikacin, lividomycin, neomycin, and paromomycin.[26] The proposed phosphorylation mechanism takes into consideration all five conserved active site residues in the APH(3′)-IIIa enzyme (Lys44, Glu60, Asp190, Asn195, and Asp208).

Our work includes quantum mechanical (i.e., ONIOM (QM:QM)) treatment of the active site based on molecular dynamic (MD) simulations. Many related catalytic mechanisms have shown that the ONIOM method is a powerful tool for studying chemical reactions.[27, 28] By investigating the catalytic mechanism of the aminoglycoside phosphotransferase APH(3′)-IIIa, a deeper view of their atomistic details could

be of great importance in unraveling the puzzles behind their catalytic function and helping design compounds to circumvent resistance issues.

2.3 Theory and Methods

2.3.1 Molecular Dynamics Simulations (Model A)

All the simulations were performed using the NAMD 2.13 package[29, 30] and the CHARMM36 force field.[31] To build Model A, we used atomic coordinates of APH(3′)-IIIa from the crystal structure complexed with kanamycin A, adenosine diphosphate (ADP), and two magnesium ions (Mg^{2+}) determined at 2.4 Å resolution [Protein Data Bank (PDB) entry 1L8T].[32] The determined structure correspondingly shows crystallographic water molecules that were reserved for the startup structure. The structure of ATP was constructed using the molecular structure editor (maestro)[33] from the coordinates of ADP. The protein residues are assigned with their default protonation state at pH 7 as defined in the CHARMM force field. The protein was also protonated using the H++ Web server[34, 35] to confirm that the titratable residues of the active site have the appropriate protonation states. For Model A, explicit solvation was included using the TIP3P water model employing periodic boundary conditions with dimensions of 101.5 $Å^3$. After solvation, the system was neutralized using 22 sodium (Na^+) ions. The MD protocols included minimization, annealing, equilibration, and production. The isothermal-isobaric (NPT) ensemble was used for all MD runs. The time step of integration was chosen to be 2 fs for all simulations. For the MD production of 100 ns simulation, the temperature was preserved at 298.15 K using the Langevin thermostat [36] with a damping frequency of 1 ps^{-1}. The pressure was preserved at 1 atm using the Nosé–Hoover Langevin piston barostat [37, 38] with a period of 0.4 ps and the Langevin piston decay of 0.2 ps. A distance cutoff of 12.0 Å was applied to short-range nonbonded interactions, and 10.0 Å for the smooth switching functions. Long-range electrostatic interactions were treated using the particle-mesh Ewald (PME) method,[39, 40] in which a grid spacing of 1 Å was used for all simulation cells. It should be mentioned here that the atoms of the protein backbone were restrained in the minimization, annealing, and equilibration simulations. However, no atoms were constrained in the 100 ns MD production simulation. The APH(3′)-IIIa protein in complex with the ATP, two Mg^{2+} ions, and kanamycin

A for Model A are depicted in Figure 2.3.

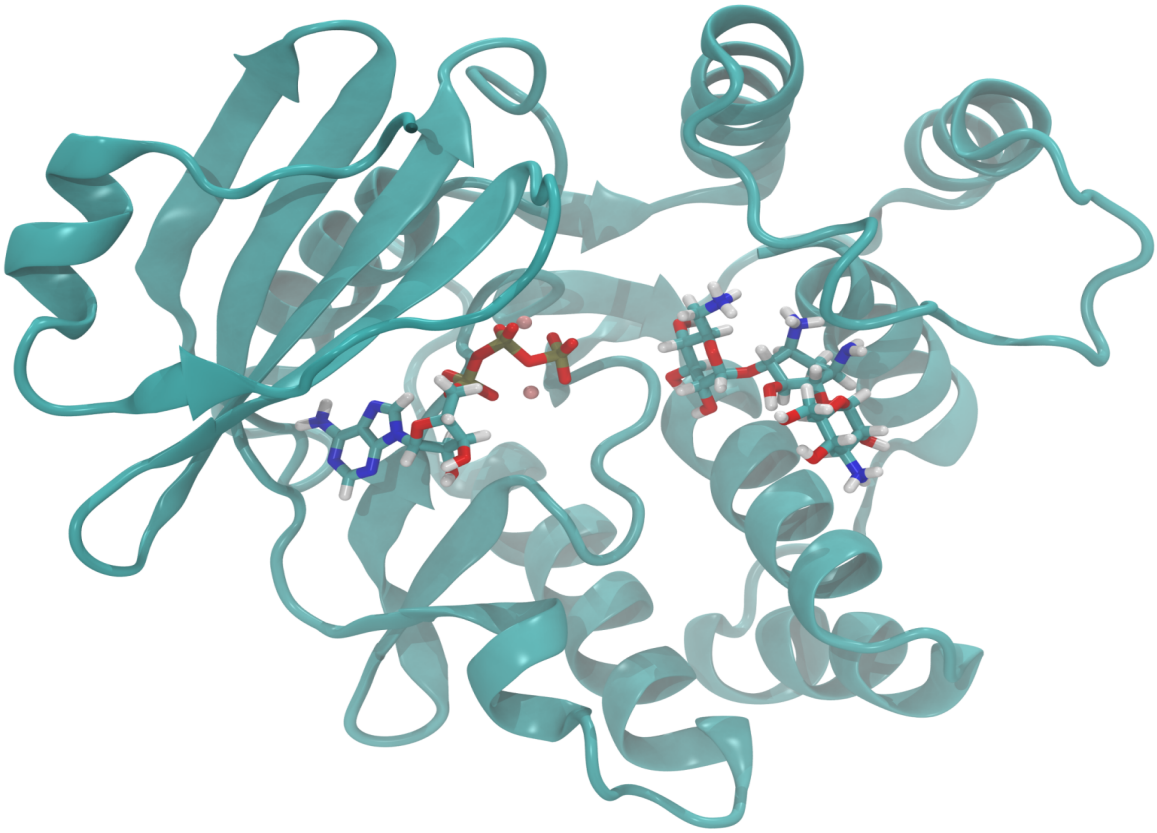

Figure 2.3: Cartoon representation of the APH(3′)-IIIa protein in complex with the ATP, two Mg^{2+} ions, and kanamycin A substrates (represented in licorice).

2.3.2 Quantum Mechanics Calculations (Model B)

The active site of the APH(3′)-IIIa enzyme used for the ONIOM(QM:QM) calculations (Model B) was constructed based on the final frame of the 100 ns MD production of Model A. Model B, consisting of 272 atoms, included kanamycin, ATP, and two Mg^{2+} ions, in addition to the protein's residues Gly25, Met26, Ser27, Lys44, Glu60, Asp190, Asn195, and Asp208. Moreover, Model B was solvated by incorporation of explicit solvation (total of 9 water molecules) and implicit solvation (PCM)[41] by using integral equation formalism of the polarizable continuum model (IEFPCM). We have used the ONIOM method [42, 43] as implemented in the Gaussian 16 quantum

package[44] to carry out QM calculations. Model B was partitioned into two subsystems (i.e., layers) based on their level of involvement in the reaction. The high-level layer (105 atoms) includes five water molecules, the residues (Asp190, Asn195, and Asp208) and the atoms from the substrates that are highly involved in the reaction. The low-level layer (167 atoms) contains the remaining atoms of Model B. In order to keep the effect of the chemical bonds at the QM-QM boundary, the broken bonds have been capped with hydrogen atoms as link atoms. For Model B the structures were optimized by utilizing the ONIOM(M06-2X/6-31+G(d):HF/6-31G(d)) method, in which the high-level layer is computed with the M06-2X/6-31+G(d) level of theory, and the low-level layer is computed with the HF/6-31G(d) level of theory. The M06-2X method has been shown to perform very well for noncovalent interactions, barrier heights, and thermochemistry for main-group elements.[45] It should be noted that the optimization is carried out using the PCM solvation model. The optimized structures on the potential energy surfaces (PESs) were validated by the analysis of the corresponding Hessian matrices (the second-order partial derivatives of the energy-function of a molecule with respect to its geometric coordinates). The minima associated with the transition states were analyzed using the intrinsic reaction coordinate (IRC)[46, 47] calculations. The total energy of the ONIOM(QM1:QM2) of Model B (E_{tot}) is calculated using the subtractive scheme, in which the high-level QM energy of the subsystem ($E_{QM1,subsystem}$) is added to the low-level QM energy of the model system ($E_{QM2,system}$), and eventually the low-level QM energy of the subsystem ($E_{QM2,subsystem}$) is subtracted from the addition:

$$E_{tot} = E_{QM1,subsystem} + E_{QM2,system} - E_{QM2,subsystem} \tag{2.1}$$

For all optimized structures, single-point energy calculations have been performed using the M06-2X/6-311++G(2df,p) level of theory with the PCM solvation model. The ONIOM(M06-2X/6-31+G(d):HF/6-31G(d)) thermochemistry results were used to compute the correction of vibrational energies required for the estimation of zero-point energy (ZPE) and the Gibbs energy change from 0 K to the 298.15 K (Δ_0^TG). These corrections are added to the M06-2X/6-311+G(2df,p) electronic energy. Unless otherwise stated all chemical structures of Model B shown in the figures are optimized at the ONIOM(M06-2X/6-31+G(d):HF/6-31G(d)) method along with the PCM solvation model.

2.4 Results and Discussion

In the direction of investigating the catalytic mechanism of the APH(3′)-IIIa, we based our study on the X-ray crystal structure, MD simulations (Model A), and ONIOM(QM:QM) calculations (Model B). The X-ray structure of this enzyme (PDB code: 1L8T) has the kanamycin–ADP complex bound to the active site. First, the phosphate group (β-phosphate) of the ADP has three terminal oxygens with 2174, 2175, and 2176 labeling in the 1L8T PDB file. These labeled oxygens have been linked with a PO_3 group (γ-phosphate) to obtain the substrate kanamycin–ATP complex (the reactant of the reaction). After the addition of the phosphate group to the ADP, we ended up with three different conformations of the ATP. Therefore, three MD simulations of 100 ns have been conducted to appraise if this commutation of substrates could show any critical conformational rearrangements in the active site. As a result, only one simulation, with a PO_3 group linked to the 2176 oxygen, confirmed that the active site is robust, and most of the interactions among the active site residues were conserved. The assessment of the structural stability for MD simulations was achieved by the root-mean-square fluctuation (RMSF) that represents the average over time of the root-mean-square deviation (RMSD) over protein backbone atoms (see Figure A.1 in Appendix A). The average value of the RMSD over the 100 ns MD simulation has the value of 1.63 Å. It should be mentioned that the RMSF of the conserved residues of the active site did not exceed the value of 1.48 Å. The thermodynamic temperature and pressure that control the most probable population of states of our system at thermal equilibrium over time have been analyzed to ensure that the system is close to 298.15 K and 1 atm, respectively (see Figures A.2 and A.3 in Appendix A).

The MD simulation and the ONIOM(QM:QM) calculations revealed that the substrates are surrounded by a network of hydrogen bonds and electrostatic interactions contributed by assorted residues of the active site, similarly to what is observed in the X-ray structure 1L8T (Table 2.1 and Figure 2.4).

Met26, Ser27, and Lys44 interact directly with the phosphate groups of the ATP, whereas Glu60 forms a salt bridge with the amino group of Lys44 side chain, making Lys44 more available for nucleotide coordination in the active site. The role of Met and Ser amide hydrogens in nucleotide capture has been reported through a site-directed mutagenesis study of the Met26 and Ser27 to Ala/Pro mutations.[48] It has

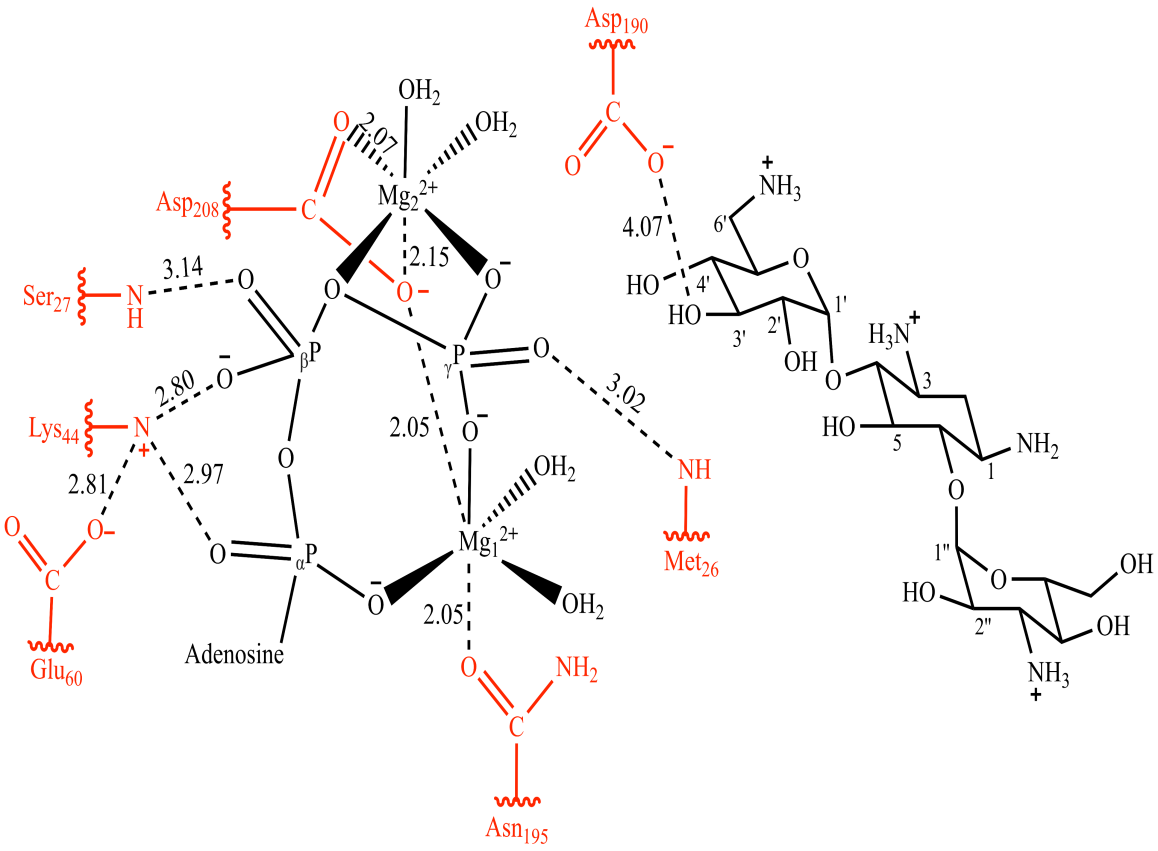

Figure 2.4: APH(3′)-IIIa active site environment showing a network of hydrogen bonds and electrostatic interactions. Distances (in Å) of the reactant complex optimized at the (M06-2X/6-31+G(d):HF/6-31G(d)) method.

Table 2.1: Distances (Å) for some residues of the active site of 1L8T, the substrates, and the Mg^{2+} ions[a]

	X-ray Structure (1L8T)	Model A[b]	Model B[c]
Met26(N)–γ-phosphate(O)	–	3.66 (2.78)	3.02
Ser27(N)–β-phosphate(O)	3.24	5.13 (3.21)	3.14
Lys44(N^+)–α-phosphate(O)	2.77	2.67 (2.85)	2.97
Lys44(N^+)–β-phosphate(O)	3.06	3.01 (3.14)	2.80
Lys44(N^+)–Glu60(O^-)	2.81	2.85 (2.79)	2.81
Asp190(O^-)–Kanamycin(3′-O)	2.71	4.87 (5.44)	4.07
Asn195(O)–Mg1	1.86	2.09 (2.08)	2.05
Asp208(O^-)–Mg1	1.98	1.90 (1.95)	2.05
Asp208(O^-)–Mg2	2.58	2.34 (2.26)	2.15
Asp208(O)–Mg2	2.16	1.83 (1.80)	2.07

[a]The bonds are illustrated in Figure 4; [b]averaged bond length during the 100 ns NPT ensemble (values between parentheses represent bond lengths of the final frame); [c]the structure is optimized using the ONIOM(M06-2X/6-31+G(d):HF/6-31G(d)) method with the PCM solvation model.

been suggested in the literature that Asp190 is an active site base.[13] Asn195 and Asp208 act as ligands involved in coordinating the two Mg^{2+} ions. Asp208 coordinates both Mg^{2+} ions in the active site, and it has been demonstrated that Asp208 has a significant role in transition state stabilization.[49] Four explicit water molecules are implicated in Mg^{2+} coordination.

A previous study elucidated that the pKa values for kanamycin amino groups determined by potentiometric titrations at 25 °C and 0.1 M NaCl are 6.45, 7.74, 8.45, and 9.5.[50] Therefore, at physiological pH, three amino groups should be protonated (see Figure 2.4), and we have taken this into consideration for the QM:QM calculations and MD simulations. The optimized structure of the reactant complex is depicted in Figure 2.5. The (M06-2X/6-311+G(2df,p)//ONIOM(M06-2X/6-31+G(d):HF/6-31G(d)) method was used to calculate the charge distribution of the reactant utilizing natural bond orbital analysis.[51, 52] The resulting charge of the 3′-hydroxyl oxygen of kanamycin (–0.82) and the side-chain oxygen of the Asp190 (–0.85) asserts the nucleophilic behavior of these oxygens. On the other hand, the γ-phosphate phosphorus of the ATP (+2.67) asserts the electrophilic behavior.

In our first attempts to study the catalytic mechanism of the APH(3′)-IIIa, we investigated the dissociative mechanism. In this mechanism, the γ-phosphate of the ATP is released in the first step forming the ADP and the metaphosphate group. In

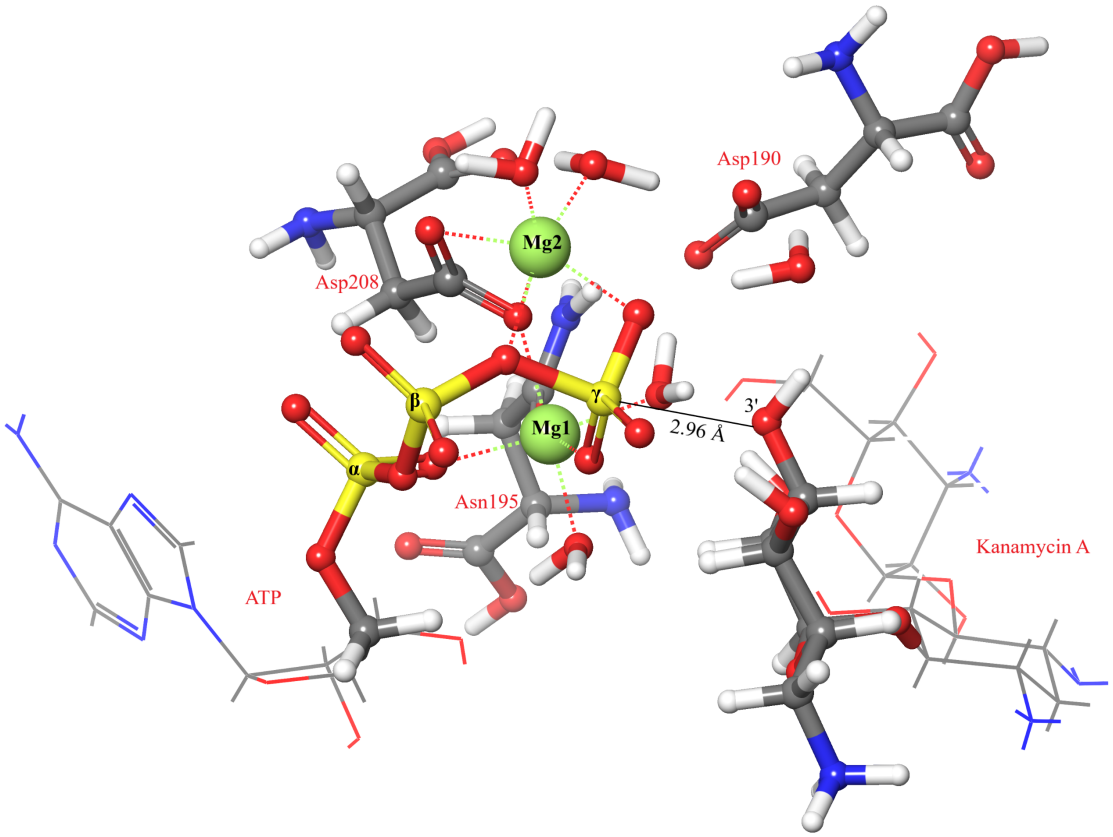

Figure 2.5: ONIOM optimized structure of the reactant complex. The high-layer is illustrated in balls and sticks and the low-layer in lines. For clarity, only some of the low-layer atoms are shown.

the second step, the nucleophilic attack of the 3′-hydroxyl group of kanamycin on the metaphosphate forms the phosphorylated kanamycin with the ADP product complex. All trials of the proposed dissociative mechanism that could lead to the formation of the ADP and the metaphosphate intermediate failed. Many trials for Model B were made, such as transition state scan, optimization where the metaphosphate is constrained, followed by an optimization where none of the atoms were constrained. In addition, the synchronous transit-guided quasi-Newton (STQN) methods (QST2 and QST3) were also tried. All these trials were explored to locate the dissociative mechanism at the ONIOM(M06-2X/6-31+G(d):HF/6-31G(d)) method. For the dissociative mechanism, the metaphosphate, after detachment from ATP, should have a sufficient stabilization, but because the nucleophiles (3′-hydroxyl group of kanamycin, and the β-phosphate oxygen of the ADP) are close enough (see Figure A.4 in Appendix A), the environment is all set for an associative transition state. Hence, the ONIOM transition state geometry search does not converge to a dissociative transition state. Consequently, this forms an associative transition state rather than stabilization of the metaphosphate intermediate. Nevertheless, we proceeded to investigate the associative mechanism.

Herein, the first step of the proposed reaction mechanism (Figure 2.6) is initiated by proton transfer from the 3′-hydroxyl group of kanamycin to the oxygen of Asp190 mediated by one of the explicit water molecules; simultaneously, the 3′-hydroxyl oxygen of the kanamycin attacks the γ-phosphate of the ATP, forming the intermediate complex of phosphorylated kanamycin and ADP. The Gibbs energy of activation ($\Delta G^{\ddagger}$) for this step is 77 kJ mol^{-1}, calculated at the M06-2X/6-311++G(2df,p) level of theory. Both Mg^{2+} ions and Asp208 play a crucial role in stabilization of the bipyramidal-like transition state. The ONIOM optimized structure of the transition state and intermediate are shown in Figures 2.7 and 2.8, respectively.

The second step is a proton transfer mechanism; the explicit water molecule facilitates the proton transfer process from the aspartic acid to the phosphate group of the phosphorylated kanamycin. The $\Delta G^{\ddagger}$ of the second step is 37 kJ mol^{-1}, calculated at the M06-2X/6-311++G(2df,p) level of theory. The energy barrier of the second step is significantly lower than the energy barrier of the first step with the energy difference of 40 kJ mol^{-1}. This concludes that the first step is the rate-determining step of the proposed reaction mechanism. The ONIOM optimized structures of the second transition state and the product complex are shown in Figures 2.9 and 2.10. The

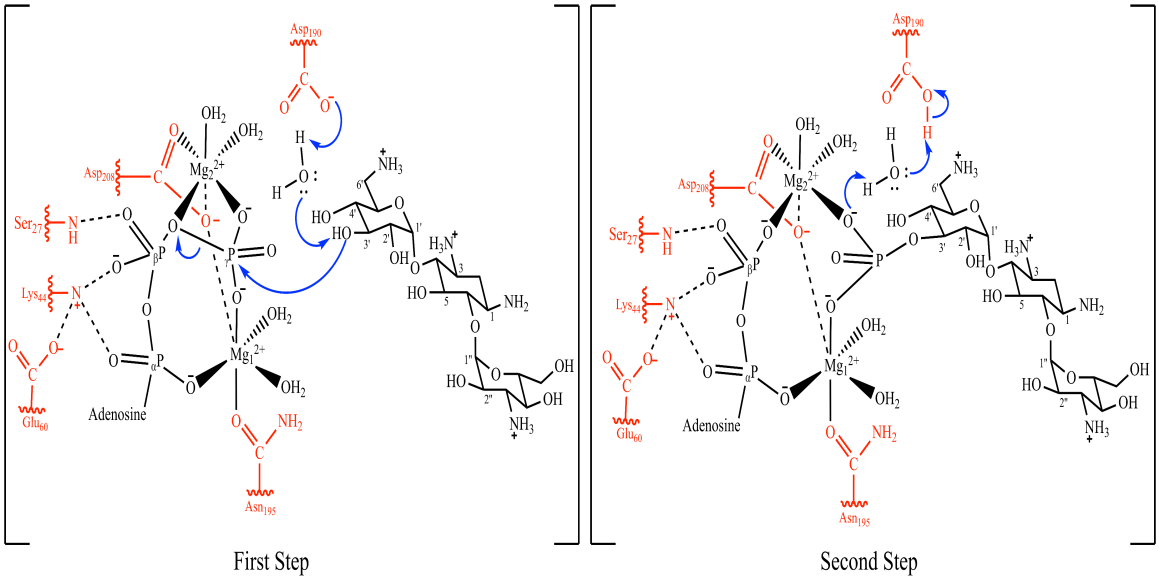

Figure 2.6: Proposed catalytic mechanism of the APH(3′)-IIIa enzyme.

potential energy surface of the proposed reaction mechanism is given in Figure 2.11.

The overall energy barrier of the proposed reaction mechanism has a $\Delta G^{\ddagger}$ of 77 kJ mol^{-1}, calculated at the M06-2X/6-311++G(2df,p) level of theory. These results agree with the experimental $\Delta G^{\ddagger}$ value (75 $\pm$ 4 kJ mol^{-1}) for the phosphorylation of kanamycin A.[53] It should be pointed out that the reported $\Delta G^{\ddagger}$ value has been obtained by[53]

$$\Delta G^{\ddagger} = -RT \ln(k_{cat}h/K_BT) \tag{2.2}$$

where R is the gas constant, T is the temperature in Kelvin, h is Planck's constant, and K_B is the Boltzmann constant. Therefore, the fitted parameter of the turnover rate (k_{cat}) of 0.5 s^{-1} at 298 K is used to give an energy barrier of 75 kJ mol^{-1}.[53] The Gibbs energy of the reaction indicates that the process is slightly exergonic, which proceeds with a net release of energy (ΔG = –4 kJ mol^{-1}). The barriers of activation along with the thermodynamic properties are listed in Table 2.2.

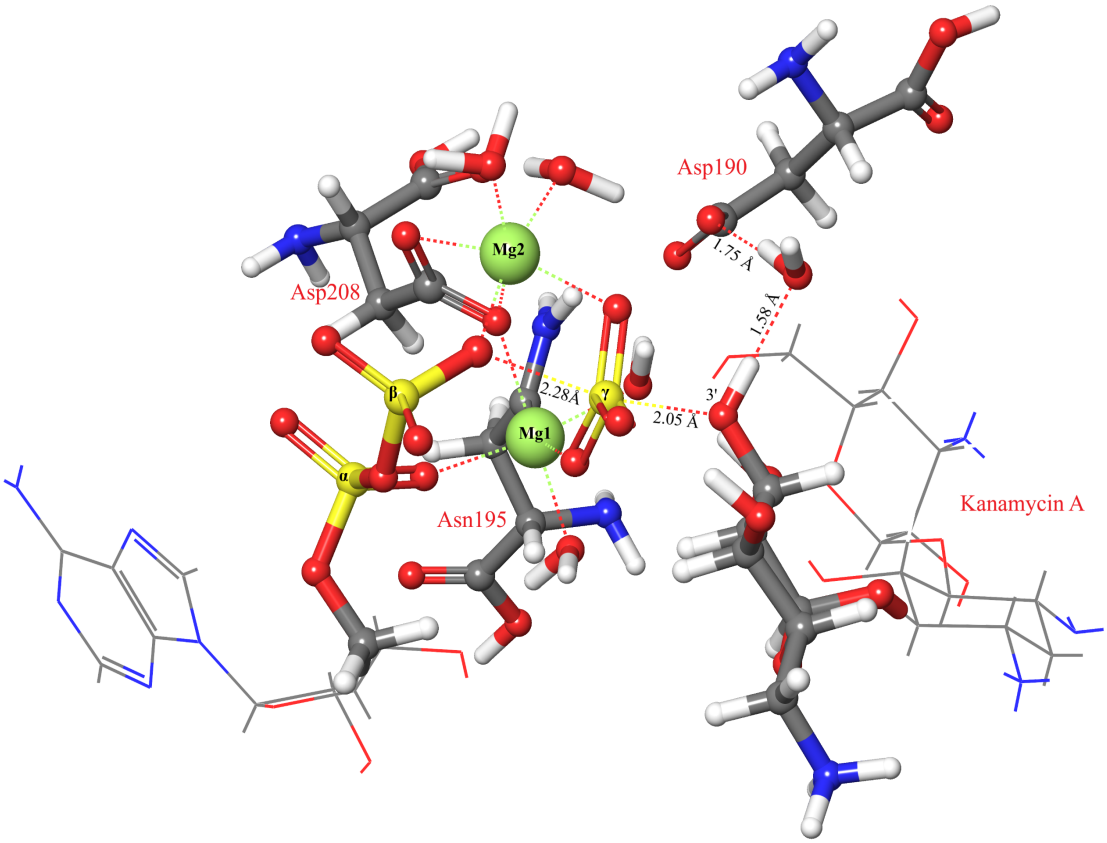

Figure 2.7: ONIOM optimized structure of the transition state (1st step) forming a bipyramidal-like geometry. The high-layer is illustrated in balls and sticks and the low-layer in lines. For clarity, only some of the low-layer atoms are shown.

Table 2.2: Gibbs energy of activation and Gibbs energy of reaction for the phosphorylation reaction of kanamycin by ATP in kJ mol^{-1} at 298.15 K

Gibbs energies	ONIOM(QM:QM)[a]	M06-2X/6-311++G(2df,p)[b]	experiment[c]
$\Delta G^{\ddagger}$ (1st step)	72	77	
$\Delta G^{\ddagger}$ (2nd step)	41	37	
$\Delta G^{\ddagger}$ (overall)	72	77	75 ± 4
ΔG (reaction)	3	–4	

[a]Calculated at ONIOM(M06-2X/6-31+G(d):HF/6-31G(d)) method; [b]all geometries of the stationary points were optimized at the ONIOM(M06-2X/6-31+G(d):HF/6-31G(d)) method; [c]experimental value taken from ref [53].

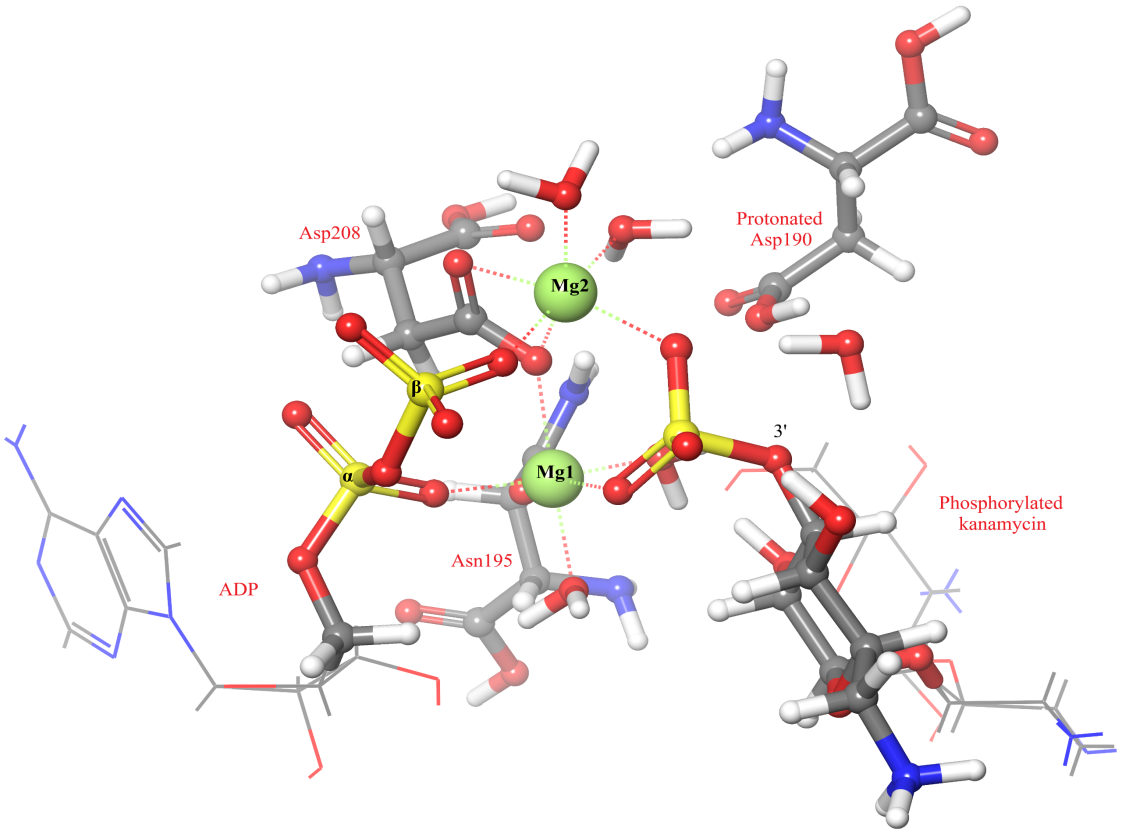

Figure 2.8: ONIOM optimized structure of the intermediate complex. The high-layer is illustrated in balls and sticks and the low-layer in lines. For clarity, only some of the low-layer atoms are shown.

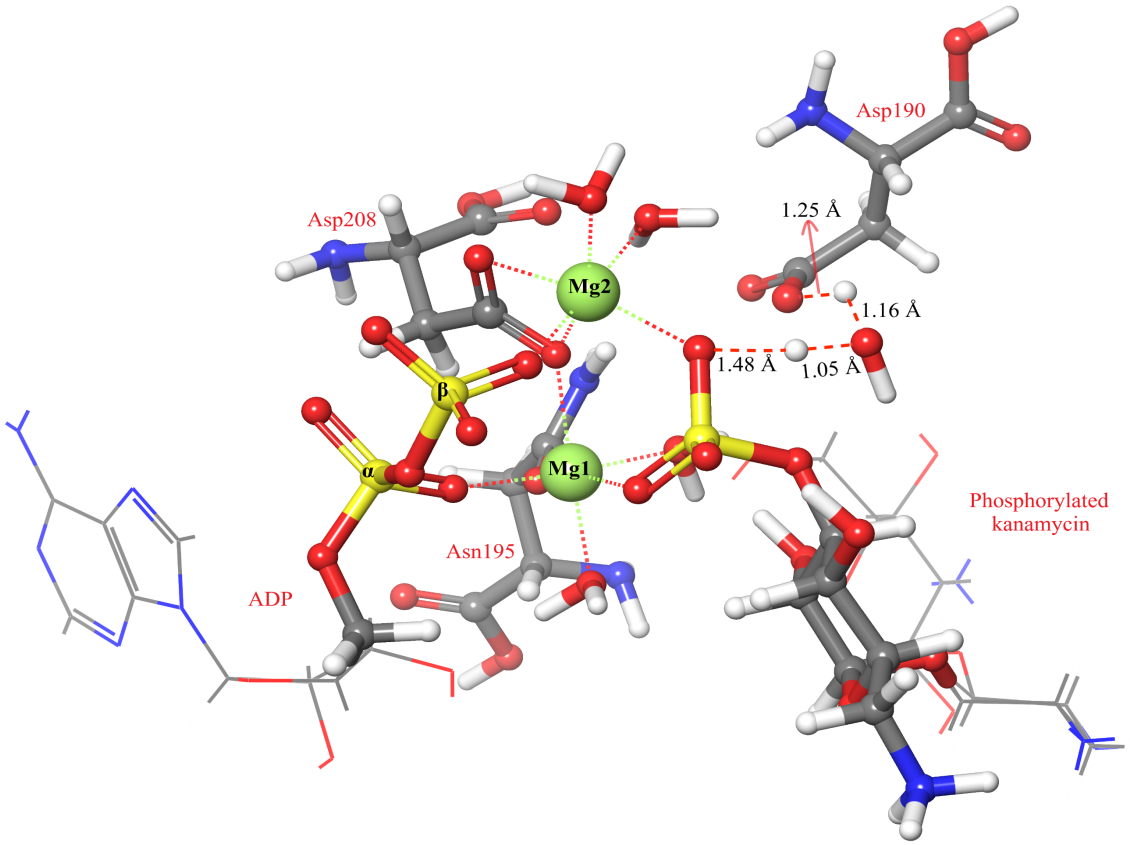

Figure 2.9: ONIOM optimized structure of the transition state (2nd step). The high-layer is illustrated in balls and sticks and the low-layer in lines. For clarity, only some of the low-layer atoms are shown.

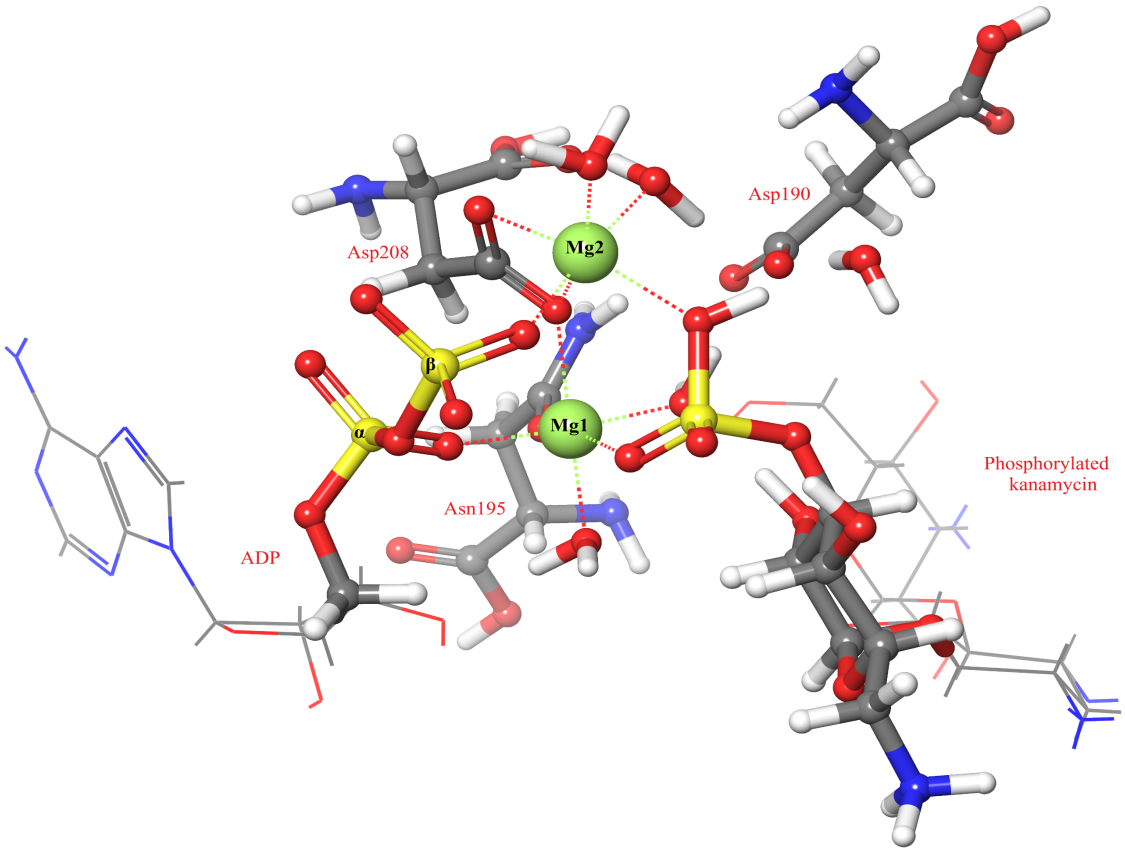

Figure 2.10: ONIOM optimized structure of the product complex. The high-layer is illustrated in balls and sticks and the low-layer in lines. For clarity, only some of the low-layer atoms are shown.

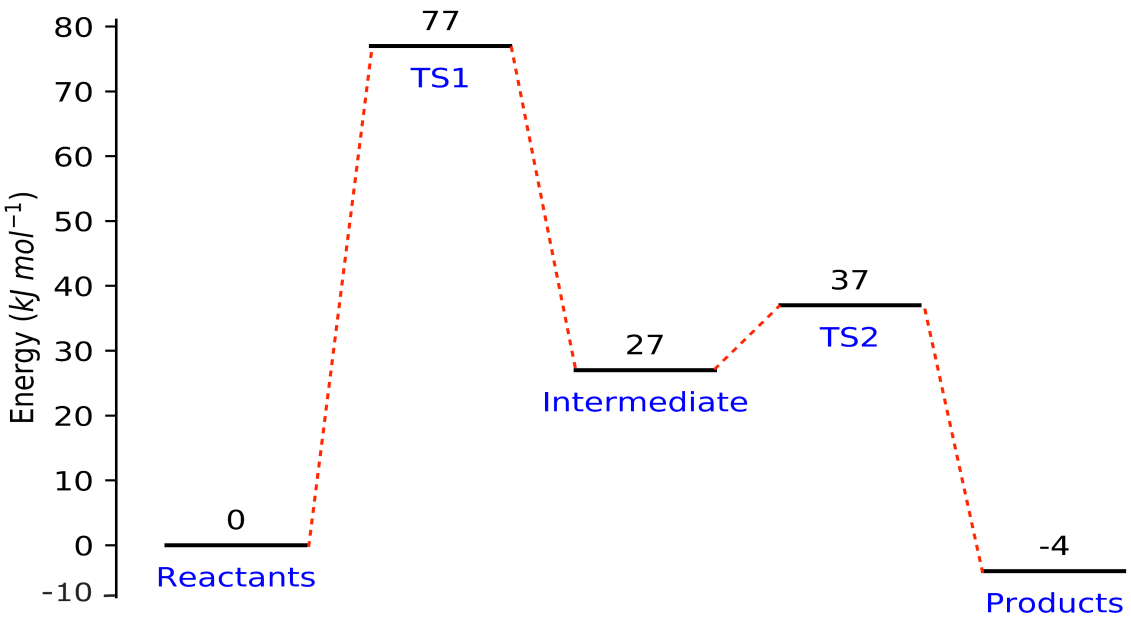

Figure 2.11: Potential energy surface of the proposed reaction mechanism calculated at the M06-2X/6-311++G(2df,p)//ONIOM(M06-2X/6- 31+G(d):HF/6-31G(d)) level of theory with the PCM solvation model.

2.5 Conclusions

The computational study of the APH(3′)-IIIa catalytic mechanism illustrated herein helps to construct the PES of the associated reaction mechanism. The proposed associative mechanism involves initiation by protonation of Asp190 by a neighboring water molecule, which leads to hydrogen abstraction from the kanamycin 3′-hydroxyl group and simultaneously triggers the critical nucleophilic attack on the γ-phosphate of the ATP. The second step is a proton transfer from the aspartic acid to the phosphate group of the phosphorylated kanamycin mediated by the explicit water molecule. Asp208 plays a significant role by binding to both Mg^{2+} ions, and this is likely important for constructing a bipyramidal-like transition state. The results also describe the influence of the conserved active site residues (Met26, Ser27, Lys44, Glu60, Asp190, Asn195, and Asp208). These residues all form the catalytic core of the enzyme and are involved in metal coordination, nucleotide triphosphate binding, or the cooperation of the γ-phosphate transfer. The M06-2X/6-311++G(2df,p)//ONIOM(M06-2X/6-31+G(d):HF/6-31G(d)) overall $\Delta G^{\ddagger}$ for the reaction (77 kJ mol^{-1}) agrees well with the experimental value [53] of 75 $\pm$ 4 kJ mol^{-1}. These results indicate the reliability of

the adopted ONIOM(QM:QM) method. Despite all failed trials to explore the dissociative catalytic pathway, this mechanism, nevertheless, might be explored in future research. Potent inhibitors of APH(3′)-IIIa that block the initiation by Asp190 or break the proton relay process may be designed based on the associative mechanism proposed herein to reverse AGAs resistance, which could lead to significant medical and clinical benefits.

References

(1) Chan, M. *World Health Organization* **2011**.

(2) Kåhrström, C. T. *Nature Reviews Microbiology* **2013**, *11*, 146–146.

(3) Takahashi, Y.; Igarashi, M. *The Journal of antibiotics* **2018**, *71*, 4–14.

(4) Becker, B.; Cooper, M. A. *ACS chemical biology* **2013**, *8*, 105–115.

(5) Houghton, J. L.; Green, K. D.; Chen, W.; Garneau-Tsodikova, S. *ChemBioChem* **2010**, *11*, 880–902.

(6) Prayle, A.; Smyth, A. R. *Current opinion in pulmonary medicine* **2010**, *16*, 604–610.

(7) Kamei, M.; Kasperski, K.; Fuller, M.; Parkinson-Lawrence, E. J.; Karageorgos, L.; Belakhov, V.; Baasov, T.; Hopwood, J. J.; Brooks, D. A. In *JIMD Reports-Case and Research Reports, Volume 13*; Springer: 2013, pp 139–147.

(8) Subedi, Y. P.; AlFindee, M. N.; Takemoto, J. Y.; Chang, C.-W. T. *MedChemComm* **2018**, *9*, 909–919.

(9) Fourmy, D.; Recht, M. I.; Blanchard, S. C.; Puglisi, J. D. *Science* **1996**, *274*, 1367–1371.

(10) Romanowska, J.; Setny, P.; Trylska, J. *The Journal of Physical Chemistry B* **2008**, *112*, 15227–15243.

(11) Długosz, M.; Trylska, J. *The Journal of Physical Chemistry B* **2009**, *113*, 7322–7330.

(12) Bezerra, K. S.; Fulco, U. L.; Esmaile, S. C.; Lima Neto, J. X.; Machado, L. D.; Freire, V. N.; Albuquerque, E. L.; Oliveira, J. I. *The Journal of Physical Chemistry B* **2019**, *123*, 6421–6429.

(13) Magnet, S.; Blanchard, J. S. *Chemical reviews* **2005**, *105*, 477–498.

(14) Alekshun, M. N.; Levy, S. B. *Cell* **2007**, *128*, 1037–1050.

(15) Chandrika, N. T.; Garneau-Tsodikova, S. *Chemical Society Reviews* **2018**, *47*, 1189–1249.

(16) Llano-Sotelo, B.; Azucena Jr, E. F.; Kotra, L. P.; Mobashery, S.; Chow, C. S. *Chemistry & biology* **2002**, *9*, 455–463.

(17) Vong, K.; Tam, I. S.; Yan, X.; Auclair, K. *ACS chemical biology* **2012**, *7*, 470–475.

(18) Willby, M. J.; Green, K. D.; Gajadeera, C. S.; Hou, C.; Tsodikov, O. V.; Posey, J. E.; Garneau-Tsodikova, S. *ACS chemical biology* **2016**, *11*, 1639–1646.

(19) Matsushita, T.; Sati, G. C.; Kondasinghe, N.; Pirrone, M. G.; Kato, T.; Waduge, P.; Kumar, H. S.; Sanchon, A. C.; Dobosz-Bartoszek, M.; Shcherbakov, D., et al. *Journal of the American Chemical Society* **2019**, *141*, 5051–5061.

(20) Sati, G. C.; Sarpe, V. A.; Furukawa, T.; Mondal, S.; Mantovani, M.; Hobbie, S. N.; Vasella, A.; Böttger, E. C.; Crich, D. *ACS infectious diseases* **2019**, *5*, 1718–1730.

(21) Park, J. W.; Park, S. R.; Nepal, K. K.; Han, A. R.; Ban, Y. H.; Yoo, Y. J.; Kim, E. J.; Kim, E. M.; Kim, D.; Sohng, J. K., et al. *Nature chemical biology* **2011**, *7*, 843–852.

(22) Sucipto, H.; Kudo, F.; Eguchi, T. *Angewandte Chemie International Edition* **2012**, *51*, 3428–3431.

(23) Ban, Y. H.; Song, M. C.; Hwang, J.-y.; Shin, H.-l.; Kim, H. J.; Hong, S. K.; Lee, N. J.; Park, J. W.; Cha, S.-S.; Liu, H.-w., et al. *Nature chemical biology* **2019**, *15*, 295–303.

(24) Ban, Y. H.; Song, M. C.; Park, J. W.; Yoon, Y. J. *Natural product reports* **2020**, *37*, 301–311.

(25) Kim, C.; Mobashery, S. *Bioorganic chemistry* **2005**, *33*, 149–158.

(26) McKay, G.; Thompson, P. R.; Wright, G. *Biochemistry* **1994**, *33*, 6936–6944.

(27) Chung, L. W.; Sameera, W.; Ramozzi, R.; Page, A. J.; Hatanaka, M.; Petrova, G. P.; Harris, T. V.; Li, X.; Ke, Z.; Liu, F., et al. *Chemical reviews* **2015**, *115*, 5678–5796.

(28) Gesto, D. S.; Cerqueira, N. M.; Fernandes, P. A.; Ramos, M. J. *Journal of the American Chemical Society* **2013**, *135*, 7146–7158.

(29) Phillips, J. C.; Braun, R.; Wang, W.; Gumbart, J.; Tajkhorshid, E.; Villa, E.; Chipot, C.; Skeel, R. D.; Kale, L.; Schulten, K. *Journal of computational chemistry* **2005**, *26*, 1781–1802.

(30) Ribeiro, J. V.; Bernardi, R. C.; Rudack, T.; Stone, J. E.; Phillips, J. C.; Freddolino, P. L.; Schulten, K. *Scientific reports* **2016**, *6*, 1–14.

(31) Best, R. B.; Zhu, X.; Shim, J.; Lopes, P. E.; Mittal, J.; Feig, M.; MacKerell Jr, A. D. *Journal of chemical theory and computation* **2012**, *8*, 3257–3273.

(32) Fong, D. H.; Berghuis, A. M. *The EMBO journal* **2002**, *21*, 2323–2331.

(33) Maestro, Schrödinger Release 11.8.0; Schrödinger, LLC: New York, NY, 2019.

(34) Gordon, J. C.; Myers, J. B.; Folta, T.; Shoja, V.; Heath, L. S.; Onufriev, A. *Nucleic acids research* **2005**, *33*, W368–W371.

(35) Anandakrishnan, R.; Aguilar, B.; Onufriev, A. V. *Nucleic acids research* **2012**, *40*, W537–W541.

(36) Grest, G. S.; Kremer, K. *Physical Review A* **1986**, *33*, 3628.

(37) Nosé, S.; Klein, M. *Molecular Physics* **1983**, *50*, 1055–1076.

(38) Nosé, S. *Molecular Physics* **2002**, *100*, 191–198.

(39) Darden, T.; York, D.; Pedersen, L. *The Journal of chemical physics* **1993**, *98*, 10089–10092.

(40) Essmann, U.; Perera, L.; Berkowitz, M. L.; Darden, T.; Lee, H.; Pedersen, L. G. *The Journal of Chemical Physics* **1995**, *103*, 8577–8593.

(41) Cancès, E.; Mennucci, B.; Tomasi, J. *The Journal of Chemical Physics* **1997**, *107*, 3032–3041.

(42) Svensson, M.; Humbel, S.; Froese, R. D. J.; Matsubara, T.; Sieber, S.; Morokuma, K. *The Journal of Physical Chemistry* **1996**, *100*, 19357–19363.

(43) Dapprich, S.; Komáromi, I.; Byun, K.; Morokuma, K.; Frisch, M. J. *Journal of Molecular Structure: THEOCHEM* **1999**, *461-462*, 1–21.

(44) Frisch, M. J. et al. Gaussian˜16 Revision C.01, Gaussian Inc. Wallingford CT, 2016.

(45) Mardirossian, N.; Head-Gordon, M. *Journal of Chemical Theory and Computation* **2016**, *12*, 4303–4325.

(46) Fukui, K. *Accounts of Chemical Research* **1981**, *14*, 363–368.

(47) Hratchian, H. P.; Schlegel, H. B. *Journal of Chemical Theory and Computation* **2005**, *1*, 61–69.

(48) Thompson, P. R.; Boehr, D. D.; Berghuis, A. M.; Wright, G. D. *Biochemistry* **2002**, *41*, 7001–7007.

(49) Boehr, D. D.; Thompson, P. R.; Wright, G. D. *Journal of Biological Chemistry* **2001**, *276*, 23929–23936.

(50) Fuentes-Martínez, Y.; Godoy-Alcántar, C.; Medrano, F.; Dikiy, A.; Yatsimirsky, A. K. *Bioorganic Chemistry* **2010**, *38*, 173–180.

(51) Foster, J. P.; Weinhold, F. *Journal of the American Chemical Society* **1980**, *102*, 7211–7218.

(52) Reed, A. E.; Curtiss, L. A.; Weinhold, F. *Chemical Reviews* **1988**, *88*, 899–926.

(53) Soto, B. S. Comparison of Activation Enthalpies for Aminoglycoside Modification Reactions, MA thesis, University of Tennessee, 2015.

"Curiosity—the rover and the concept—is what science is all about: the quest to reveal the unknown."

—Ahmed Zewail

3

Discovery of Potent Inhibitors for SARS-CoV-2's Main Protease

This chapter is adapted with permission from: Abu-Saleh, A.A.A.; Awad, I.E.; Yadav, A.; Poirier, R.A. Discovery of potent inhibitors for SARS-CoV-2's main protease by ligand-based/structure-based virtual screening, MD simulations, and binding energy calculations. *Phys. Chem. Chem. Phys.*, **2020**, *22*, 23099–23106.

3.1 Abstract

COVID-19 has caused lockdowns all over the world in early 2020, as a global pandemic. Both theoretical and experimental efforts are seeking to find an effective treatment to suppress the virus. *In silico* drug design can play a vital role in identifying promising

drug candidates against COVID-19. Herein, we focused on the main protease of SARS-CoV-2 that plays crucial biological functions in the virus. We performed a ligand-based virtual screening followed by a docking screening for testing approved drugs and bioactive compounds listed in the DrugBank and ChEMBL databases. The top 8 docking results were advanced to all-atom MD simulations to study the relative stability of the protein–ligand interactions. MD simulations support that the catalytic residue, His41, has a neutral side chain with a protonated delta position. An absolute binding energy (ΔG) of – 42 kJ mol^{-1} for the protein–ligand (Mpro–N3) complex has been calculated using the potential-of-mean-force (geometrical) approach. Furthermore, the relative binding energies were computed for the top docking results. Our results suggest several promising approved and bioactive inhibitors of SARS-CoV-2 Mpro as follows: a bioactive compound, ChEMBL275592, which has the best MM/GBSA binding energy; the second-best compound, montelukast, is an approved drug used in the treatment of asthma and allergic rhinitis; the third-best compound, ChEMBL288347, is a bioactive compound. Bromocriptine and saquinavir, are other approved drugs that also demonstrate stability in the active site of Mpro, albeit their relative binding energies are low compared to the N3 inhibitor. This study provides useful insights into de novo protein design and novel inhibitor development, which could reduce the cost and time required for the discovery of a potent drug to combat SARS-CoV-2.

3.2 Introduction

Coronaviruses can provoke infectious diseases in humans and animals. Coronavirus disease 2019 (COVID-19) is caused by a novel severe acute respiratory syndrome, SARS-CoV-2, which has spread as a worldwide pandemic. Patients infected with this disease present major symptoms including, high fever, rhinorrhea, cough, sore throat, pneumonia and ultimately, death in severe cases.[1, 2] Globally, according to the world health organization (WHO), there have been 173,674,509 confirmed cases of COVID-19, including 3,744,408 deaths as of June 6, 2021. Most of these cases and deaths are from Europe and the Americas.

Coronaviruses were named due to their protein spikes that have a crown-like shape.[3] The coronavirus genome encodes several proteins, such as the spike, Mpro

(also known as 3-chymotrypsin-like cysteine protease, 3CLpro), and RNA-dependent RNA polymerase (RdRp).[4] Different approaches are being investigated for the development of useful drugs to fight against SARS-CoV-2. Das et al presented an overview of therapeutic strategies and approaches in combating COVID-19.[5] Developing inhibitors of viral Mpro is one of the promising approaches. Mpro is essential for viral replication by facilitating the cleavage of viral peptides into smaller functional units.[6] Consequently, drugs that target the Mpro would cease the replication process and prevent viral infection. A study by Liu et al comprehensively viewed coronavirus Mpro inhibitors that have been developed from 2010 to 2020.[7] More recently, 15 drugs are being tested to cure COVID-19 including virus protease inhibitors.[8] However, albeit the preliminary results are promising, there were issues in the design of the study. According to WHO, there is no specific medicine to treat COVID-19 yet.

In silico drug design has been playing a vital role in modern drug therapies against infectious diseases.[9–11] Currently, enormous efforts and approaches are being pursued for the discovery of inhibitors against SARS-CoV-2 Mpro by employing high performance computational resources. Nutho et al studied two HIV-1 protease inhibitors specifically, lopinavir and ritonavir, by MD simulations and relative binding energy calculations.[12] MD simulations, molecular docking, and structure-activity relationship were used for the discovery of new hydroxyethylamine analogs against the Mpro.[13] Docking screening of approved drugs and drug candidates in clinical trials,[14] and medicinal plants[15] were also conducted along with MD simulations. Molecular docking, fast pulling of ligand, and free energy perturbation calculations were also performed to investigate potential inhibitors of SARS-CoV-2 Mpro.[16] Moreover, both MD simulations and molecular docking were employed to explore the Mpro inhibitory of 19 marketed drugs,[17] and to repurpose protease inhibitors[18] and anti-HIV drugs.[19] Based on a new refined crystal structure of SARS-CoV-2 Mpro [Protein Data Bank (PDB) entry 6Y2G], Tsuji performed a structure-based molecular docking using the ChEMBL database and reported 28 bioactive compounds in addition to 64 potential drugs, including approved, clinical, and pre-clinical compounds.[20] Moreover, virtual screening of antiviral compounds targeting the spike, Mpro, and the SARS-CoV-2 receptor binding domain (RBD)–angiotensin-converting enzyme 2 (ACE2) complex of SARS-CoV-2 shows that PC786, an antiviral polymerase inhibitor, has a good binding affinity to all the targets.[21] Table 3.1 summarizes a list of recent papers of *in silico* studies for the discovery of inhibitors against SARS-CoV-2

Table 3.1: Recent *In silico* studies reported in the literature for the discovery of inhibitors against SARS-CoV-2 Mpro

In silico approach	Screened drugs	Citation
MD simulations, RBE,[a] and PIEDA[b]	lopinavir and ritonavir	Nutho et al[12]
MD simulations, docking, and SAR[c]	hydroxyethylamine analogs	Kumar et al[13]
MD simulations, docking, and RBE[a]	approved and clinical drugs	Wang[14]
MD simulations and docking	medicinal plants	Qamar et al[15]
Structure-based molecular docking	medicinal plants	Shawky et al[22]
Structure-based molecular docking	*Salvadora persica* flavonoids	Owis et al[23]
MD simulations, docking, fast-pulling of ligand, and ABFE[d]	natural compounds	Ngo et al[16]
MD simulations and docking	19 marketed drugs	Huynh et al[17]
MD simulations and docking	protease inhibtors	Havranek et al[18]
MD simulations, docking, and RBE[a]	antiviral compounds	Sang et al,[19] Panda[21]
Structure-based molecular docking	ChEMBL database	Tsuji[20]
Fragment molecular orbital based interaction analysis	N3 inhibitor	Hatada[24]
Catalytic mechanism of the Mpro by QM/MM methods	polypeptide Ac-Val-Lys-Leu-Gln-ACC	Swiderek and Moliner[25]

[a]RBE stands for relative binding energy calculated by MM/GBSA or MM/PBSA or both. [b]PIEDA stands for pair interaction energy decomposition analysis. [c]SAR stands for structure activity relationship. [d]ABFE stands for absolute binding free energy.

Mpro.

In this work, we will focus on a newly released protein crystal structure of the SARS-CoV-2 Mpro.[26] This protein is a dimer that includes two protomers; each protomer has three domains. Domains I and II, residues 8-184, have an antiparallel β-barrel structure. Domain III, residues 201-303, has five α-helices. The extended loop, residues 185-200, connects Domains II and III. Furthermore, this protein has a catalytic dyad, His41 and Cys145, and the substrate binding site is in a cleft between Domains I and II. In this paper, we performed an integrated computational protocol including ligand-based and structure-based molecular screening, molecular dynamics

simulations, and binding energy calculations to facilitate the identification of promising candidate drugs to treat COVID-19.

3.3 Methods and Computational Details

The initial coordinates of one protomer of the SARS-CoV-2 Mpro was retrieved from the RCSB [PDB entry 6LU7] determined at 2.16 Å resolution with no missing residues.[26] The cocrystalized ligand (named N3) of SARS-CoV-2 Mpro was used to conduct the ligand-based virtual screening. The N3 ligand is a peptidomimetic potent inhibitor and it was also found as a complex with earlier coronaviruses Mpro such as IBV,[27] HCoV-HKU1,[28] SARS-CoV,[29] HCoV-NL63,[30] FIPV,[31] and PEDV.[32]

3.3.1 Hierarchical Virtual Screening and Docking

In the PDB crystal structure, the N3 ligand was covalently bonded to Cys145. We constructed the free ligand by breaking the covalent bond and making an α,β-unsaturated ketone using the molecular structure editor (maestro)[33]. We minimized the N3 ligand using the MMFF94s force field.[34] We then screened the data sets from both the DrugBank[35] and ChEMBL[36] libraries based on the preprocessed N3 ligand. For ligand-based screening, a novel fully flexible high-throughput 3D molecular similarity approach (Screen3D algorithm)[37] was performed as implemented in the BRUSELAS server.[38]

The top 200 compounds (the top 100 from each library) that are structurally similar to the N3 ligand were advanced to the next hierarchical filter, docking screening. OpenBabel software[39] was used to generate and minimize conformations from the top 200 screened compounds. These compounds were docked into a preprocessed protein pocket by utilizing the AutoDock Vina package.[40] It has been shown that AutoDock Vina has an effective scoring function in terms of accuracy and performance.[41] The grid cell of 18.0 Å, 21.3 Å, and 24.3 Å in the x, y, and z directions, respectively, was built for docking calculations. This grid cell is located around the active site of the Mpro, centroid to residues His41, Met49, Phe140, Leu141, Asn142,

Gly143, Cys145, His164, Met165, Glu166, Leu167, Pro168, His172, Gln189, and Thr190.

3.3.2 Molecular Dynamics (MD) Simulations

The top 8 docking results were advanced to all-atom MD simulations to study the relative stability of the protein–ligand interactions, and to screen a set of compounds for further binding energy calculations. All the simulations were done using the NAMD 2.13 package[42, 43] and the CHARMM36 force field.[44] The parameters for the N3 ligand and the top 8 docking compounds were generated using the CHARMM general force field (CGenFF).[45] A protomer of the Mpro has a total of 306 residues.[26] The protonation state of the titratable residues were assigned at pH 7.4 exploiting the H++ web server.[46] It should be pointed out that the catalytic residue His41 can adopt three different protonation states: neutral HSD (δ-nitrogen protonated), neutral HSE (ϵ-nitrogen protonated), and protonated HSP (both δ- and ϵ-nitrogens protonated). Therefore, three MD simulations were run to explore the effect of the protonation states of His41 on the stability of the active site. The TIP3P explicit solvation model was used, and the periodic boundary conditions were set with dimensions of 115.2 $Å^3$. Afterward, the system was neutralized using four sodium (Na^+) ions. The MD protocols involved minimization, annealing, equilibration, and production. The atoms of the protein backbone were restrained in the minimization and annealing simulations, while the Cα atoms of the protein were restrained in the 1 ns equilibration simulation. However, no atoms were restrained in the 100 ns MD production simulation. The isothermal-isobaric (NPT) ensemble and a 2 fs time step of integration was chosen for all MD simulations. Through the 100 ns of MD production, the pressure was set at 1 atm using the Nosé-Hoover Langevin piston barostat[47, 48] with the Langevin piston decay of 0.2 ps and a period of 0.4 ps. The temperature was set at 298.15 K using the Langevin thermostat[49] with a damping frequency of 1 ps^{-1}. A distance cutoff of 10.0 Å was applied to short-range nonbonded interactions with a pair list distance of 12 Å, and Lennard Jones interactions were smoothly truncated at 8.0 Å. Long-range electrostatic interactions were treated using the particle-mesh Ewald (PME) method,[50, 51] where a grid spacing of 1.0 Å was used for all simulation cells. All covalent bonds involving hydrogen atoms were constrained using the SHAKE algorithm.[52] For consistency, we have applied the same protocol for all MD

simulations.

3.3.3 Binding Energy Calculation

Starting from the equilibrated protein–ligand complex, we calculated the absolute binding energy of the Mpro–N3 complex using the geometrical energy approach. It has been shown that the geometrical approach accurately predicts protein–ligand binding energies.[53, 54] We used the default set up of the binding free energy estimator as described by Chipot and coworkers.[55] More details on theoretical background of the geometrical (i.e., potential-of-mean-force) free energy calculations can be obtained elsewhere.[54] In addition, we collected a total of 1000 snapshots extracted consistently from the 100 ns of MD production to calculate the relative protein–ligand binding energy of the top docking results. The one-average molecular mechanics generalized Born surface area (MM/GBSA) approach[56, 57] was used for the relative binding energy calculations, in which the ligand (L) binds to the protein receptor (R) to form the complex (RL),

$$\Delta G_{bind} = \Delta G_{RL} - \Delta G_R - \Delta G_L$$

which can be represented by contributions of different interactions,

$$\Delta G_{bind} = \Delta H - T\Delta S = \Delta E_{MM} + \Delta G_{sol} - T\Delta S$$

where the changes in the gas phase molecular mechanics (ΔE_{MM}), solvation Gibbs energy (ΔG_{sol}), and conformational entropy ($-T\Delta S$) are determined as follows: ΔE_{MM} is the sum of the changes in the electrostatic energies ΔE_{ele}, the van der Waals energies ΔE_{vdW}, and the internal energies ΔE_{int} (bonded interactions); ΔG_{sol} is the total of both the polar solvation (calculated by generalized Born model) and the nonpolar solvation (calculated using the solvent-accessible surface area); $-T\Delta S$ is calculated by the normal mode analysis. The solvent dielectric constant of 78.5 and the surface tension constant of 0.021 kJ mol^{-1} Å^{-2} were used for MM/GBSA calculations.

Table 3.2: Top 8 docking results for SARS-CoV-2 Mpro

Compound ID	Generic name	Number of conformations that have binding affinity of ≤ -33 kJ mol^{-1}
ChEMBL275592	NA	9
DB01232	saquinavir	9
DB00471	montelukast	7
DB00549	zafirlukast	7
ChEMBL288347	NA	6
DB00559	bosentan	6
DB01200	bromocriptine	5
DB08995	doismin	5

3.4 Results and Discussion

We performed a ligand-based virtual screening of approved drugs and bioactive compounds from both the DrugBank and ChEMBL databases. The top 100 screened compounds from each library are advanced to flexible molecular docking using AutoDock Vina. Nine conformations from each compound were generated through a flexible docking. Docking score was chosen as the measure of the binding affinity to rank the poses of the 200 compounds. Our selection of the top 8 compounds were based on compounds that have at least five conformations (docking modes) with a docking score of ≤ -33 kJ mol^{-1} (-8 kcal mol^{-1}). Docking results of the 200 compounds with different conformations are provided in Table B.1 in Appendix B. Docking results of the top 8 compounds for SARS-CoV-2 Mpro are listed in Table 3.2. The structures of the top 8 compounds are shown in Fig. 3.1. It should be pointed out that the bioactive compounds, ChEMBL275592 and ChEMBL288347, have Lipinski's rule of five violations of 1 and 2, respectively.

Next, the top 8 docking results were advanced for MD simulations. Many studies have validated the role of MD simulations for the improvement of docking results.[58, 59] Before launching MD simulations on the top docking results, three MD simulations of SARS-CoV-2 Mpro complexed with the N3 ligand were carried out to explore the plausible protonation states of the catalytic His41, as illustrated earlier in the methods section. His41 is a well-preserved residue amongst various viruses including hepatitis C virus (HCV), MERS-CoV, SARS-CoV, and SARS-CoV-2.[14] The three MD simulations were labeled as follows: neutral HSD (Model 1), neutral HSE (Model 2), and protonated HSP (Model 3). Control of the structure stability of the three models was

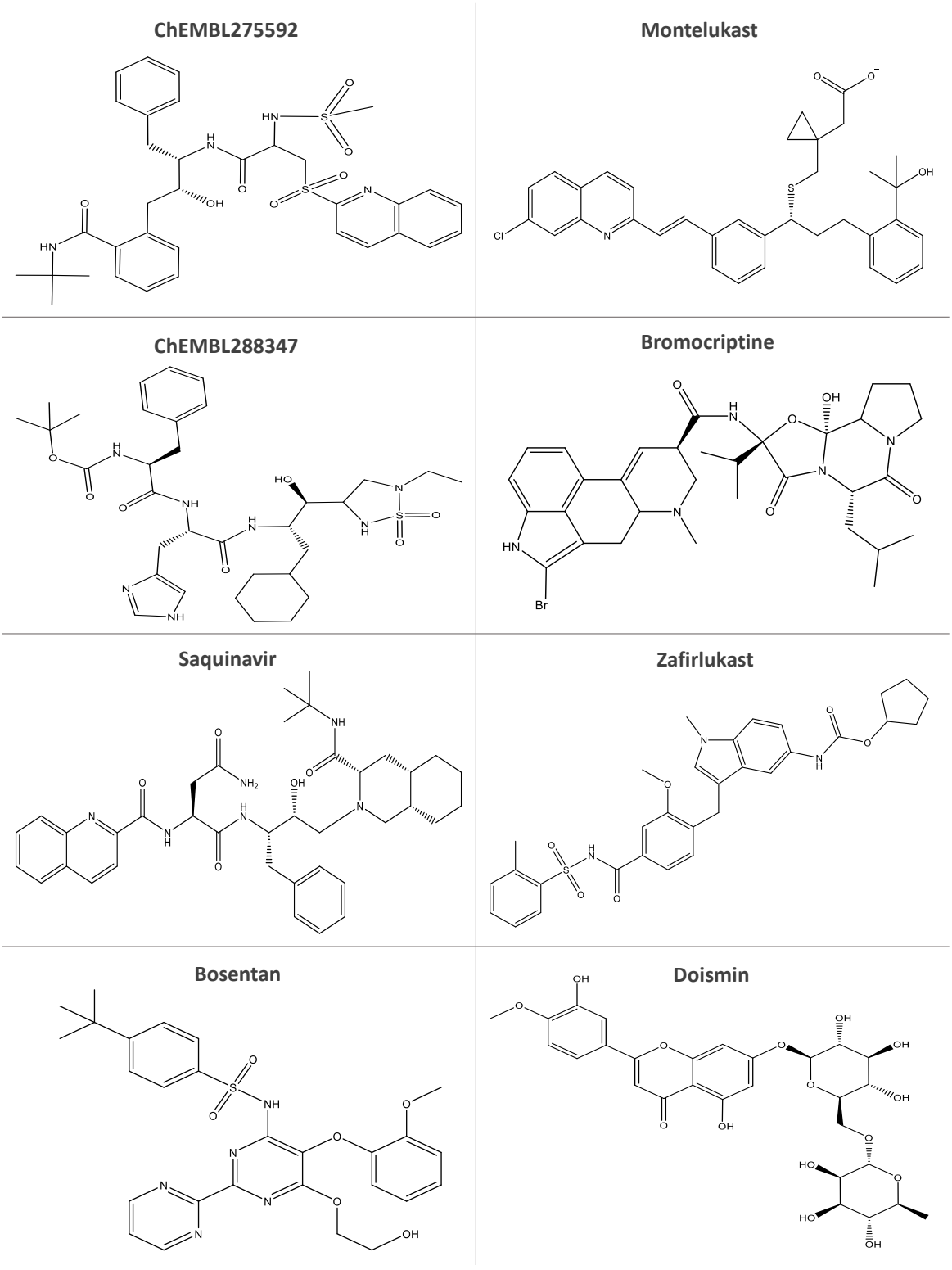

Figure 3.1: Two-dimensional structures of the selected top 8 compounds

achieved by the root-mean-square deviation (RMSD) over protein backbone atoms, and by the root-mean-square fluctuation (RMSF). In addition, the Mpro–N3 hydrogen bond interactions were also analyzed during the 100 ns NPT ensemble. Fig. 3.2 shows the RMSD, RMSF, and hydrogen bond analyses of the protein–ligand complex for the three models.

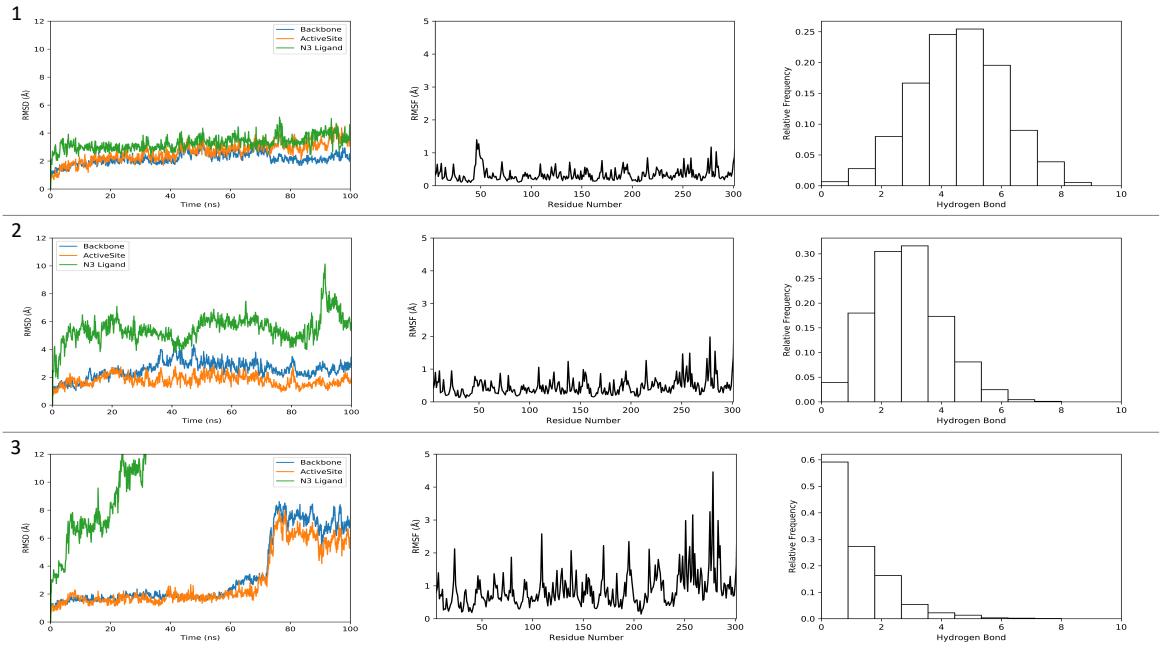

Figure 3.2: From left to right: RMSD, RMSF, and hydrogen bond interactions of the Mpro–N3 complex during 100 ns MD simulations. Moldel 1 (top), Model 2 (middle), and Model 3 (bottom).

Unambiguously, amongst the three models, Model 1 shows a modest structural stability in terms of the RMSD of both the Mpro and N3 ligand, and the RMSF analysis. Moreover, the intermolecular interaction of the Mpro–N3 complex has an average of five hydrogen bonds (see the top histogram in Fig. 3.2). The stability of the Mpro–N3 complex is mainly due to the hydrogen bonds between the N3 ligand and residues His41, Gly143, Glu166, and Gln189 of the Mpro, besides the hydrophobic interactions. These results are in concert with recent experimental and theoretical work.[24, 26, 60] Fig. 3.3 represents the pose of the N3 ligand inside the pocket of the Mpro.

The RMSD and the RMSF of the protein backbone of Model 2 is comparable with Model 1, however, the N3 ligand in Model 2 was less strongly bound inside the

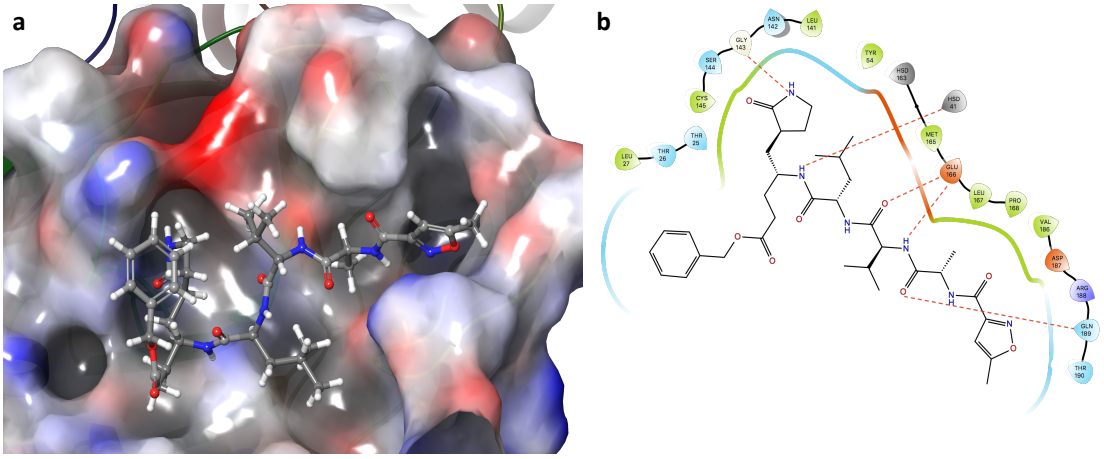

Figure 3.3: (a) Representative pose of the N3 ligand in the Mpro pocket. The protein surface is colored based on the electrostatic potential. (b) Hydrogen bond interactions (red dashed line) of the N3 ligand in complex with the Mpro.

Mpro pocket than Model 1 (see Fig. 3.2). Model 2 has an average of three hydrogen bonds between the N3 ligand and the Mpro. In Model 3, the N3 ligand has left the binding pocket of the Mpro during the MD simulations (see the green line of the RMSD analysis at the bottom of Fig. 3.2). Thus, Model 1 is considered as a starting point for MD simulations for the top docking results. In other words, His41 is set as a neutral form with a protonated delta position (HSD type of CHARMM format), and this model agrees with the common reaction mechanism of cysteine protease.[61] The optimal binding pose of the Mpro–N3 complex of Model 1 was further assessed by absolute binding energy calculations using the geometrical approach. It should be mentioned that the N3 is a Michael acceptor inhibitor, which means that the inhibitor forms a reversible complex (Mpro–N3) under the equilibrium binding constant K_{eq}. It then undergoes a nucleophilic attack by Cys145 of the Mpro active site, forming a stable covalent bond. The latter step is controlled by the inactivation rate constant, which is beyond the scope of this paper. To calculate K_{eq}, the different contributions arising from the geometrical restraints were computed, either in the bound state, or in the unbound state.[54, 55] The final absolute binding energy, $\Delta G = -1/\beta\ lnK_{eq}$, has a value of – 42 kJ mol^{-1}. Yet, no experimental binding energy was reported for the SARS-CoV-2 Mpro. Nevertheless, our results are comparable to experimental binding energies of similar protease–inhibitor systems. Based on the experimental inhibitory constant (K_i), HCoV-NL63,[30] SARS-CoV,[62] and HCoV-229E[62] have the Mpro–N3 binding energies of – 28, – 29, and –33 kJ mol^{-1}, respectively. Therefore,

Table 3.3: MD results and relative binding energies of the top 8 docking compounds and antiviral drugs

Compound	MD structure stability	Contact area (Å^2)[a]	MMGBSA binding energies (kJ mol^{-1})
ChEMBL275592	stable	395 ± 48	-158 ± 41
montelukast	stable	433 ± 34	-154 ± 16
ChEMBL288347	stable	411 ± 42	-144 ± 23
bromocriptine	stable	354 ± 44	-121 ± 14
saquinavir	stable	362 ± 39	-117 ± 16
zafirlukast	unstable	251 ± 66	-73 ± 20
bosentan	unstable	219 ± 137	-59 ± 45
doismin	unstable	305 ± 76	-57 ± 29
lopinavir	stable	395 ± 60	-116 ± 23
ritonavir	stable	392 ± 67	-115 ± 17
remdesivir	stable	396 ± 62	-87 ± 17

[a]Averaged contact area between compounds and the Mpro during the 100 ns NPT ensemble

our predicted results conclude that the SARS-CoV-2 Mpro has relatively a higher binding affinity to the N3 inhibitor than the other Coronaviruses.

Using the same protocol as Model 1, MD simulations were carried out for the top 8 docking compounds to investigate their stability inside the Mpro pocket. The RMSD, RMSF, and hydrogen bond analyses of the top 8 docking compounds complexed individually with the Mpro were performed (see Figures B.1–B.3 in Appendix B). The RMSD values of ChEMBL275592, montelukast, ChEMBL288347, bromocriptine, and saquinavir systems increased at the beginning of the simulation then remained stable until the end of the simulation. These compounds have reliable MMGBSA binding energies relative to the known N3 inhibitor that has a value of -150 ± 24 kJ mol^{-1} calculated at MMGBSA method. The poses of these stable compounds inside the pocket of the Mpro are provided (see Figure B.4 in Appendix B). The rest of the docking compounds, zafirlukast, bosentan, and doismin, lack the stability inside the Mpro pocket, consequently, these compounds have poor binding energies relative to the known N3 inhibitor. For validation, we normalized the results of the top compounds with antiviral drugs such as, lopinavir, ritonavir, and remdesivir. MD simualtions analyses and the poses of these antiviral drugs inside the pocket of the Mpro are provided (see Figures B.6–B.7 in Appendix B). Table 3.3 lists the MD results and the MMGBSA relative binding energies for the top docking compounds and selected antiviral drugs.

The averaged contact area analysis was calculated based on the surface area of a ligand that is exposed to residues of a protein.[63] Table 3.4 summarizes the contact area analysis for compounds that have good stability inside the binding site of the Mpro through the 100 ns MD simulations. Snapshots of the last frame of simulated systems are depicted in Fig. 3.4. Analyses of the time-evolution of the contact area are also provided (see Figure B.5 in Appendix B). We found that residues Thr25, His41, Ser46, Met49, Asn142, Cys145, Met165, Glu166, Pro168, and Gln189 have a good contact area with the top five compounds. Wang studied the common significant hot spot residues of the Mpro; these residues are His41, Met49, Asn142, His164, Met165, Glu166, and Gln189, which are in agreement with our results.[14]

Table 3.4: Averaged contact area (Å^2) between compounds and active site residues of the Mpro during the 100 ns NPT ensemble

Residue	N3	ChEMBL–275592	montelukast	ChEMBL–288347	bromocriptine	squinavir	lopinavir	ritonavir	remdesivir
Thr25	14	19	16	14	12	12	20	10	13
His41	24	15	17	19	6	11	19	16	28
Ser46	2	20	8	32	31	29	28	12	7
Met49	5	27	7	30	24	17	39	66	53
Asn142	44	3	30	16	69	32	28	15	48
Gly143	25	31	19	6	28	6	1	4	23
Cys145	13	14	23	5	18	4	10	6	22
Met165	19	24	55	52	39	14	43	14	40
Glu166	50	49	43	30	20	26	46	23	33
Pro168	53	18	30	40	9	33	32	32	13
Gln189	56	40	43	70	40	83	55	75	28
Ala191	23	16	19	12	0	4	4	11	4

3.5 Conclusions

In this study, the ligand-based screening, structure-based docking screening, MD simulations, and binding energy calculations were conducted based on the Mpro as a drug target. The Mpro–N3 complex has an absolute binding energy of – 42 kJ mol^{-1}. The predicted results suggest that montelukast, ChEMBL275592, and ChEMBL288347 (top 3 compounds) show good inhibitory efficiency on the focused Mpro target. Montelukast is an approved drug that is used to control and prevent breathing problems. Montelukast is currently under clinical trials for the attenuation and prophylaxis of COVID-19 symptoms as listed by U.S. National Library of Medicine.[64] ChEMBL275592 is a bioactive compound that shows an inhibitory activity of 2.8 nM against HIV-1 protease.[65] ChEMBL288347 is also a bioactive compound that shows an inhibitory activity of 1.4 nM through *in vitro* inhibition of purified human renal renin.[66] In addition, bromocriptine and saquinavir may also be candidates for Mpro inhibition. Our findings pave the way for further optimizations and designs of Mpro's inhibitors.

References

(1) Guan, W.-j.; Ni, Z.-y.; Hu, Y.; Liang, W.-h.; Ou, C.-q.; He, J.-x.; Liu, L.; Shan, H.; Lei, C.-l.; Hui, D. S., et al. *New England journal of medicine* **2020**, *382*, 1708–1720.

(2) Huang, C.; Wang, Y.; Li, X.; Ren, L.; Zhao, J.; Hu, Y.; Zhang, L.; Fan, G.; Xu, J.; Gu, X., et al. *The lancet* **2020**, *395*, 497–506.

(3) Stadler, K.; Masignani, V.; Eickmann, M.; Becker, S.; Abrignani, S.; Klenk, H.-D.; Rappuoli, R. *Nature Reviews Microbiology* **2003**, *1*, 209–218.

(4) Liu, C.; Zhou, Q.; Li, Y.; Garner, L. V.; Watkins, S. P.; Carter, L. J.; Smoot, J.; Gregg, A. C.; Daniels, A. D.; Jervey, S., et al. Research and development on therapeutic agents and vaccines for COVID-19 and related human coronavirus diseases, 2020.

(5) Das, G.; Ghosh, S.; Garg, S.; Ghosh, S.; Jana, A.; Samat, R.; Mukherjee, N.; Roy, R.; Ghosh, S. *RSC Advances* **2020**, *10*, 28243–28266.

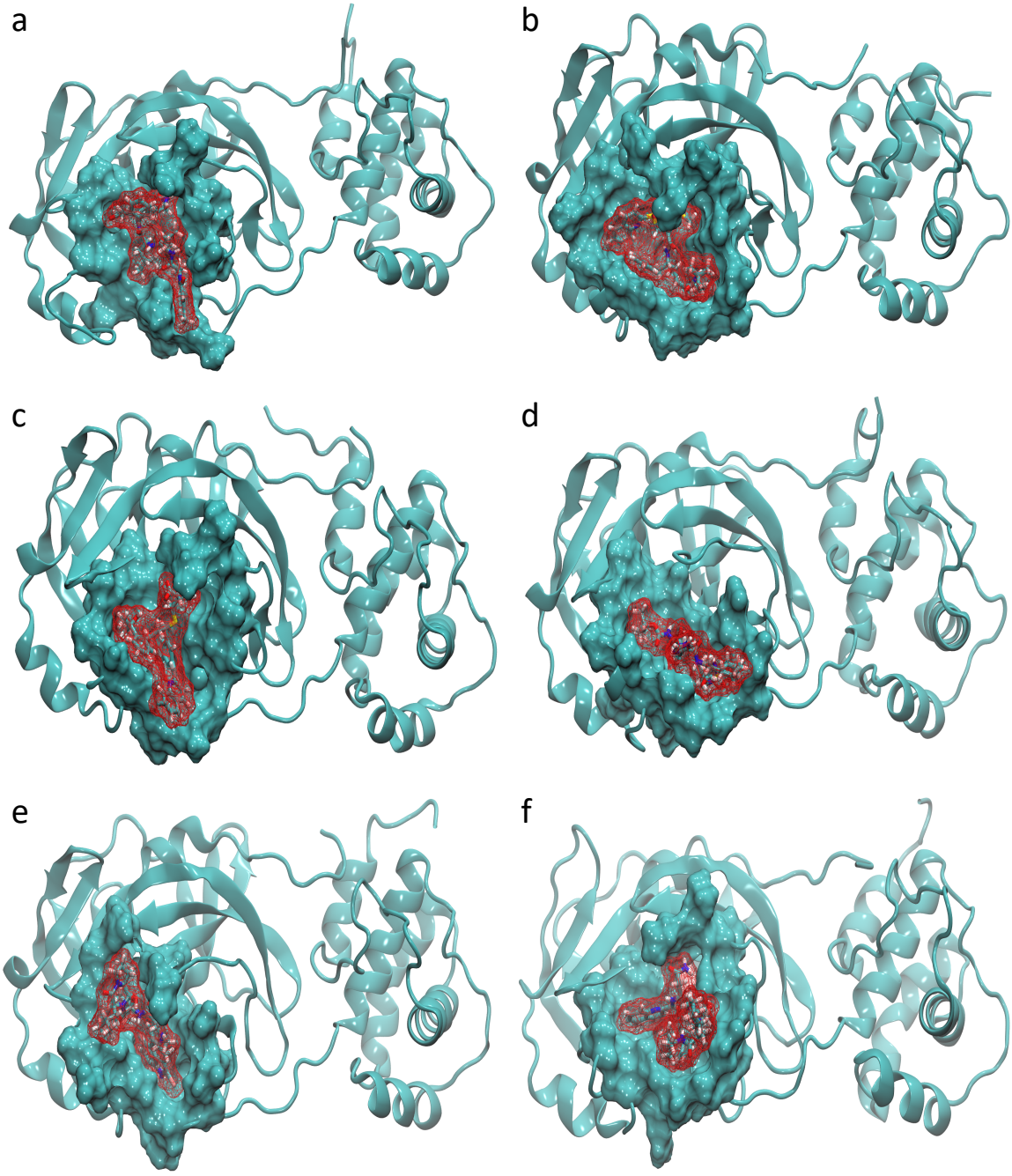

Figure 3.4: Last frame of 100 ns MD simulations of ligands in the Mpro pocket. (a) N3 inhibitor, (b) ChEMBL275592, (c) montelukast, (d) ChEMBL288347, (e) bromocriptine, and (f) saquinavir.

(6) Goetz, D.; Choe, Y.; Hansell, E.; Chen, Y.; McDowell, M.; Jonsson, C.; Roush, W.; McKerrow, J.; Craik, C. *Biochemistry* **2007**, *46*, 8744–8752.

(7) Liu, Y.; Liang, C.; Xin, L.; Ren, X.; Tian, L.; Ju, X.; Li, H.; Wang, Y.; Zhao, Q.; Liu, H., et al. *European Journal of Medicinal Chemistry* **2020**, 112711.

(8) Shaffer, L. *Nature medicine* **2020**, *26*, 2–3.

(9) Macalino, S. J. Y.; Gosu, V.; Hong, S.; Choi, S. *Archives of pharmacal research* **2015**, *38*, 1686–1701.

(10) Njogu, P. M.; Guantai, E. M.; Pavadai, E.; Chibale, K. *ACS infectious diseases* **2016**, *2*, 8–31.

(11) Aminpour, M.; Montemagno, C.; Tuszynski, J. A. *Molecules* **2019**, *24*, 1693.

(12) Nutho, B.; Mahalapbutr, P.; Hengphasatporn, K.; Pattaranggoon, N. C.; Simanon, N.; Shigeta, Y.; Hannongbua, S.; Rungrotmongkol, T. *Biochemistry* **2020**, *59*, 1769–1779.

(13) Kumar, S.; Sharma, P. P.; Shankar, U.; Kumar, D.; Joshi, S. K.; Pena, L.; Durvasula, R.; Kumar, A.; Kempaiah, P.; Poonam; Rathi, B. *Journal of Chemical Information and Modeling* **2020**, *60*, 5754–5770.

(14) Wang, J. *Journal of Chemical Information and Modeling* **2020**, *60*, 3277–3286.

(15) Ul Qamar, M. T.; Alqahtani, S. M.; Alamri, M. A.; Chen, L.-L. *Journal of pharmaceutical analysis* **2020**, *10*, 313–319.

(16) Ngo, S. T.; Pham, N. Q. A.; Le, L.; Pham, D.-H.; Vu, V. *Journal of Chemical Information and Modeling* **2020**, *60*, 5771–5780.

(17) Huynh, T.; Wang, H.; Luan, B. *The journal of physical chemistry letters* **2020**, *11*, 4413–4420.

(18) Havranek, B.; Islam, S. M. *Journal of Biomolecular Structure and Dynamics* **2020**, 1–12.

(19) Sang, P.; Tian, S.-H.; Meng, Z.-H.; Yang, L.-Q. *RSC Advances* **2020**, *10*, 15775–15783.

(20) Tsuji, M. *FEBS Open Bio* **2020**, *10*, 995–1004.

(21) Panda, P. K.; Arul, M. N.; Patel, P.; Verma, S. K.; Luo, W.; Rubahn, H.-G.; Mishra, Y. K.; Suar, M.; Ahuja, R. *Science advances* **2020**, *6*, eabb8097.

(22) Shawky, E.; Nada, A. A.; Ibrahim, R. S. *RSC Advances* **2020**, *10*, 27961–27983.

(23) Owis, A. I.; El-Hawary, M. S.; El Amir, D.; Aly, O. M.; Abdelmohsen, U. R.; Kamel, M. S. *RSC Advances* **2020**, *10*, 19570–19575.

(24) Hatada, R.; Okuwaki, K.; Mochizuki, Y.; Handa, Y.; Fukuzawa, K.; Komeiji, Y.; Okiyama, Y.; Tanaka, S. *Journal of chemical information and modeling* **2020**, *60*, 3593–3602.

(25) Swiderek, K.; Moliner, V. **2020**, *11*, 10626–10630.

(26) Jin, Z.; Du, X.; Xu, Y.; Deng, Y.; Liu, M.; Zhao, Y.; Zhang, B.; Li, X.; Zhang, L.; Peng, C., et al. *Nature* **2020**, 1–5.

(27) Xue, X.; Yu, H.; Yang, H.; Xue, F.; Wu, Z.; Shen, W.; Li, J.; Zhou, Z.; Ding, Y.; Zhao, Q., et al. *Journal of virology* **2008**, *82*, 2515–2527.

(28) Zhao, Q.; Li, S.; Xue, F.; Zou, Y.; Chen, C.; Bartlam, M.; Rao, Z. *Journal of virology* **2008**, *82*, 8647–8655.

(29) Xue, X.; Yang, H.; Shen, W.; Zhao, Q.; Li, J.; Yang, K.; Chen, C.; Jin, Y.; Bartlam, M.; Rao, Z. *Journal of molecular biology* **2007**, *366*, 965–975.

(30) Wang, F.; Chen, C.; Tan, W.; Yang, K.; Yang, H. *Scientific reports* **2016**, *6*, 22677.

(31) Wang, F.; Chen, C.; Liu, X.; Yang, K.; Xu, X.; Yang, H. *Journal of Virology* **2016**, *90*, 1910–1917.

(32) Wang, F.; Chen, C.; Yang, K.; Xu, Y.; Liu, X.; Gao, F.; Liu, H.; Chen, X.; Zhao, Q.; Liu, X., et al. *Journal of Medicinal Chemistry* **2017**, *60*, 3212–3216.

(33) Maestro, Schrödinger Release 11.8.0; Schrödinger, LLC: New York, NY, 2019.

(34) Halgren, T. A. *Journal of Computational Chemistry* **1999**, *20*, 720–729.

(35) Law, V.; Knox, C.; Djoumbou, Y.; Jewison, T.; Guo, A. C.; Liu, Y.; Maciejewski, A.; Arndt, D.; Wilson, M.; Neveu, V., et al. *Nucleic acids research* **2014**, *42*, D1091–D1097.

(36) Gaulton, A.; Hersey, A.; Nowotka, M.; Bento, A. P.; Chambers, J.; Mendez, D.; Mutowo, P.; Atkinson, F.; Bellis, L. J.; Cibrián-Uhalte, E., et al. *Nucleic acids research* **2017**, *45*, D945–D954.

(37) Kalászi, A.; Szisz, D.; Imre, G.; Polgar, T. *Journal of chemical information and modeling* **2014**, *54*, 1036–1049.

(38) Banegas-Luna, A. J.; Cerón-Carrasco, J. P.; Puertas-Martın, S.; Pérez-Sánchez, H. *Journal of chemical information and modeling* **2019**, *59*, 2805–2817.

(39) O'Boyle, N. M.; Banck, M.; James, C. A.; Morley, C.; Vandermeersch, T.; Hutchison, G. R. *Journal of cheminformatics* **2011**, *3*, 33.

(40) Vina, A. *J. Comput. Chem* **2010**, *31*, 455–461.

(41) Wang, Z.; Sun, H.; Yao, X.; Li, D.; Xu, L.; Li, Y.; Tian, S.; Hou, T. *Physical Chemistry Chemical Physics* **2016**, *18*, 12964–12975.

(42) Phillips, J. C.; Braun, R.; Wang, W.; Gumbart, J.; Tajkhorshid, E.; Villa, E.; Chipot, C.; Skeel, R. D.; Kale, L.; Schulten, K. *Journal of computational chemistry* **2005**, *26*, 1781–1802.

(43) Ribeiro, J. V.; Bernardi, R. C.; Rudack, T.; Stone, J. E.; Phillips, J. C.; Freddolino, P. L.; Schulten, K. *Scientific reports* **2016**, *6*, 1–14.

(44) Best, R. B.; Zhu, X.; Shim, J.; Lopes, P. E.; Mittal, J.; Feig, M.; MacKerell Jr, A. D. *Journal of chemical theory and computation* **2012**, *8*, 3257–3273.

(45) Yu, W.; He, X.; Vanommeslaeghe, K.; MacKerell Jr, A. D. *Journal of computational chemistry* **2012**, *33*, 2451–2468.

(46) Anandakrishnan, R.; Aguilar, B.; Onufriev, A. V. *Nucleic acids research* **2012**, *40*, W537–W541.

(47) Nosé, S.; Klein, M. *Molecular Physics* **1983**, *50*, 1055–1076.

(48) Nosé, S. *Molecular physics* **1984**, *52*, 255–268.

(49) Grest, G. S.; Kremer, K. *Physical Review A* **1986**, *33*, 3628.

(50) Darden, T.; York, D.; Pedersen, L. *The Journal of chemical physics* **1993**, *98*, 10089–10092.

(51) Essmann, U.; Perera, L.; Berkowitz, M. L.; Darden, T.; Lee, H.; Pedersen, L. G. *The Journal of chemical physics* **1995**, *103*, 8577–8593.

(52) Ryckaert, J.-P.; Ciccotti, G.; Berendsen, H. J. *Journal of computational physics* **1977**, *23*, 327–341.

(53) Gumbart, J. C.; Roux, B.; Chipot, C. *Journal of chemical theory and computation* **2013**, *9*, 794–802.

(54) Fu, H.; Cai, W.; Hénin, J.; Roux, B.; Chipot, C. *Journal of Chemical Theory and Computation* **2017**, *13*, 5173–5178.

(55) Fu, H.; Gumbart, J. C.; Chen, H.; Shao, X.; Cai, W.; Chipot, C. *Journal of chemical information and modeling* **2018**, *58*, 556–560.

(56) Genheden, S.; Ryde, U. *Proteins: Structure, Function, and Bioinformatics* **2012**, *80*, 1326–1342.

(57) Wang, E.; Sun, H.; Wang, J.; Wang, Z.; Liu, H.; Zhang, J. Z.; Hou, T. *Chemical reviews* **2019**, *119*, 9478–9508.

(58) Salmaso, V.; Moro, S. *Frontiers in pharmacology* **2018**, *9*, 923.

(59) Guterres, H.; Im, W. *Journal of Chemical Information and Modeling* **2020**, *60*, 2189–2198.

(60) Ryunosuke, Y.; Nobuaki, Y.; Masakazu, S. *Scientific Reports* **2020**, *10*, 12493.

(61) Otto, H.-H.; Schirmeister, T. *Chemical reviews* **1997**, *97*, 133–172.

(62) Yang, H.; Xie, W.; Xue, X.; Yang, K.; Ma, J.; Liang, W.; Zhao, Q.; Zhou, Z.; Pei, D.; Ziebuhr, J., et al. *PLoS Biol* **2005**, *3*, e324.

(63) Scheurer, M.; Rodenkirch, P.; Siggel, M.; Bernardi, R. C.; Schulten, K.; Tajkhorshid, E.; Rudack, T. *Biophysical journal* **2018**, *114*, 577–583.

(64) `http://clinicaltrials.gov/ct2/show/NCT04389411`.

(65) Jungheim, L. N.; Shepherd, T. A.; Baxter, A. J.; Burgess, J.; Hatch, S. D.; Lubbehusen, P.; Wiskerchen, M.; Muesing, M. A. *Journal of medicinal chemistry* **1996**, *39*, 96–108.

(66) Rosenberg, S. H.; Dellaria, J. F.; Kempf, D. J.; Hutchins, C. W.; Woods, K. W.; Maki, R. G.; De Lara, E.; Spina, K. P.; Stein, H. H. *Journal of medicinal chemistry* **1990**, *33*, 1582–1590.

"The most enjoyable part of science is doing it. It is sometimes very frustrating but extremely rewarding when you suddenly understand something"

—Kip Thorne

4

Discovery of Potent Inhibitors for SARS-CoV-2's Spike Protein

This chapter is adapted from: Abu-Saleh, A.A.A.; Yadav, A.; Poirier, R.A. Accelerating the Discovery of the Beyond Rule of Five Compounds That Have High Affinities Toward SARS-CoV-2 Spike RBD. *ChemRxiv*, **2020**, DOI: 10.26434/chemrxiv.14130353.v2.

4.1 Abstract

The battle against SARS-CoV-2 coronavirus is the focal point for the global pandemic that has affected millions of lives worldwide. The need for effective and selective therapeutics for the treatment of the disease caused by SARS-CoV-2 is critical. Herein, we performed computational *de novo* design incorporating molecular docking studies,

molecular dynamics simulations, absolute binding energy calculations, and steered molecular dynamics simulations for the discovery of potential compounds with high affinity towards SARS-CoV-2 spike RBD. By leveraging ZINC15 database, a total of 1282 in-clinical and FDA approved drugs were filtered out from nearly 0.5 million protomers of relatively large compounds (MW $>$ 500, and LogP $\leq$ 5). Our results depict plausible mechanistic aspects related to the blockage of SARS-CoV-2 spike RBD by the top hits discovered. We found that the most promising candidates, namely, ZINC95628821, ZINC95617623, ZINC3979524, and ZINC261494658, strongly bind to the spike RBD and interfere with the human ACE2 receptor. These findings accelerate the rational design of selective inhibitors targeting the spike RBD protein of SARS-CoV-2.

4.2 Introduction

The severe acute respiratory syndrome coronavirus 2 (SARS-CoV-2) that emerged in late 2019 has caused serious illness and death all over the world. COVID-19, a disease caused by SARS-CoV-2, led the world health organization (WHO) to announce a global pandemic on March 11, 2020. To date, about 170 million infections and more than three million deaths have been reported by the WHO, and the numbers continue to rise.[1] Among several vaccine candidates, three vaccines made by Pfizer-BioNTech, Moderna, and johnson & johnson companies were approved by the U.S. food and drug administration (FDA) for an emergency use against COVID-19. Moreover, veklury (remdesivir), an antiviral drug, has also been approved by the U.S. FDA for the use as a treatment for COVID-19 in adults and pediatric patients (12 years of age and older) requiring hospitalization. Although studies reported that remdesivir failed to show clinical benefits for moderately severe COVID-19 patients,[2, 3] it is the only drug that has been approved so far for COVID-19 by the U.S. FDA. Therefore, accelerating the discovery of a safe and an effective COVID-19 medication is a must to control the pandemic.

The coronavirus genome encodes distinct structural and nonstructural proteins. The structural proteins (i.e., the membrane, the envelop, the spike, and the nucleocapsid) are responsible for key functions such as host infection,[4] membrane fusion,[5] self-assembly,[6] release of virus-like particles,[7] and other functions.[8] The

nonstructural proteins facilitate viral replication-transcription processes.[9] The extensive amount of ongoing research is mainly focused on both non-structural and structural proteins of SARS-CoV-2 as drug targets in order to develop effective therapeutics for COVID-19.[10–16]

Among structural proteins, the spike protein is the key machinery that empowers virus entry into the host cell.[17] Structural characterization of the spike protein would give atomic-level information to guide structure-based drug design. Recently, crystallographic and cryo-EM methods have been utilized to determine various structures and conformational states of the SARS-CoV-2 spike proteins.[5, 17, 18]. Amaro and coworkers have carried out massive molecular dynamics (MD) simulations to promote and extend the available structural data.[19] Moreover, Choi et al performed MD simulations of the spike protein in a viral bilayer.[20] These computational results added a detailed insight on the structural and dynamics of the full-length glycosylated SARS-CoV-2 spike protein at an atomic level.[19]

Detailed mechanisms of the cell entry of SARS-CoV-2 have been recently investigated.[5, 21, 22] The spike protein has two subunits S1 and S2, which are critical for receptor recognition and membrane fusion, respectively. The S1 contains the receptor-binding domain (RBD) of the viral spike that specifically binds to the human angiotensin-converting enzyme 2 (hACE2). The RBD can be in either an up conformation, which is the receptor-accessible state (i.e., enables binding to the host receptor), or a down conformation, which is the receptor-inaccessible state.[17, 21] Gur et al investigated conformational dynamics and the transition pathway between down to up states of the spike protein by using all-atom MD simulations.[23] For membrane fusion, host cell proteases cleave SARS-CoV-2 spikes at the S1/S2 boundary followed by structural changes of the S2 that promote a host cell entry.[21, 24, 25] Interestingly, experimental results have revealed that SARS-CoV-2 RBD has stronger hACE2 binding affinity than that possessed by the previous SARS-CoV RBD. However, the entire SARS-CoV-2 spike has hACE2 binding affinity similar to or lower than SARS-CoV-2 spike.[18, 21, 26, 27] Moreover, a computational study of the RBD -accessible and -inaccessible conformations and their binding strength to the hACE2 is in agreement with the experimental findings.[28] Therefore, the RBD is considered as a key target for designing and developing compounds that suppress the virus entry into the human cell.

Different approaches have been conducted that are based on interfering with the RBD binding to the hACE2 including neutralizing antibodies,[29–31] decoy proteins,[32] miniproteins,[33] peptides,[34–40] and stapled hACE2 peptides.[41] In addition, many studies have explored drug repurposing or repositioning of vast chemical compounds such as FDA approved drugs,[42–44] antivirals,[45, 46] phytochemicals,[47] essential free fatty acids,[48] and natural products[49, 50] for the sake of disrupting the RBD–hACE2 binding. Designing compounds for inhibiting the hACE2 active site has also been reported.[51]

As far as we are aware, no high-throughput virtual screening has been conducted in relatively large molecules in the "beyond rule of 5" chemical space that have high RBD binding affinity. Herein, we performed a comprehensive computational protocol, which incorporates molecular docking, MD simulations, absolute binding energy calculations, and steered MD simulations for the discovery of relatively large compounds that would bind to SARS-CoV-2 spike RBD very tightly, therefore, blocking viral attachment to the host cell.

4.3 Computational Methods

4.3.1 Model System Preparation

The initial structure of SARS-CoV-2 RBD bound to the hACE2 was retrieved from the RCSB protein data bank (PDB entry 6LZG).[5] The protonation states of the titratable residues were determined using the H++ Web server under the physiological pH.[52] Moreover, salinity, internal and external dielectric constants were set to be 0.15, 10.0, and 80.0 respectively.

4.3.2 Molecular Docking

3-D chemical structures (MW $>$ 500, and LogP $\leq$ 5) were retrieved from ZINC15 database,[53] resulting in about 0.5 million protomers. Among these protomers, only in-clinical trials and FDA approved drugs (a total of 1283 protomers) were selected for docking. OpenBabel software[54] was used to minimize selected compounds. These compounds were docked into a preprocessed SARS-CoV-2 RBD protein pocket by

utilizing the AutoDock Vina.[55] For improving the reliability of docking, these compounds were also docked using the BindScope web application.[56] The xyz grid cell origin of –37.0 Å, 30.0 Å, and 3.5 Å with dimensions of 26.0, 45.5, and 22.0 in the x, y, and z directions, respectively, was built for docking calculations. The grid cell was constructed at key residues located within receptor binding motif of the RBD that are directly involved in interacting with the hACE2. The spike RBD–ligand binding affinities were ranked based on a consensus docking results from two scoring functions Vina[55] and 3D-convolutional neural networks method (Kdeep).[57] Consensus docking scores were chosen as the measure of protein–ligand binding affinities to rank the poses of the studied compounds. For the next high-throughput virtual screening, we selected the top 13 compounds that have a consensus docking score of ≤ -38 kJ mol^{-1} (-9 kcal mol^{-1}). Moreover, we selected one compound from each scoring functions Vina[55] and Kdeep algorithm[57] that has the highest protein–ligand binding affinity. All molecular docking results are provided in Table C.1 in Appendix C.

4.3.3 MD Simulations

All-atom MD simulations were done using the NAMD 2.13 package.[58] We performed MD simulations on the model systems with top docking results (total of 15 RBD–ligand complexes). Model systems of the RBD–ligand complexes were prepared in an explicit solvent using the TIP3P water model[59] in a simulation cell with dimensions of $86 \times 71 \times 96$ Å^3. All crystallographically resolved water molecules were removed from model systems. The parameters for the ligands and the spike RBD protein model structures were all set using the CHARMM general force field (CGenFF),[60] and the CHARMM36 force field,[61] respectively. Model systems were neutralized using chloride ions. The MD protocols involve minimization, annealing, equilibration, and production. The protein backbone atoms were restrained in the minimization and annealing simulations. The Cα atoms of the protein backbone were restrained in the 1 ns equilibration simulations. For the 100 ns MD production simulations, no atoms were restrained. The isothermal-isobaric (NPT) ensemble and a 2 fs time-step was chosen for all MD simulations. The pressure was set at 1 atm using the Nosé-Hoover Langevin piston barostat[62, 63] with the Langevin piston decay of 0.2 ps and a period of 0.4 ps. The temperature was set at 298.15 K using the Langevin thermostat[64] and a damping frequency of 1 ps^{-1}. A cutoff distance of 10.0 Å was

applied for Lennard-Jones interactions with a pair list distance of 12 Å, interactions were smoothly truncated at 8.0 Å. The particle-mesh Ewald (PME) method was utilized to treat the long-range electrostatic interactions,[65] where a grid spacing of 1.0 Å was used for all simulation cells. Covalent bonds involving hydrogen atoms were constrained using the SHAKE algorithm.[66]

4.3.4 Absolute Binding Energy Calculations

One of the main goal in computer-aided drug discovery is the accurate and reliable prediction of the absolute binding energy of receptor-ligand systems. Here, we calculated the absolute binding energies of the stable RBD–ligand complexes that resulted from the MD simulations. Starting from the equilibrated RBD–ligand structures, we conducted the absolute binding energy calculations using the potential of mean force (PMF) approach as described by Chipot and coworkers.[67, 68] It has been reported that the PMF approach accurately predicts protein–ligand binding affinities.[67, 69] A set of geometrical restraints on collective variables[70] are exploited to accurately determine the translational, rotational, and conformational entropies that accompany the binding process and, thus, computing protein–ligand absolute binding energies. These restraints include the root mean-square deviation (RMSD) of the ligand in the bound (site) and unbound (bulk) states compared to an equilibrated reference structure of the RBD–ligand complex. Additional restraints include three Euler (Θ, Φ, Ψ) and two spherical (θ, φ) angles that describe the relative orientation and position of the ligand with respect to the RBD protein, respectively, see Figure C.1 in the Appendix C. The equilibrium binding constant (K_{eq}) can be determined as,

$$K_{eq} = exp\left[-\beta\left(\Delta G_c^{site} + \Delta G_c^{bulk} + \Delta G_o^{site} + \Delta G_a^{site} + \Delta G_o^{bulk} - \frac{1}{\beta}\ln\left(S^* I^* C^\circ\right)\right)\right] \tag{4.1}$$

where the ΔG_c^{site} and ΔG_c^{bulk} denote the Gibbs energy changes of the conformational ligand RMSD in the site and bulk states, respectively, the ΔG_o^{site} and ΔG_a^{site} represent the Gibbs energy changes associated with the orientational and the positional of the ligand in the binding site, respectively, and the ΔG_o^{bulk} represents the Gibbs energy change associated with the ligand orientation in the bulk. The last term in Eq. (4.1) represents the separation of the ligand from the binding site into the bulk. It should be mentioned that the ΔG_o^{bulk} is calculated analytically as reported by Chipot and

coworkers.[67] More details on theoretical background of the binding energy calculations using the PMF route can be obtained elsewhere.[67] Eventually, the standard binding energy is

$$\Delta G^{\circ}_{bind} = k_B T \ln K_{eq} C^{\circ} \tag{4.2}$$

where the k_B and T are the Boltzmann constant and simulation temperature, respectively, and $C^{\circ} = 1/1661$ Å^3 is the standard one molar concentration. For each model system, the RBD–ligand separation, RMSD (site), RMSD (bulk), and angular course variables were run for 50 ns, 50 ns, 100 ns, and 50 ns, respectively. By leveraging GPU-accelerated NAMD engine,[71] the simulations were performed in triplicate, yielding an aggregate total of 750 ns simulation time for each model system. Absolute binding energies reported in this study are the averages of the triplicate runs.

4.3.5 Steered Molecular Dynamics (SMD) Simulations

To probe the selectivity and the potency of the top hits binding to the spike RBD protein, SMD simulations of the RBD–ligand–hACE2 model systems were conducted. The RBD–ligand–hACE2 model systems were solvated using a TIP3P water model with a 12 Å buffer around the system and then extended 30.0 Å in the SMD pulling axis, resulting in a simulation cell with dimensions of 121 × 121 × 167 Å^3. The SMD simulations were employed by harmonically restraining the position of the spike RBD protein center-of-mass, and moving the second restraint center-of-mass of the hACE2 protein, with a constant pulling speed of 1.5 Å ns^{-1} in the z-axis direction.

4.4 Results and Discussion

We performed an integrated computational strategy including molecular docking, MD simulations, absolute binding energy calculations, and SMD simulations to accelerate the identification of promising drug candidates for COVID-19. 1283 compounds (in-clinical trials and FDA approved drugs) were retrieved from the ZINC15 database[53] and advanced to flexible molecular docking using both Kdeep[57] and AutoDock Vina[55] scoring functions. Consensus docking scores were chosen as an initial measure of the RBD–ligand binding affinities to rank the poses of the screened compounds. Docking results of the top 15 compounds are listed in Table 4.1. Docking results of all

Table 4.1: Summary of top consensus docking results in kJ mol^{-1} for SARS-CoV-2 spike RBD target

Compound ID	Vina score	Kdeep score	Consensus score
ZINC6717782	-38	-40	-39
ZINC95628821	-36	-41	-39
ZINC253638647	-35	-43	-38
ZINC3979524	-36	-41	-38
ZINC253387884	-35	-41	-38
ZINC255977094	-36	-40	-38
ZINC150339052	-37	-39	-38
ZINC261494659	-35	-41	-38
ZINC936069565	-34	-42	-38
ZINC51951669	-37	-38	-38
ZINC49637509	-32	-43	-38
ZINC261494658	-33	-42	-38
ZINC95617623	-32	-43	-38
ZINC261494590[a]	-25	-47	-36
ZINC3978005[b]	-40	-23	-32

[a] The compound was selected based on the Kdeep scoring function; [b] The compound was selected based on the Vina scoring function.

screened compounds are provided in Table C.1 in Appendix C. The two-dimensional structures and the three-dimensional docked conformations of these compounds are also provided (see Figures C.2–C.5 in Appendix C).

The best 15 RBD–ligand complexes from molecular docking were used as starting structures for the conventional MD simulations. Ensemble MD simulations consolidate the effect of solvation, flexibility of both ligand and protein target, and better estimate of protein-ligand nonbonded interactions. The structure stability of the RBD-ligand model systems were evaluated by the RMSD with respect to the equilibrated structures (see Figures C.6 and C.7 in Appendix C). The time-evolution of the RMSD show that most ligands with invalid binding modes reveal significant signs of binding instability in the RBD binding pocket. Snapshots of the last frame of the stable simulated RBD–ligand model systems are depicted in Figure 4.1.

The use of absolute binding energy calculations is crucial to enhance the hit identification. Consequently, rigorous absolute binding energy calculations were only conducted on the stable RBD-ligand systems resulting from the MD simulations. In

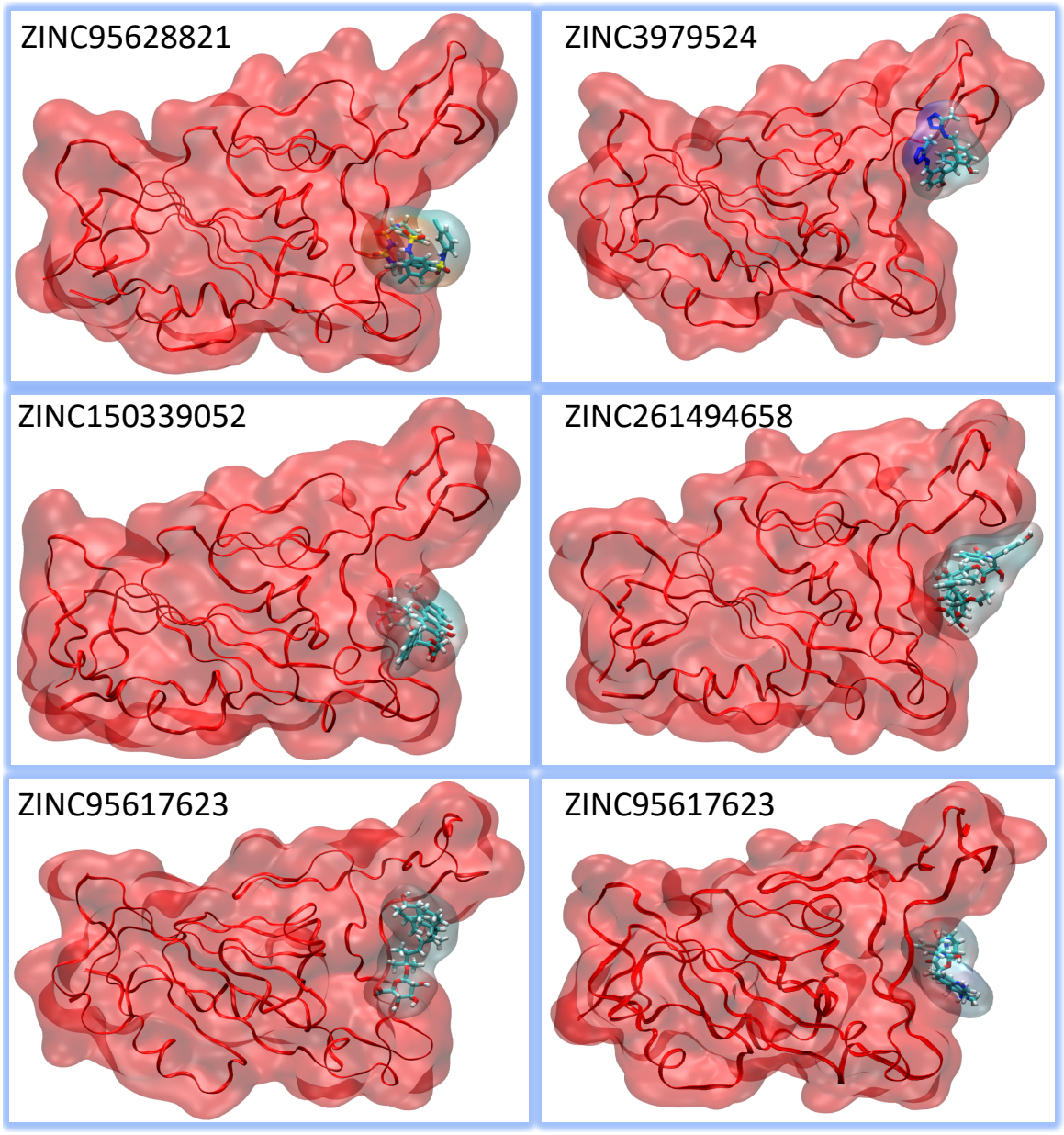

Figure 4.1: The last frame of the 100 ns MD simulations of ligands complexed with the spike RBD protein. ligands are shown as sticks and the RBD is shown as red ribbons.

Table 4.2: The calculated contributions accompanying the RBD–ligand binding process and the predicted ΔG°_{bind} in kJ mol^{-1}

Protein-ligand complex	ΔG^{site}_{c}	$\Delta G^{site}_{angular}$	$-\frac{1}{\beta}\ln(S^{*}I^{*}C^{\circ})$	ΔG^{bulk}_{c}	ΔG°_{bind}
RBD–ZINC95628821	-73 ± 6	-5 ± 0	-44 ± 6	72 ± 3	-23 ± 3
RBD–ZINC3979524	-22 ± 4	-5 ± 0	-38 ± 2	22 ± 2	-12 ± 3
RBD–ZINC150339052	-41 ± 5	-9 ± 3	-12 ± 3	38 ± 3	$+3 \pm 2$
RBD–ZINC261494658	-33 ± 2	-7 ± 0	-24 ± 3	29 ± 1	-8 ± 2
RBD–ZINC95617623	-38 ± 4	-9 ± 1	-26 ± 4	27 ± 1	-19 ± 1
RBD–ZINC3978005	-21 ± 5	-9 ± 1	-12 ± 1	19 ± 3	$+4 \pm 4$

absolute binding energy calculations, the resulting contributions from the aforementioned restraints are computed sequentially using the extended adaptive biasing force (eABF) method[72] with the unbiased corrected z-averaged restraint (CZAR) estimator[73] implemented in the Colvars module[70] of NAMD. The contributions from the course variables and the final standard binding energy (ΔG°_{bind}) of ligands to the SARS-CoV-2 spike RBD protein are provided in Table 4.2.

Unambiguously, the four ligands, namely, ZINC95628821, ZINC95617623, ZINC-3979524, and ZINC261494658 bind spontaneously to the SARS-CoV-2 spike RBD with ΔG°_{bind} of $-23, -19, -12$, and -8, respectively. In contrast, the two ligands, namely, ZINC150339052 and ZINC3978005 have non-spontaneous binding behavior toward the RBD with $\Delta G^{\circ}_{bind} = 3$ and 4 kJ mol^{-1}, respectively. These values represent the non-covalent interaction energies between the ligands and the spike RBD and give a good estimate of their binding affinities.

To validate the potency of the RBD–ligand binding affinities, we need to investigate if the top hits are able to interfere with the RBD–hACE2 binding event. For this purpose, SMD simulations were employed for distinguishing active from decoy ligands. Both strong and weak ligands listed in Table 4.2 were considered for SMD simulations as a validation strategy. In SMD simulations, the center of mass of the RBD was kept fixed (i.e., PHE400 of the RBD is an anchoring residue), whereas the center of mass of the hACE2 was steered (i.e., TYR515 of the hACE2 is a pulling residue). Figure 4.2 shows the final results of 20 ns SMD simulations for the RBD–hACE2 in the presence and absence of ligands.

The initial and the equilibrated conformations of RBD–ligand–hACE2 model systems are also provided (see Figure C.8 in Appendix C). The time-evolution force

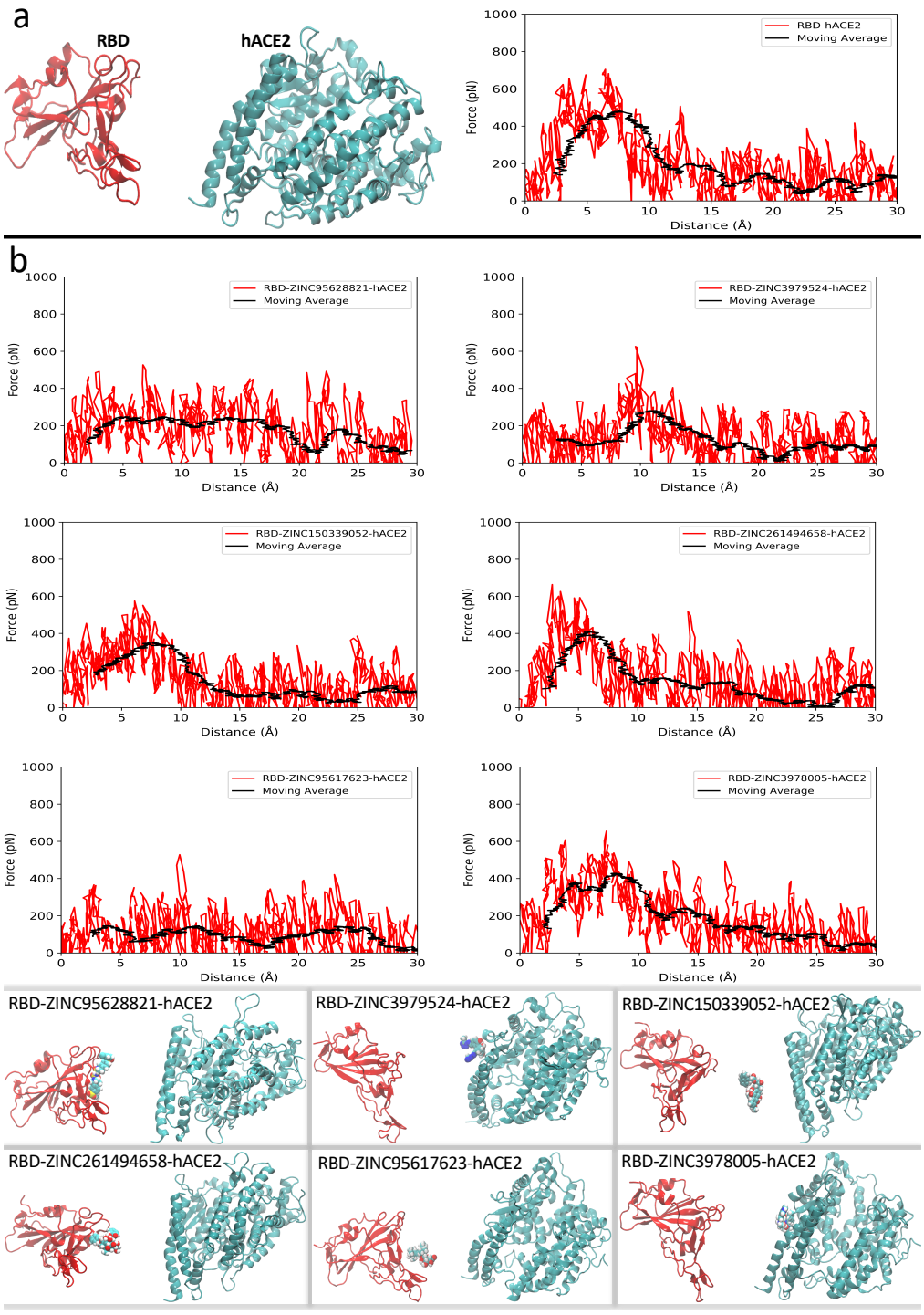

Figure 4.2: (a) The structure of the apo RBD–hACE2 (left) along with its time-averaged SMD results (right); (b) the structures of the RBD–ligand–hACE2 (bottom) along with their time-averaged SMD results (top). All structures were depicted after the 20 ns SMD simulations. The RBD, the hACE2, and the ligands are shown as red cartoon, cyan cartoon, spheres, respectively.

profile of the unbinding event of the RBD–ACE2 model system has a maximum rupture force of 704 pN, in a good agreement with the computed maximum rupture force of 751 pN reported recently.[74] Taka et al also reported the unbinding process of SARS-CoV-2 spike RBD from the hACE2 by carrying out SMD simulations.[75] It is well established that the rupture force is directly proportional with the receptor-ligand binding affinity.[76] The moving average (black line) of the time-evolution force profiles in Figure 4.2 indicates that ligands (particularly ZINC95628821, ZINC3979524, and ZINC95617623) are disrupting the RBD-hACE2 binding by lowering the rupture force. Additionally, the structures in Figure 4.2b show that ligands, namely, ZINC95628821, ZINC261494658, and ZINC95617623 are strong binders to the RBD protein. This is anticipated due to the fact that these ligands have relatively better binding affinity to the RBD than other ligands, namely, ZINC150339052, and ZINC3978005. On the contrary, during the SMD simulations, ZINC3979524 and ZINC3978005 left the RBD and attached to the hACE2 receptor, revealing that these ligands have more favourable interactions to the hACE2 than the RBD. SMD simulations also revealed that ZINC150339052 has non promising binding affinity toward neither the RBD nor the hACE2 proteins (see Figure 4.2b). Detailed analyses of the ligand interaction diagram of the equilibrated RBD–ligand–hACE2 complexes are shown in Figure 4.3.

Ligands that exhibit robust RBD binding stability during the SMD simulations, namely, ZINC95628821, ZINC261494658, and ZINC95617623, indeed form more non-covalent interactions (i.e. hydrogen bonding, pi-cation, pi-pi stacking) with key amino acid residues of the RBD and enjoy more exposure to the RBD binding pose than other ligands. Notably, these robust binders have direct polar contact with ARG403 of the RBD. Moreover, these ligands also interfere with key residues of the hACE2 protein (i.e. ASP38, TYR41, and LYS353). Interestingly, ARG403 of the RBD and residues ASP38, TYR41, and LYS353 of the hACE2 were reported as true hot spots that contribute to the stability of the RBD–hACE2 interface.[77] Many studies reported that hydrophobic interactions also play a critical role in anchoring the RBD to the hACE2 receptor.[75, 78] All ligands that possess spontaneous standard binding energies have at least four direct contacts with the RBD hydrophobic residues (see Figure 4.3). The polar and non-polar interactions of the RBD-ligand complexes contribute to their total standard binding energy. Based on rigorous binding energy calculations and SMD simulations, we suggest that the top drug candidates are ZINC95628821 followed by ZINC95617623, ZINC3979524, and ZINC261494658. These top hits certify critical

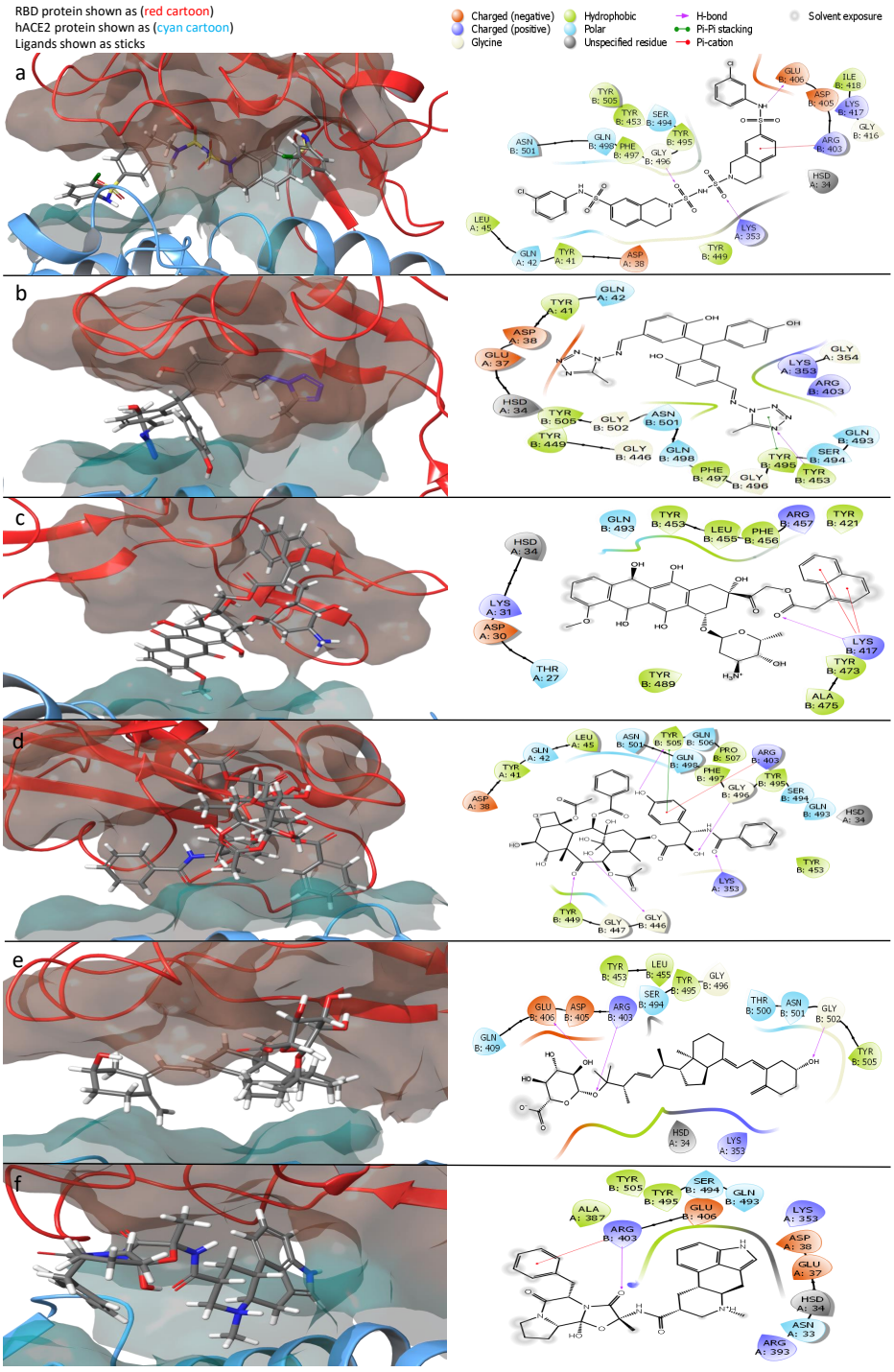

Figure 4.3: Representative poses (left) detailed ligand interaction diagrams (right) of the RBD–ligand–ACE2 complexes. (a) ZINC95628821, (b) ZINC3979524, (c) ZINC150339052, (d) ZINC261494658, (e) ZINC95617623, (f) ZINC3978005. In the ligand interaction diagram, the hACE2 and the RBD residues were labeled A and B, respectively.

interactions associated with the RBD-ligand-hACE2 binding, which in turn disrupt the RBD-hACE2 binding event.

4.5 Conclusions

In this work, we performed high-throughput virtual screening that comprise of molecular docking, MD simulations, non-covalent absolute binding energy calculations, and SMD simulations for the discovery of SARS-CoV-2 spike RBD-based inhibitors. Vina[55] and Kdeep[57] scoring functions were leveraged for structure-based screening and ranking of in-clinical trials and FDA approved drugs. Absolute binding energy calculations in combinations with the SMD simulations provided more effective ranking procedures of the top hits. Based on integrated *in silico* approach, our findings suggest that ZINC95628821, ZINC95617623, ZINC3979524, and ZINC261494658 have potential antiviral effects by blocking the RBD–hACE2 recognition. Clinical trials have shown that ZINC3979524 is a novel inhibitor of a respiratory syncytial virus with the EC50 of 1.4 nM, and thus, this compound along with the other drug candidates suggested herein need to be considered for further *in vitro* and *in vivo* investigation. This study provides a rational drug design of RBD-based inhibitors for accelerating the research and development of effective COVID-19 medications.

References

(1) *COVID-19 weekly epidemiological update*; tech. rep.; 23 February 2021.

(2) Wang, Y.; Zhang, D.; Du, G.; Du, R.; Zhao, J.; Jin, Y.; Fu, S.; Gao, L.; Cheng, Z.; Lu, Q., et al. *The Lancet* **2020**, *395*, 1569–1578.

(3) Young, B.; Tan, T. T.; Leo, Y. S. *The Lancet. Infectious Diseases* **2021**, *21*, 20.

(4) Hossain, M. G.; Akter, S.; Saha, S. *Journal of Microbiology, Immunology and Infection* **2020**, *54*, 175–181.

(5) Wang, Q.; Zhang, Y.; Wu, L.; Niu, S.; Song, C.; Zhang, Z.; Lu, G.; Qiao, C.; Hu, Y.; Yuen, K.-Y., et al. *Cell* **2020**, *181*, 894–904.

(6) Ye, Q.; West, A. M.; Silletti, S.; Corbett, K. D. *Protein Science* **2020**, *29*, 1890–1901.

(7) Siu, Y.; Teoh, K.; Lo, J.; Chan, C.; Kien, F.; Escriou, N.; Tsao, S.; Nicholls, J.; Altmeyer, R.; Peiris, J., et al. *Journal of virology* **2008**, *82*, 11318–11330.

(8) Mittal, A.; Manjunath, K.; Ranjan, R. K.; Kaushik, S.; Kumar, S.; Verma, V. *PLoS pathogens* **2020**, *16*, e1008762.

(9) Haque, S. M.; Ashwaq, O.; Sarief, A.; Azad John Mohamed, A. K. *Future virology* **2020**, *15*, 625–648.

(10) Izda, V.; Jeffries, M. A.; Sawalha, A. H. *Clinical Immunology* **2020**, 108634.

(11) Liu, X.-H.; Zhang, X.; Lu, Z.-H.; Zhu, Y. S.; Wang, T. *Biomedicine & Pharmacotherapy* **2020**, 111035.

(12) Mulholland, A. J.; Amaro, R. E. **2020**, *60*, 5724–5726.

(13) Li, Z.; Li, X.; Huang, Y.-Y.; Wu, Y.; Liu, R.; Zhou, L.; Lin, Y.; Wu, D.; Zhang, L.; Liu, H., et al. *Proceedings of the National Academy of Sciences* **2020**, *117*, 27381–27387.

(14) Abu-Saleh, A. A.-A. A.; Awad, I. E.; Yadav, A.; Poirier, R. A. *Physical Chemistry Chemical Physics* **2020**, *22*, 23099–23106.

(15) Awoonor-Williams, E.; Abu-Saleh, A. A.-A. A. *Physical Chemistry Chemical Physics* **2021**, *23*, 6746–6757.

(16) Zhang, H.; Yang, Y.; Li, J.; Wang, M.; Saravanan, K. M.; Wei, J.; Tze-Yang Ng, J.; Tofazzal Hossain, M.; Liu, M.; Zhang, H., et al. *PLoS computational biology* **2020**, *16*, e1008489.

(17) Wrapp, D.; Wang, N.; Corbett, K. S.; Goldsmith, J. A.; Hsieh, C.-L.; Abiona, O.; Graham, B. S.; McLellan, J. S. *Science* **2020**, *367*, 1260–1263.

(18) Walls, A. C.; Park, Y.-J.; Tortorici, M. A.; Wall, A.; McGuire, A. T.; Veesler, D. *Cell* **2020**, *181*, 281–292.

(19) Casalino, L.; Gaieb, Z.; Goldsmith, J. A.; Hjorth, C. K.; Dommer, A. C.; Harbison, A. M.; Fogarty, C. A.; Barros, E. P.; Taylor, B. C.; McLellan, J. S., et al. *ACS Central Science* **2020**, *6*, 1722–1734.

(20) Choi, Y. K.; Cao, Y.; Frank, M.; Woo, H.; Park, S.-J.; Yeom, M. S.; Croll, T. I.; Seok, C.; Im, W. *Journal of Chemical Theory and Computation* **2021**, *17*, 2479–2487.

(21) Shang, J.; Wan, Y.; Luo, C.; Ye, G.; Geng, Q.; Auerbach, A.; Li, F. *Proceedings of the National Academy of Sciences* **2020**, *117*, 11727–11734.

(22) Tang, T.; Jaimes, J. A.; Bidon, M. K.; Straus, M. R.; Daniel, S.; Whittaker, G. R. *ACS Infectious Diseases* **2021**, *7*, 264–272.

(23) Gur, M.; Taka, E.; Yilmaz, S. Z.; Kilinc, C.; Aktas, U.; Golcuk, M. *The Journal of Chemical Physics* **2020**, *153*, 075101.

(24) Letko, M.; Marzi, A.; Munster, V. *Nature microbiology* **2020**, *5*, 562–569.

(25) Borkotoky, S.; Dey, D.; Banerjee, M. *Journal of Chemical Information and Modeling* **2021**, *61*, 423–431.

(26) Ou, X.; Liu, Y.; Lei, X.; Li, P.; Mi, D.; Ren, L.; Guo, L.; Guo, R.; Chen, T.; Hu, J., et al. *Nature communications* **2020**, *11*, 1–12.

(27) Shang, J.; Ye, G.; Shi, K.; Wan, Y.; Luo, C.; Aihara, H.; Geng, Q.; Auerbach, A.; Li, F. *Nature* **2020**, *581*, 221–224.

(28) Peng, C.; Zhu, Z.; Shi, Y.; Wang, X.; Mu, K.; Yang, Y.; Zhang, X.; Xu, Z.; Zhu, W. *The journal of physical chemistry letters* **2020**, *11*, 10482–10488.

(29) Piccoli, L.; Park, Y.-J.; Tortorici, M. A.; Czudnochowski, N.; Walls, A. C.; Beltramello, M.; Silacci-Fregni, C.; Pinto, D.; Rosen, L. E.; Bowen, J. E., et al. *Cell* **2020**, *183*, 1024–1042.

(30) Huo, J.; Zhao, Y.; Ren, J.; Zhou, D.; Duyvesteyn, H. M.; Ginn, H. M.; Carrique, L.; Malinauskas, T.; Ruza, R. R.; Shah, P. N., et al. *Cell host & microbe* **2020**, *28*, 445–454.

(31) Wu, N. C.; Yuan, M.; Liu, H.; Lee, C.-C. D.; Zhu, X.; Bangaru, S.; Torres, J. L.; Caniels, T. G.; Brouwer, P. J.; Van Gils, M. J., et al. *Cell reports* **2020**, *33*, 108274.

(32) Linsky, T. W.; Vergara, R.; Codina, N.; Nelson, J. W.; Walker, M. J.; Su, W.; Barnes, C. O.; Hsiang, T.-Y.; Esser-Nobis, K.; Yu, K., et al. *Science* **2020**, *370*, 1208–1214.

(33) Cao, L.; Goreshnik, I.; Coventry, B.; Case, J. B.; Miller, L.; Kozodoy, L.; Chen, R. E.; Carter, L.; Walls, A. C.; Park, Y.-J., et al. *Science* **2020**, *370*, 426–431.

(34) Schütz, D.; Ruiz-Blanco, Y. B.; Münch, J.; Kirchhoff, F.; Sanchez-Garcia, E.; Müller, J. A. *Advanced drug delivery reviews* **2020**, *167*, 47–65.

(35) Pomplun, S.; Jbara, M.; Quartararo, A. J.; Zhang, G.; Brown, J. S.; Lee, Y.-C.; Ye, X.; Hanna, S.; Pentelute, B. L. *ACS Central Science* **2021**, *7*, 156–163.

(36) Wang, G.; Yang, M.-L.; Duan, Z.-L.; Liu, F.-L.; Jin, L.; Long, C.-B.; Zhang, M.; Tang, X.-P.; Xu, L.; Li, Y.-C., et al. *Cell research* **2021**, *31*, 17–24.

(37) Chowdhury, S. M.; Talukder, S. A.; Khan, A. M.; Afrin, N.; Ali, M. A.; Islam, R.; Parves, R.; Al Mamun, A.; Sufian, M. A.; Hossain, M. N., et al. *The Journal of Physical Chemistry B* **2020**, *124*, 9785–9792.

(38) Sitthiyotha, T.; Chunsrivirot, S. *The Journal of Physical Chemistry B* **2020**, *124*, 10930–10942.

(39) Han, Y.; Král, P. *ACS nano* **2020**, *14*, 5143–5147.

(40) Freitas, F. C.; Ferreira, P. H. B.; Favaro, D. C.; Oliveira, R. J. d. *Journal of chemical information and modeling* **2021**, *61*, 1226–1243.

(41) Maas, M. N.; Hintzen, J. C.; Löffler, P. M.; Mecinović, J. *Chemical Communications* **2021**, *57*, 3283–3286.

(42) Trezza, A.; Iovinelli, D.; Santucci, A.; Prischi, F.; Spiga, O. *Scientific reports* **2020**, *10*, 1–8.

(43) Deganutti, G.; Prischi, F.; Reynolds, C. A. *Journal of computer-aided molecular design* **2021**, *35*, 195–207.

(44) Awad, I. E.; Abu-Saleh, A. A.-A. A.; Sharma, S.; Yadav, A.; Poirier, R. A. *Journal of Biomolecular Structure and Dynamics* **2020**, 1–14.

(45) Wang, X.; Cao, R.; Zhang, H.; Liu, J.; Xu, M.; Hu, H.; Li, Y.; Zhao, L.; Li, W.; Sun, X., et al. *Cell discovery* **2020**, *6*, 1–5.

(46) Puhl, A. C. et al. *ACS Omega* **2021**, *6*, 7454–7468.

(47) Pandey, P.; Rane, J. S.; Chatterjee, A.; Kumar, A.; Khan, R.; Prakash, A.; Ray, S. *Journal of Biomolecular Structure and Dynamics* **2020**, 1–11.

(48) Toelzer, C.; Gupta, K.; Yadav, S. K.; Borucu, U.; Davidson, A. D.; Williamson, M. K.; Shoemark, D. K.; Garzoni, F.; Staufer, O.; Milligan, R., et al. *Science* **2020**, *370*, 725–730.

(49) Li, Y.-T.; Yang, C.; Wu, Y.; Lv, J.-J.; Feng, X.; Tian, X.; Zhou, Z.; Pan, X.; Liu, S.; Tian, L.-W. *Journal of Natural Products* **2021**, *84*, 436–443.

(50) Gangadevi, S.; Badavath, V. N.; Thakur, A.; Yin, N.; De Jonghe, S.; Acevedo, O.; Jochmans, D.; Leyssen, P.; Wang, K.; Neyts, J., et al. *The journal of physical chemistry letters* **2021**, *12*, 1793–1802.

(51) Williams-Noonan, B. J.; Todorova, N.; Kulkarni, K.; Aguilar, M.-I.; Yarovsky, I. *The Journal of Physical Chemistry B* **2021**.

(52) Anandakrishnan, R.; Aguilar, B.; Onufriev, A. V. *Nucleic acids research* **2012**, *40*, W537–W541.

(53) Sterling, T.; Irwin, J. J. *Journal of chemical information and modeling* **2015**, *55*, 2324–2337.

(54) O'Boyle, N. M.; Banck, M.; James, C. A.; Morley, C.; Vandermeersch, T.; Hutchison, G. R. *Journal of cheminformatics* **2011**, *3*, 33.

(55) Vina, A. *J. Comput. Chem* **2010**, *31*, 455–461.

(56) Skalic, M.; Martınez-Rosell, G.; Jiménez, J.; De Fabritiis, G. *Bioinformatics* **2019**, *35*, 1237–1238.

(57) Jiménez, J.; Skalic, M.; Martinez-Rosell, G.; De Fabritiis, G. *Journal of chemical information and modeling* **2018**, *58*, 287–296.

(58) Phillips, J. C.; Braun, R.; Wang, W.; Gumbart, J.; Tajkhorshid, E.; Villa, E.; Chipot, C.; Skeel, R. D.; Kale, L.; Schulten, K. *Journal of computational chemistry* **2005**, *26*, 1781–1802.

(59) Jorgensen, W. L.; Chandrasekhar, J.; Madura, J. D.; Impey, R. W.; Klein, M. L. *The Journal of chemical physics* **1983**, *79*, 926–935.

(60) Yu, W.; He, X.; Vanommeslaeghe, K.; MacKerell Jr, A. D. *Journal of computational chemistry* **2012**, *33*, 2451–2468.

(61) Best, R. B.; Zhu, X.; Shim, J.; Lopes, P. E.; Mittal, J.; Feig, M.; MacKerell Jr, A. D. *Journal of chemical theory and computation* **2012**, *8*, 3257–3273.

(62) Nosé, S.; Klein, M. *Molecular Physics* **1983**, *50*, 1055–1076.

(63) Nosé, S. *Molecular physics* **1984**, *52*, 255–268.

(64) Grest, G. S.; Kremer, K. *Physical Review A* **1986**, *33*, 3628.

(65) Essmann, U.; Perera, L.; Berkowitz, M. L.; Darden, T.; Lee, H.; Pedersen, L. G. *The Journal of chemical physics* **1995**, *103*, 8577–8593.

(66) Ryckaert, J.-P.; Ciccotti, G.; Berendsen, H. J. *Journal of computational physics* **1977**, *23*, 327–341.

(67) Fu, H.; Cai, W.; Hénin, J.; Roux, B.; Chipot, C. *Journal of Chemical Theory and Computation* **2017**, *13*, 5173–5178.

(68) Fu, H.; Gumbart, J. C.; Chen, H.; Shao, X.; Cai, W.; Chipot, C. *Journal of chemical information and modeling* **2018**, *58*, 556–560.

(69) Gumbart, J. C.; Roux, B.; Chipot, C. *Journal of chemical theory and computation* **2013**, *9*, 794–802.

(70) Fiorin, G.; Klein, M. L.; Hénin, J. *Molecular Physics* **2013**, *111*, 3345–3362.

(71) Phillips, J. C.; Hardy, D. J.; Maia, J. D.; Stone, J. E.; Ribeiro, J. V.; Bernardi, R. C.; Buch, R.; Fiorin, G.; Hénin, J.; Jiang, W., et al. *The Journal of chemical physics* **2020**, *153*, 044130.

(72) Fu, H.; Shao, X.; Chipot, C.; Cai, W. *Journal of chemical theory and computation* **2016**, *12*, 3506–3513.

(73) Lesage, A.; Lelievre, T.; Stoltz, G.; Hénin, J. *The Journal of Physical Chemistry B* **2017**, *121*, 3676–3685.

(74) Nguyen, H. L.; Lan, P. D.; Thai, N. Q.; Nissley, D. A.; O'Brien, E. P.; Li, M. S. *The Journal of Physical Chemistry B* **2020**, *124*, 7336–7347.

(75) Taka, E.; Yilmaz, S. Z.; Golcuk, M.; Kilinc, C.; Aktas, U.; Yildiz, A.; Gur, M. *bioRxiv* **2020**.

(76) Vuong, Q. V.; Nguyen, T. T.; Li, M. S. *Journal of chemical information and modeling* **2015**, *55*, 2731–2738.

(77) Laurini, E.; Marson, D.; Aulic, S.; Fermeglia, M.; Pricl, S. *ACS nano* **2020**, *14*, 11821–11830.

(78) Wang, Y.; Liu, M.; Gao, J. *Proceedings of the National Academy of Sciences* **2020**, *117*, 13967–13974.

"Life is like riding a bicycle. To keep your balance, you must keep moving"

—Albert Einstein

5

Summary and Outlook

Computer modeling and simulations play a pivotal role in chemistry and biophysics. By leveraging supercomputers, theoretical chemists can explain in detail the atomic resolution of biological systems and solve chemical problems.

The accelerated emergence of resistant bacteria is becoming a serious global threat. Aminoglycoside antibiotics comprise a large number of compounds used for bacterial infections. However, the resistance mechanisms of bacteria (e.g. enzymatic modifications) affect the activity of these antibiotics, which in turn inhibit the efficacy of the drug. In chapter one, a general introduction about aminoglycoside modifying enzymes has been presented. In chapter two, I focused on the phosphorylation mechanism of the aminoglycoside antibiotic, namely, kanamycin A, that is catalysed by the aminoglycoside modifying enzyme. In this chapter I performed combined MD simulations and ONIOM(QM:QM) calculations to understand the catalytic mechanism of the phosphorylation reaction and to provide insight for the rational design of mechanism-based inhibitors of the bacterial phosphotransferase modifying enzyme.

Computational studies of the other bacterial enzymatic modifications (i.e., aminoglycoside acetyltransferases aminoglycoside nucleotidyltransferases) need to be completed in future work.

COVID-19 that is caused by the SARS-CoV-2 virus has an acutely high dissemination potential, which resulted in a global pandemic. At the time of writing my thesis, there is no effective drug available to treat the disease. Therefore, developing an effective antiviral drug is an urgent need. SARS-CoV-2 has many druggable promising targets such as the spike protein, the main protease, the papian-like protease, and the RNA-dependent RNA-polymerase. In this thesis, I focused on the viral spike and the main protease.

In chapter three, I carried out a high-throughput virtual screening for the discovery of potent inhibitors against the viral main protease. I conducted ligand-based and structure-based molecular screening, MD simulations, and binding energy calculations. The results suggest several promising inhibitors (approved and bioactive compounds) for the viral main protease. The suggested top hit compounds will pave the way for the lead optimization and design of the viral main protease inhibitors.

In chapter four, by leveraging ZINC15 database, I screened compounds in the "beyond rule of 5" chemical space (MW $>$ 500, and LogP $\leq$ 5) for the discovery of potent binders toward SARS-CoV-2 spike RBD protein. I performed a comprehensive *in silico* protocol comprising non-covalent molecular docking, MD simulations, absolute binding energy calculations, and SMD simulations. The top hits, namely, ZINC95628821, ZINC95617623, ZINC3979524, and ZINC261494658 interfere with binding events of the viral RBD and the hACE2 protein of the host cell. Therefore, these suggested drugs need to be tested by *in vitro* and *in vivo* studies. It should be pointed out that remdesivir is the only U.S. FDA approved drug for COVID-19 patients requiring hospitalization. However, it has been reported that it failed to show clinical benefits for moderately severe COVID-19 patients.[1, 2] Therefore, the full free energy landscape of the remdesiver binding to its viral target (i.e. RNA-dependent RNA-polymerase) will be studied in future work to provide insight for the intelligent design of more potent inhibitors.

References

(1) Wang, Y.; Zhang, D.; Du, G.; Du, R.; Zhao, J.; Jin, Y.; Fu, S.; Gao, L.; Cheng, Z.; Lu, Q., et al. *The Lancet* **2020**, *395*, 1569–1578.

(2) Young, B.; Tan, T. T.; Leo, Y. S. *The Lancet. Infectious Diseases* **2021**, *21*, 20.

A

Phosphorylation of the Antibiotic Kanamycin

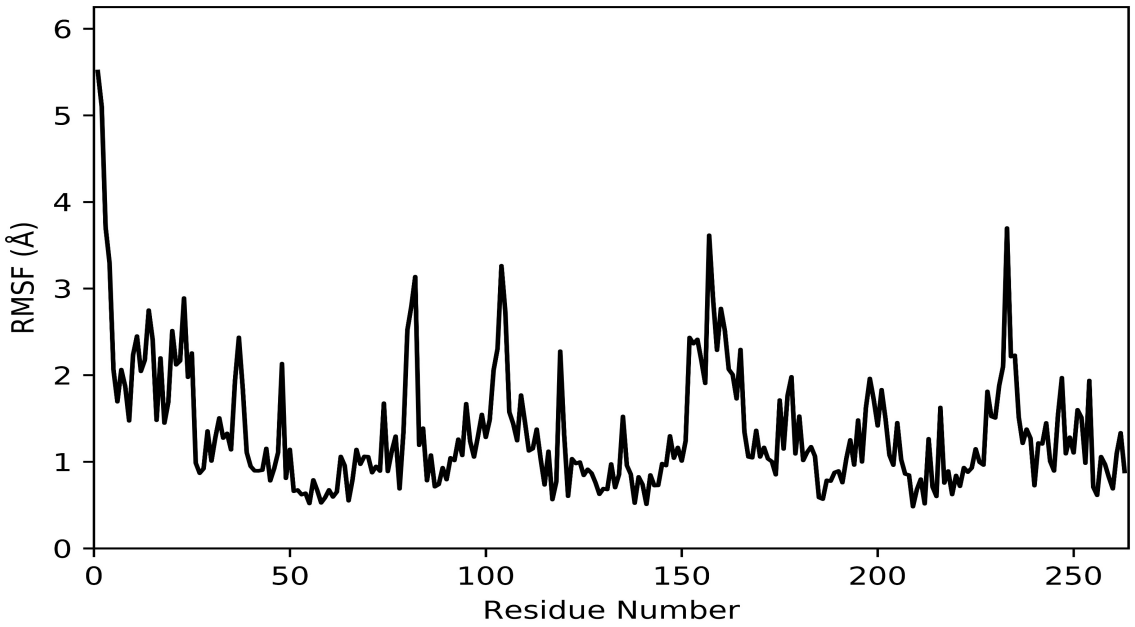

Figure A.1: RMSF analysis of APH(3′)-IIIa protein in complex with the ATP, Mg^{2+} ions, and kanamycin A during 100 ns MD simulation.

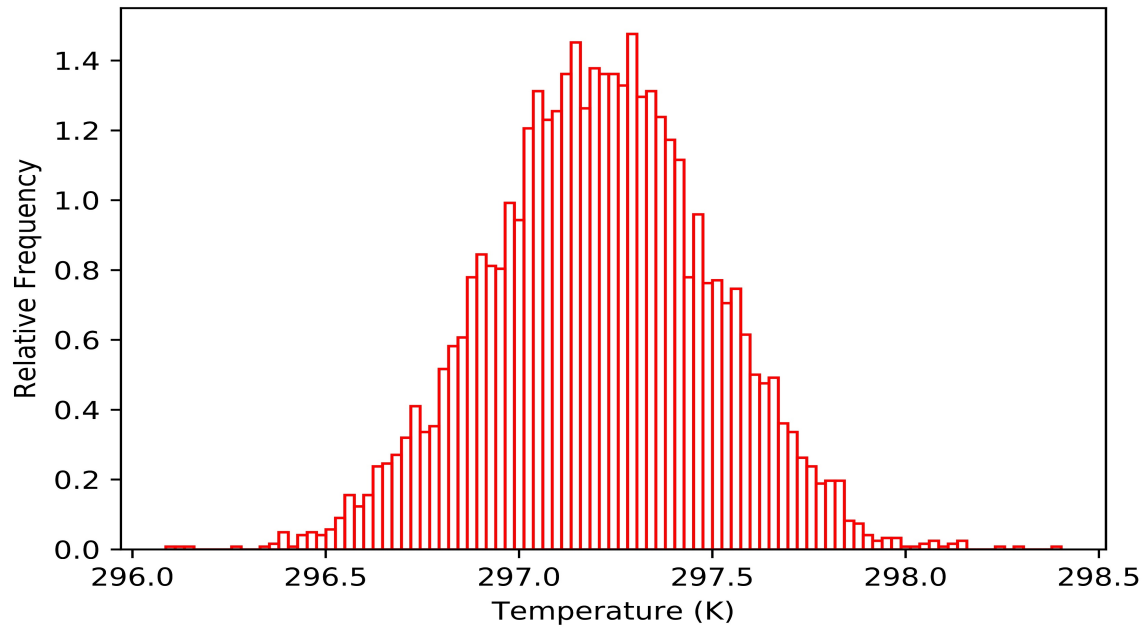

Figure A.2: Temperature distribution of the APH(3′)-IIIa enzyme model as a function of time during 100 ns MD production.

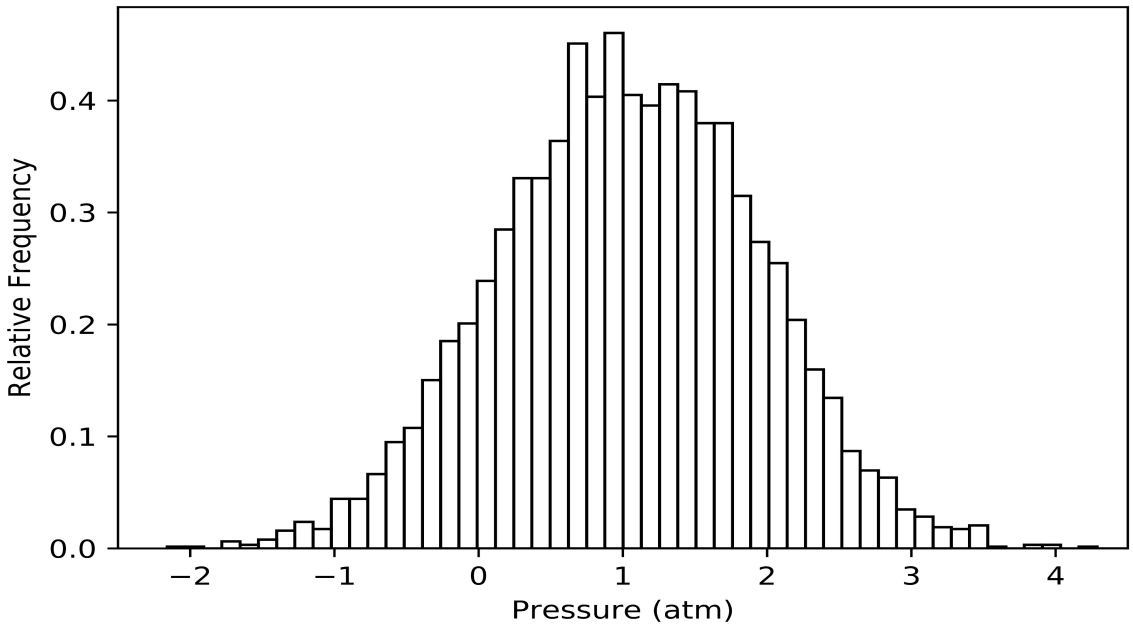

Figure A.3: Pressure distribution of the APH(3′)-IIIa enzyme model as a function of time during 100 ns MD production.

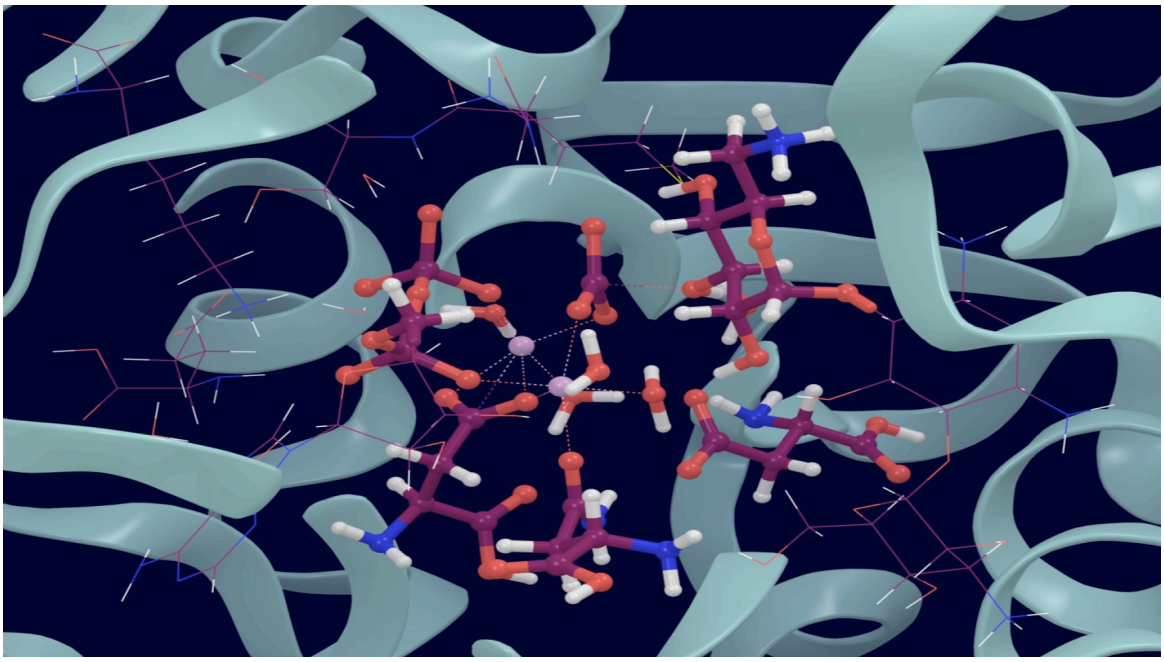

Figure A.4: The metaphosphate is constrained between two nucleophiles (3′-hydroxyl group of kanamycin, and the β-phosphate oxygen of the ADP).

B

Discovery of Potent Inhibitors for SARS-CoV-2's Main Protease

Table B.1: Docking results of compounds in kcal mol^{-1} for SARS-CoV-2 Mpro target

Ligand code	Docking score	Ligand code	Docking score	Ligand code	Docking score	Ligand code	Docking score
DB01200	-9.5	DB00559	-8.2	CHEMBL187239	-7.9	DB00320	-7.8
CHEMBL275592	-9.0	DB00696	-8.2	CHEMBL264866	-7.9	DB00549	-7.8
DB01200	-9.0	DB01177	-8.2	CHEMBL267277	-7.9	DB00616	-7.8
DB01232	-9.0	DB08934	-8.2	CHEMBL288347	-7.9	DB00696	-7.8
DB00696	-8.9	CHEMBL116969	-8.1	CHEMBL288347	-7.9	DB01301	-7.8
DB01232	-8.9	CHEMBL1256086	-8.1	CHEMBL288347	-7.9	DB01601	-7.8
DB08995	-8.9	CHEMBL140704	-8.1	CHEMBL315380	-7.9	DB04570	-7.8
DB01232	-8.8	CHEMBL152817	-8.1	CHEMBL331645	-7.9	DB06813	-7.8
DB01232	-8.8	CHEMBL275592	-8.1	CHEMBL383674	-7.9	DB08827	-7.8
DB00549	-8.7	CHEMBL288347	-8.1	CHEMBL421410	-7.9	DB08934	-7.8
DB01232	-8.7	CHEMBL288347	-8.1	CHEMBL421410	-7.9	DB08995	-7.8
DB01232	-8.7	CHEMBL383674	-8.1	CHEMBL430743	-7.9	DB08995	-7.8
DB01232	-8.7	CHEMBL421410	-8.1	DB00220	-7.9	DB08995	-7.8
DB06290	-8.7	CHEMBL421410	-8.1	DB00471	-7.9	CHEMBL126085	-7.7
DB08995	-8.7	DB00220	-8.1	DB00528	-7.9	CHEMBL182854	-7.7
DB09297	-8.7	DB00224	-8.1	DB00549	-7.9	CHEMBL182854	-7.7
CHEMBL1256086	-8.6	DB00549	-8.1	DB00559	-7.9	CHEMBL187239	-7.7
CHEMBL140704	-8.6	DB00559	-8.1	DB00694	-7.9	CHEMBL206413	-7.7
CHEMBL275592	-8.6	DB00559	-8.1	DB00696	-7.9	CHEMBL2074811	-7.7
DB00320	-8.6	DB08827	-8.1	DB00696	-7.9	CHEMBL324630	-7.7
DB01232	-8.6	DB08934	-8.1	DB01200	-7.9	CHEMBL325241	-7.7
DB01232	-8.6	DB08995	-8.1	DB01220	-7.9	CHEMBL331645	-7.7
CHEMBL116969	-8.5	DB09235	-8.1	DB01251	-7.9	CHEMBL331645	-7.7
DB00471	-8.5	CHEMBL121923	-8.0	DB01329	-7.9	CHEMBL341234	-7.7
DB00471	-8.5	CHEMBL238114	-8.0	DB01419	-7.9	CHEMBL341234	-7.7
DB00549	-8.5	CHEMBL275592	-8.0	DB04845	-7.9	CHEMBL383674	-7.7
DB00549	-8.5	CHEMBL275592	-8.0	DB08934	-7.9	CHEMBL421410	-7.7
DB00694	-8.5	CHEMBL275592	-8.0	DB08995	-7.9	CHEMBL430743	-7.7
DB00696	-8.5	CHEMBL288347	-8.0	CHEMBL116969	-7.8	CHEMBL430743	-7.7
DB01200	-8.5	CHEMBL288347	-8.0	CHEMBL116969	-7.8	CHEMBL430743	-7.7
DB00471	-8.4	CHEMBL288347	-8.0	CHEMBL116969	-7.8	CHEMBL53355	-7.7
DB00471	-8.4	CHEMBL383674	-8.0	CHEMBL121923	-7.8	CHEMBL553189	-7.7
DB00549	-8.4	CHEMBL421410	-8.0	CHEMBL121923	-7.8	CHEMBL68229	-7.7
DB01177	-8.4	CHEMBL53355	-8.0	CHEMBL1256086	-7.8	DB00224	-7.7
DB01177	-8.4	DB00278	-8.0	CHEMBL1256086	-7.8	DB00278	-7.7
CHEMBL116969	-8.3	DB00293	-8.0	CHEMBL1256086	-7.8	DB00319	-7.7
CHEMBL2074811	-8.3	DB00471	-8.0	CHEMBL1256086	-7.8	DB00385	-7.7
CHEMBL275592	-8.3	DB00471	-8.0	CHEMBL140324	-7.8	DB00471	-7.7
CHEMBL288347	-8.3	DB00503	-8.0	CHEMBL140324	-7.8	DB00559	-7.7
CHEMBL421410	-8.3	DB00549	-8.0	CHEMBL2074811	-7.8	DB00559	-7.7
DB00224	-8.3	DB00559	-8.0	CHEMBL315380	-7.8	DB00694	-7.7
DB00320	-8.3	DB01061	-8.0	CHEMBL3344364	-7.8	DB00696	-7.7
DB00320	-8.3	DB01061	-8.0	CHEMBL341234	-7.8	DB00696	-7.7
DB00320	-8.3	DB01200	-8.0	CHEMBL383674	-7.8	DB01177	-7.7
DB00471	-8.3	DB01200	-8.0	CHEMBL421410	-7.8	DB01264	-7.7
DB00559	-8.3	DB01419	-8.0	CHEMBL430743	-7.8	DB01326	-7.7
DB00559	-8.3	DB01419	-8.0	CHEMBL509330	-7.8	DB01347	-7.7
DB08995	-8.3	DB01601	-8.0	CHEMBL53355	-7.8	DB01419	-7.7
CHEMBL275592	-8.2	DB06813	-8.0	CHEMBL53355	-7.8	DB01601	-7.7
CHEMBL275592	-8.2	DB08827	-8.0	CHEMBL68229	-7.8	DB01601	-7.7
CHEMBL455346	-8.2	DB08827	-8.0	DB00220	-7.8	DB06796	-7.7
CHEMBL509330	-8.2	DB08934	-8.0	DB00224	-7.8	DB06796	-7.7
DB00278	-8.2	DB08995	-8.0	DB00224	-7.8	DB06813	-7.7
DB00278	-8.2	DB09235	-8.0	DB00278	-7.8	DB08816	-7.7
DB00278	-8.2	DB09235	-8.0	DB00278	-7.8	DB08816	-7.7
DB00549	-8.2	DB09235	-8.0	DB00278	-7.8	DB08827	-7.7

Ligand code	Docking score	Ligand code	Docking score	Ligand code	Docking score	Ligand code	Docking score
DB08827	-7.7	DB01347	-7.6	CHEMBL68229	-7.5	CHEMBL152817	-7.4
DB09235	-7.7	DB01419	-7.6	CHEMBL71334	-7.5	CHEMBL157441	-7.4
DB09235	-7.7	DB01601	-7.6	CHEMBL71334	-7.5	CHEMBL2074811	-7.4
DB09235	-7.7	DB04570	-7.6	CHEMBL71334	-7.5	CHEMBL2074811	-7.4
DB09299	-7.7	DB06290	-7.6	DB00224	-7.5	CHEMBL238114	-7.4
DB09299	-7.7	DB06796	-7.6	DB00224	-7.5	CHEMBL291719	-7.4
CHEMBL121923	-7.6	DB06796	-7.6	DB00224	-7.5	CHEMBL291719	-7.4
CHEMBL121923	-7.6	DB06827	-7.6	DB00224	-7.5	CHEMBL315380	-7.4
CHEMBL121923	-7.6	DB08827	-7.6	DB00319	-7.5	CHEMBL322945	-7.4
CHEMBL1256086	-7.6	DB08934	-7.6	DB00320	-7.5	CHEMBL331645	-7.4
CHEMBL1256086	-7.6	DB08934	-7.6	DB00503	-7.5	CHEMBL341234	-7.4
CHEMBL13155	-7.6	DB09299	-7.6	DB00528	-7.5	CHEMBL344419	-7.4
CHEMBL13155	-7.6	CHEMBL1093632	-7.5	DB00616	-7.5	CHEMBL344419	-7.4
CHEMBL140324	-7.6	CHEMBL116969	-7.5	DB00616	-7.5	CHEMBL344419	-7.4
CHEMBL140324	-7.6	CHEMBL121923	-7.5	DB00694	-7.5	CHEMBL355777	-7.4
CHEMBL152817	-7.6	CHEMBL121923	-7.5	DB00696	-7.5	CHEMBL360805	-7.4
CHEMBL157441	-7.6	CHEMBL121923	-7.5	DB00864	-7.5	CHEMBL382977	-7.4
CHEMBL1790527	-7.6	CHEMBL1256086	-7.5	DB00932	-7.5	CHEMBL404655	-7.4
CHEMBL182854	-7.6	CHEMBL126085	-7.5	DB00948	-7.5	CHEMBL404655	-7.4
CHEMBL187239	-7.6	CHEMBL13155	-7.5	DB00948	-7.5	CHEMBL404655	-7.4
CHEMBL238114	-7.6	CHEMBL140324	-7.5	DB01061	-7.5	CHEMBL430743	-7.4
CHEMBL238114	-7.6	CHEMBL152817	-7.5	DB01200	-7.5	CHEMBL430743	-7.4
CHEMBL264866	-7.6	CHEMBL152817	-7.5	DB01251	-7.5	CHEMBL437115	-7.4
CHEMBL267277	-7.6	CHEMBL156038	-7.5	DB01251	-7.5	CHEMBL438612	-7.4
CHEMBL330783	-7.6	CHEMBL157441	-7.5	DB01301	-7.5	CHEMBL578278	-7.4
CHEMBL331645	-7.6	CHEMBL182854	-7.5	DB01326	-7.5	CHEMBL578758	-7.4
CHEMBL331645	-7.6	CHEMBL187239	-7.5	DB01347	-7.5	CHEMBL61309	-7.4
CHEMBL3344267	-7.6	CHEMBL187239	-7.5	DB01347	-7.5	CHEMBL68229	-7.4
CHEMBL341234	-7.6	CHEMBL2074811	-7.5	DB01601	-7.5	CHEMBL68229	-7.4
CHEMBL341234	-7.6	CHEMBL2074811	-7.5	DB01601	-7.5	CHEMBL68229	-7.4
CHEMBL383674	-7.6	CHEMBL238114	-7.5	DB01601	-7.5	CHEMBL71334	-7.4
CHEMBL383674	-7.6	CHEMBL315380	-7.5	DB04570	-7.5	CHEMBL71334	-7.4
CHEMBL404655	-7.6	CHEMBL315380	-7.5	DB04570	-7.5	CHEMBL71334	-7.4
CHEMBL421410	-7.6	CHEMBL315380	-7.5	DB04898	-7.5	DB00212	-7.4
CHEMBL438612	-7.6	CHEMBL315380	-7.5	DB06290	-7.5	DB00256	-7.4
CHEMBL445191	-7.6	CHEMBL324630	-7.5	DB06290	-7.5	DB00256	-7.4
CHEMBL445191	-7.6	CHEMBL324630	-7.5	DB06796	-7.5	DB00278	-7.4
CHEMBL66399	-7.6	CHEMBL325241	-7.5	DB06813	-7.5	DB00385	-7.4
CHEMBL68229	-7.6	CHEMBL325241	-7.5	DB06827	-7.5	DB00385	-7.4
CHEMBL68229	-7.6	CHEMBL331645	-7.5	DB08827	-7.5	DB00385	-7.4
CHEMBL71334	-7.6	CHEMBL341234	-7.5	DB08827	-7.5	DB00503	-7.4
DB00212	-7.6	CHEMBL344419	-7.5	DB08934	-7.5	DB00528	-7.4
DB00320	-7.6	CHEMBL344419	-7.5	DB08934	-7.5	DB00616	-7.4
DB00385	-7.6	CHEMBL383674	-7.5	DB09235	-7.5	DB00616	-7.4
DB00616	-7.6	CHEMBL383674	-7.5	DB09235	-7.5	DB00701	-7.4
DB00701	-7.6	CHEMBL404655	-7.5	DB09297	-7.5	DB00878	-7.4
DB00878	-7.6	CHEMBL430743	-7.5	CHEMBL1093632	-7.4	DB00878	-7.4
DB00932	-7.6	CHEMBL455346	-7.5	CHEMBL116483	-7.4	DB00932	-7.4
DB01200	-7.6	CHEMBL509330	-7.5	CHEMBL116969	-7.4	DB01061	-7.4
DB01251	-7.6	CHEMBL509330	-7.5	CHEMBL116969	-7.4	DB01177	-7.4
DB01264	-7.6	CHEMBL509330	-7.5	CHEMBL118557	-7.4	DB01200	-7.4
DB01264	-7.6	CHEMBL53355	-7.5	CHEMBL118557	-7.4	DB01251	-7.4
DB01326	-7.6	CHEMBL53355	-7.5	CHEMBL126085	-7.4	DB01264	-7.4
DB01326	-7.6	CHEMBL553189	-7.5	CHEMBL13155	-7.4	DB01264	-7.4
DB01326	-7.6	CHEMBL573443	-7.5	CHEMBL13155	-7.4	DB01301	-7.4
DB01347	-7.6	CHEMBL66399	-7.5	CHEMBL140324	-7.4	DB01301	-7.4

Ligand code	Docking score	Ligand code	Docking score	Ligand code	Docking score	Ligand code	Docking score
DB01329	-7.4	DB00212	-7.3	CHEMBL264866	-7.2	DB00701	-7.2
DB01347	-7.4	DB00212	-7.3	CHEMBL267277	-7.2	DB00701	-7.2
DB01419	-7.4	DB00212	-7.3	CHEMBL267277	-7.2	DB00864	-7.2
DB01601	-7.4	DB00303	-7.3	CHEMBL267277	-7.2	DB00932	-7.2
DB06796	-7.4	DB00303	-7.3	CHEMBL267277	-7.2	DB00948	-7.2
DB06796	-7.4	DB00319	-7.3	CHEMBL291719	-7.2	DB00948	-7.2
DB08816	-7.4	DB00320	-7.3	CHEMBL291719	-7.2	DB01061	-7.2
DB08889	-7.4	DB00385	-7.3	CHEMBL291719	-7.2	DB01061	-7.2
DB09299	-7.4	DB00503	-7.3	CHEMBL291719	-7.2	DB01061	-7.2
CHEMBL1093632	-7.3	DB00503	-7.3	CHEMBL320637	-7.2	DB01251	-7.2
CHEMBL116483	-7.3	DB00528	-7.3	CHEMBL322945	-7.2	DB01251	-7.2
CHEMBL13155	-7.3	DB00718	-7.3	CHEMBL325241	-7.2	DB01251	-7.2
CHEMBL140324	-7.3	DB00718	-7.3	CHEMBL330783	-7.2	DB01301	-7.2
CHEMBL140704	-7.3	DB00878	-7.3	CHEMBL330783	-7.2	DB01326	-7.2
CHEMBL152817	-7.3	DB00878	-7.3	CHEMBL330783	-7.2	DB01329	-7.2
CHEMBL156038	-7.3	DB00878	-7.3	CHEMBL330783	-7.2	DB01329	-7.2
CHEMBL157441	-7.3	DB00932	-7.3	CHEMBL3344267	-7.2	DB01419	-7.2
CHEMBL1790527	-7.3	DB00932	-7.3	CHEMBL341234	-7.2	DB04570	-7.2
CHEMBL1790527	-7.3	DB00948	-7.3	CHEMBL344419	-7.2	DB04865	-7.2
CHEMBL187239	-7.3	DB01061	-7.3	CHEMBL344419	-7.2	DB04898	-7.2
CHEMBL187239	-7.3	DB01229	-7.3	CHEMBL351766	-7.2	DB05521	-7.2
CHEMBL187239	-7.3	DB01264	-7.3	CHEMBL382977	-7.2	DB06290	-7.2
CHEMBL206413	-7.3	DB01264	-7.3	CHEMBL382977	-7.2	DB06813	-7.2
CHEMBL2074811	-7.3	DB01264	-7.3	CHEMBL404655	-7.2	DB09230	-7.2
CHEMBL264866	-7.3	DB01264	-7.3	CHEMBL437115	-7.2	DB09272	-7.2
CHEMBL264866	-7.3	DB01326	-7.3	CHEMBL438612	-7.2	DB09297	-7.2
CHEMBL291719	-7.3	DB01329	-7.3	CHEMBL438612	-7.2	DB09297	-7.2
CHEMBL291719	-7.3	DB04570	-7.3	CHEMBL438612	-7.2	DB09297	-7.2
CHEMBL291719	-7.3	DB04570	-7.3	CHEMBL445191	-7.2	DB09297	-7.2
CHEMBL315380	-7.3	DB06796	-7.3	CHEMBL446278	-7.2	DB09299	-7.2
CHEMBL315380	-7.3	DB06796	-7.3	CHEMBL455346	-7.2	DB09299	-7.2
CHEMBL319844	-7.3	DB06813	-7.3	CHEMBL455346	-7.2	CHEMBL116483	-7.1
CHEMBL320637	-7.3	DB08906	-7.3	CHEMBL455346	-7.2	CHEMBL126085	-7.1
CHEMBL320637	-7.3	DB09063	-7.3	CHEMBL509330	-7.2	CHEMBL13155	-7.1
CHEMBL324630	-7.3	DB09063	-7.3	CHEMBL53355	-7.2	CHEMBL140324	-7.1
CHEMBL324630	-7.3	DB09230	-7.3	CHEMBL553189	-7.2	CHEMBL140324	-7.1
CHEMBL325241	-7.3	DB09297	-7.3	CHEMBL57492	-7.2	CHEMBL156038	-7.1
CHEMBL330783	-7.3	CHEMBL116483	-7.2	CHEMBL57492	-7.2	CHEMBL156038	-7.1
CHEMBL330783	-7.3	CHEMBL118557	-7.2	CHEMBL578278	-7.2	CHEMBL156038	-7.1
CHEMBL331645	-7.3	CHEMBL118557	-7.2	CHEMBL61309	-7.2	CHEMBL156038	-7.1
CHEMBL331645	-7.3	CHEMBL13155	-7.2	CHEMBL61309	-7.2	CHEMBL157441	-7.1
CHEMBL341234	-7.3	CHEMBL13155	-7.2	CHEMBL8969	-7.2	CHEMBL1790066	-7.1
CHEMBL344419	-7.3	CHEMBL152817	-7.2	DB00206	-7.2	CHEMBL1790527	-7.1
CHEMBL344419	-7.3	CHEMBL156038	-7.2	DB00212	-7.2	CHEMBL1790527	-7.1
CHEMBL430743	-7.3	CHEMBL156038	-7.2	DB00212	-7.2	CHEMBL182854	-7.1
CHEMBL445191	-7.3	CHEMBL156038	-7.2	DB00220	-7.2	CHEMBL206413	-7.1
CHEMBL455346	-7.3	CHEMBL157441	-7.2	DB00303	-7.2	CHEMBL319844	-7.1
CHEMBL509330	-7.3	CHEMBL157441	-7.2	DB00319	-7.2	CHEMBL319844	-7.1
CHEMBL53355	-7.3	CHEMBL157441	-7.2	DB00320	-7.2	CHEMBL322945	-7.1
CHEMBL553189	-7.3	CHEMBL157441	-7.2	DB00503	-7.2	CHEMBL322945	-7.1
CHEMBL553189	-7.3	CHEMBL187239	-7.2	DB00503	-7.2	CHEMBL322945	-7.1
CHEMBL578278	-7.3	CHEMBL206413	-7.2	DB00503	-7.2	CHEMBL324630	-7.1
CHEMBL61309	-7.3	CHEMBL206413	-7.2	DB00503	-7.2	CHEMBL325241	-7.1
CHEMBL68229	-7.3	CHEMBL2074811	-7.2	DB00528	-7.2	CHEMBL325241	-7.1
CHEMBL71334	-7.3	CHEMBL238114	-7.2	DB00616	-7.2	CHEMBL330783	-7.1
CHEMBL71334	-7.3	CHEMBL264866	-7.2	DB00694	-7.2	CHEMBL335456	-7.1

Ligand code	Docking score	Ligand code	Docking score	Ligand code	Docking score	Ligand code	Docking score
CHEMBL3361310	-7.1	DB01301	-7.1	CHEMBL455346	-7.0	DB09230	-7.0
CHEMBL360805	-7.1	DB01326	-7.1	CHEMBL455346	-7.0	DB09272	-7.0
CHEMBL382977	-7.1	DB01329	-7.1	CHEMBL507767	-7.0	DB09272	-7.0
CHEMBL382977	-7.1	DB01347	-7.1	CHEMBL507767	-7.0	DB09297	-7.0
CHEMBL404655	-7.1	DB01419	-7.1	CHEMBL507767	-7.0	DB09299	-7.0
CHEMBL404655	-7.1	DB01419	-7.1	CHEMBL509330	-7.0	DB09299	-7.0
CHEMBL404655	-7.1	DB05521	-7.1	CHEMBL553189	-7.0	CHEMBL116483	-6.9
CHEMBL434033	-7.1	DB05521	-7.1	CHEMBL569788	-7.0	CHEMBL116483	-6.9
CHEMBL437115	-7.1	DB06290	-7.1	CHEMBL569788	-7.0	CHEMBL118557	-6.9
CHEMBL438612	-7.1	DB06813	-7.1	CHEMBL569788	-7.0	CHEMBL118557	-6.9
CHEMBL438612	-7.1	DB06813	-7.1	CHEMBL573443	-7.0	CHEMBL126085	-6.9
CHEMBL445191	-7.1	DB08816	-7.1	CHEMBL57492	-7.0	CHEMBL152817	-6.9
CHEMBL446278	-7.1	DB08889	-7.1	CHEMBL578124	-7.0	CHEMBL1790066	-6.9
CHEMBL446278	-7.1	DB09065	-7.1	CHEMBL578278	-7.0	CHEMBL1790066	-6.9
CHEMBL446278	-7.1	DB09065	-7.1	CHEMBL61309	-7.0	CHEMBL1790527	-6.9
CHEMBL509330	-7.1	DB09065	-7.1	CHEMBL61309	-7.0	CHEMBL182854	-6.9
CHEMBL53355	-7.1	DB09230	-7.1	CHEMBL8969	-7.0	CHEMBL238114	-6.9
CHEMBL553189	-7.1	DB09230	-7.1	DB00206	-7.0	CHEMBL264866	-6.9
CHEMBL553189	-7.1	DB09272	-7.1	DB00220	-7.0	CHEMBL264866	-6.9
CHEMBL553189	-7.1	DB09297	-7.1	DB00303	-7.0	CHEMBL264866	-6.9
CHEMBL573443	-7.1	DB09299	-7.1	DB00309	-7.0	CHEMBL306947	-6.9
CHEMBL573443	-7.1	CHEMBL1093632	-7.0	DB00319	-7.0	CHEMBL320637	-6.9
CHEMBL573443	-7.1	CHEMBL126085	-7.0	DB00319	-7.0	CHEMBL322945	-6.9
CHEMBL573443	-7.1	CHEMBL126085	-7.0	DB00385	-7.0	CHEMBL322945	-6.9
CHEMBL573443	-7.1	CHEMBL126085	-7.0	DB00385	-7.0	CHEMBL322945	-6.9
CHEMBL573443	-7.1	CHEMBL129334	-7.0	DB00492	-7.0	CHEMBL324630	-6.9
CHEMBL57492	-7.1	CHEMBL140704	-7.0	DB00528	-7.0	CHEMBL324630	-6.9
CHEMBL66399	-7.1	CHEMBL152817	-7.0	DB00616	-7.0	CHEMBL3344267	-6.9
CHEMBL66399	-7.1	CHEMBL1790066	-7.0	DB00616	-7.0	CHEMBL3357964	-6.9
CHEMBL66399	-7.1	CHEMBL1790527	-7.0	DB00694	-7.0	CHEMBL3361310	-6.9
CHEMBL8969	-7.1	CHEMBL182854	-7.0	DB00701	-7.0	CHEMBL351766	-6.9
CHEMBL8969	-7.1	CHEMBL182854	-7.0	DB00864	-7.0	CHEMBL351766	-6.9
DB00183	-7.1	CHEMBL206413	-7.0	DB00878	-7.0	CHEMBL351766	-6.9
DB00206	-7.1	CHEMBL206413	-7.0	DB00878	-7.0	CHEMBL360805	-6.9
DB00212	-7.1	CHEMBL267277	-7.0	DB00895	-7.0	CHEMBL379771	-6.9
DB00212	-7.1	CHEMBL267277	-7.0	DB00932	-7.0	CHEMBL379771	-6.9
DB00220	-7.1	CHEMBL267277	-7.0	DB00948	-7.0	CHEMBL379771	-6.9
DB00293	-7.1	CHEMBL306947	-7.0	DB00948	-7.0	CHEMBL382977	-6.9
DB00293	-7.1	CHEMBL319844	-7.0	DB01089	-7.0	CHEMBL426711	-6.9
DB00385	-7.1	CHEMBL320637	-7.0	DB01089	-7.0	CHEMBL434033	-6.9
DB00460	-7.1	CHEMBL320637	-7.0	DB01177	-7.0	CHEMBL437115	-6.9
DB00492	-7.1	CHEMBL320637	-7.0	DB01180	-7.0	CHEMBL437115	-6.9
DB00492	-7.1	CHEMBL322945	-7.0	DB01229	-7.0	CHEMBL438612	-6.9
DB00528	-7.1	CHEMBL324630	-7.0	DB01326	-7.0	CHEMBL442013	-6.9
DB00694	-7.1	CHEMBL325241	-7.0	DB01329	-7.0	CHEMBL442013	-6.9
DB00701	-7.1	CHEMBL325241	-7.0	DB01329	-7.0	CHEMBL442013	-6.9
DB00701	-7.1	CHEMBL330783	-7.0	DB04570	-7.0	CHEMBL445191	-6.9
DB00718	-7.1	CHEMBL3344364	-7.0	DB04845	-7.0	CHEMBL446278	-6.9
DB00718	-7.1	CHEMBL3344364	-7.0	DB04865	-7.0	CHEMBL446278	-6.9
DB00878	-7.1	CHEMBL335456	-7.0	DB04898	-7.0	CHEMBL446278	-6.9
DB00932	-7.1	CHEMBL3361310	-7.0	DB04898	-7.0	CHEMBL446278	-6.9
DB00932	-7.1	CHEMBL351766	-7.0	DB05521	-7.0	CHEMBL446278	-6.9
DB01061	-7.1	CHEMBL351766	-7.0	DB05521	-7.0	CHEMBL507767	-6.9
DB01089	-7.1	CHEMBL382977	-7.0	DB08873	-7.0	CHEMBL507767	-6.9
DB01177	-7.1	CHEMBL442013	-7.0	DB08889	-7.0	CHEMBL507767	-6.9
DB01251	-7.1	CHEMBL455346	-7.0	DB09063	-7.0	CHEMBL554395	-6.9

Ligand code	Docking score	Ligand code	Docking score	Ligand code	Docking score	Ligand code	Docking score
CHEMBL569788	-6.9	CHEMBL116483	-6.8	CHEMBL578758	-6.8	DB09063	-6.8
CHEMBL569788	-6.9	CHEMBL116483	-6.8	CHEMBL578758	-6.8	DB09063	-6.8
CHEMBL573443	-6.9	CHEMBL118557	-6.8	CHEMBL578758	-6.8	DB09063	-6.8
CHEMBL57492	-6.9	CHEMBL118557	-6.8	CHEMBL61309	-6.8	DB09065	-6.8
CHEMBL57492	-6.9	CHEMBL126085	-6.8	CHEMBL61309	-6.8	DB09065	-6.8
CHEMBL57492	-6.9	CHEMBL140704	-6.8	CHEMBL66399	-6.8	DB09065	-6.8
CHEMBL57492	-6.9	CHEMBL140704	-6.8	CHEMBL66399	-6.8	DB09065	-6.8
CHEMBL578278	-6.9	CHEMBL140704	-6.8	CHEMBL66399	-6.8	DB09230	-6.8
CHEMBL578278	-6.9	CHEMBL1790064	-6.8	CHEMBL66399	-6.8	DB09230	-6.8
CHEMBL78459	-6.9	CHEMBL1790066	-6.8	CHEMBL8969	-6.8	DB09272	-6.8
CHEMBL85651	-6.9	CHEMBL1790066	-6.8	CHEMBL8969	-6.8	CHEMBL1093982	-6.7
CHEMBL8969	-6.9	CHEMBL1790527	-6.8	CHEMBL8969	-6.8	CHEMBL1093982	-6.7
DB00206	-6.9	CHEMBL206413	-6.8	DB00183	-6.8	CHEMBL118557	-6.7
DB00206	-6.9	CHEMBL206413	-6.8	DB00206	-6.8	CHEMBL140704	-6.7
DB00220	-6.9	CHEMBL238114	-6.8	DB00206	-6.8	CHEMBL140704	-6.7
DB00293	-6.9	CHEMBL238114	-6.8	DB00256	-6.8	CHEMBL1790066	-6.7
DB00303	-6.9	CHEMBL306947	-6.8	DB00293	-6.8	CHEMBL1790066	-6.7
DB00319	-6.9	CHEMBL306947	-6.8	DB00319	-6.8	CHEMBL1790066	-6.7
DB00410	-6.9	CHEMBL306947	-6.8	DB00460	-6.8	CHEMBL1790527	-6.7
DB00460	-6.9	CHEMBL309507	-6.8	DB00528	-6.8	CHEMBL182854	-6.7
DB00492	-6.9	CHEMBL309507	-6.8	DB00718	-6.8	CHEMBL2112937	-6.7
DB00528	-6.9	CHEMBL309507	-6.8	DB00718	-6.8	CHEMBL30521	-6.7
DB00694	-6.9	CHEMBL319844	-6.8	DB00718	-6.8	CHEMBL309507	-6.7
DB00694	-6.9	CHEMBL319844	-6.8	DB00864	-6.8	CHEMBL309507	-6.7
DB00701	-6.9	CHEMBL320637	-6.8	DB00895	-6.8	CHEMBL319844	-6.7
DB00701	-6.9	CHEMBL320637	-6.8	DB00895	-6.8	CHEMBL319844	-6.7
DB00718	-6.9	CHEMBL330596	-6.8	DB00947	-6.8	CHEMBL3344267	-6.7
DB00718	-6.9	CHEMBL3344364	-6.8	DB01089	-6.8	CHEMBL3344364	-6.7
DB00895	-6.9	CHEMBL3344364	-6.8	DB01089	-6.8	CHEMBL3357964	-6.7
DB00976	-6.9	CHEMBL3361310	-6.8	DB01118	-6.8	CHEMBL360805	-6.7
DB01089	-6.9	CHEMBL351766	-6.8	DB01177	-6.8	CHEMBL360805	-6.7
DB01089	-6.9	CHEMBL351766	-6.8	DB01177	-6.8	CHEMBL379771	-6.7
DB01089	-6.9	CHEMBL351766	-6.8	DB01220	-6.8	CHEMBL379771	-6.7
DB01089	-6.9	CHEMBL355777	-6.8	DB01248	-6.8	CHEMBL382203	-6.7
DB01180	-6.9	CHEMBL379771	-6.8	DB01301	-6.8	CHEMBL382203	-6.7
DB01319	-6.9	CHEMBL379771	-6.8	DB01301	-6.8	CHEMBL426711	-6.7
DB01319	-6.9	CHEMBL382977	-6.8	DB01319	-6.8	CHEMBL426711	-6.7
DB01347	-6.9	CHEMBL382977	-6.8	DB01319	-6.8	CHEMBL442013	-6.7
DB01347	-6.9	CHEMBL404813	-6.8	DB01329	-6.8	CHEMBL507767	-6.7
DB04570	-6.9	CHEMBL426711	-6.8	DB01764	-6.8	CHEMBL554395	-6.7
DB04865	-6.9	CHEMBL426711	-6.8	DB04865	-6.8	CHEMBL554395	-6.7
DB05521	-6.9	CHEMBL426711	-6.8	DB04865	-6.8	CHEMBL569788	-6.7
DB05521	-6.9	CHEMBL437115	-6.8	DB04865	-6.8	CHEMBL578343	-6.7
DB05521	-6.9	CHEMBL437115	-6.8	DB04898	-6.8	CHEMBL578758	-6.7
DB06813	-6.9	CHEMBL437115	-6.8	DB04898	-6.8	CHEMBL578758	-6.7
DB06827	-6.9	CHEMBL437115	-6.8	DB05521	-6.8	CHEMBL61309	-6.7
DB06827	-6.9	CHEMBL438612	-6.8	DB06290	-6.8	CHEMBL85651	-6.7
DB08816	-6.9	CHEMBL445191	-6.8	DB08816	-6.8	CHEMBL8969	-6.7
DB08889	-6.9	CHEMBL507767	-6.8	DB08816	-6.8	DB00183	-6.7
DB08889	-6.9	CHEMBL507767	-6.8	DB08873	-6.8	DB00183	-6.7
DB09065	-6.9	CHEMBL554395	-6.8	DB08889	-6.8	DB00220	-6.7
DB09065	-6.9	CHEMBL554395	-6.8	DB08889	-6.8	DB00220	-6.7
DB09230	-6.9	CHEMBL57492	-6.8	DB08889	-6.8	DB00293	-6.7
DB09230	-6.9	CHEMBL578278	-6.8	DB08889	-6.8	DB00293	-6.7
DB09272	-6.9	CHEMBL578278	-6.8	DB08906	-6.8	DB00303	-6.7
CHEMBL116483	-6.8	CHEMBL578278	-6.8	DB09063	-6.8	DB00303	-6.7

Ligand code	Docking score	Ligand code	Docking score	Ligand code	Docking score	Ligand code	Docking score
DB00319	-6.7	CHEMBL355777	-6.6	CHEMBL1790064	-6.5	DB01319	-6.5
DB00460	-6.7	CHEMBL360805	-6.6	CHEMBL1790064	-6.5	DB01764	-6.5
DB00492	-6.7	CHEMBL360805	-6.6	CHEMBL2112937	-6.5	DB04845	-6.5
DB00948	-6.7	CHEMBL360805	-6.6	CHEMBL2112937	-6.5	DB08873	-6.5
DB01072	-6.7	CHEMBL360805	-6.6	CHEMBL309507	-6.5	DB08873	-6.5
DB01072	-6.7	CHEMBL379771	-6.6	CHEMBL309507	-6.5	DB08906	-6.5
DB01118	-6.7	CHEMBL426711	-6.6	CHEMBL3344267	-6.5	DB09026	-6.5
DB01180	-6.7	CHEMBL442013	-6.6	CHEMBL335456	-6.5	DB09026	-6.5
DB01248	-6.7	CHEMBL442013	-6.6	CHEMBL335456	-6.5	CHEMBL129334	-6.4
DB01248	-6.7	CHEMBL442013	-6.6	CHEMBL335456	-6.5	CHEMBL2112937	-6.4
DB01319	-6.7	CHEMBL445191	-6.6	CHEMBL335456	-6.5	CHEMBL2112937	-6.4
DB01319	-6.7	CHEMBL554395	-6.6	CHEMBL3361310	-6.5	CHEMBL30521	-6.4
DB01602	-6.7	CHEMBL554395	-6.6	CHEMBL340774	-6.5	CHEMBL30521	-6.4
DB01602	-6.7	CHEMBL574931	-6.6	CHEMBL340774	-6.5	CHEMBL330596	-6.4
DB01602	-6.7	CHEMBL578124	-6.6	CHEMBL355777	-6.5	CHEMBL330596	-6.4
DB01764	-6.7	CHEMBL578343	-6.6	CHEMBL355777	-6.5	CHEMBL3357964	-6.4
DB04865	-6.7	CHEMBL578758	-6.6	CHEMBL355777	-6.5	CHEMBL3361310	-6.4
DB04865	-6.7	CHEMBL578758	-6.6	CHEMBL379771	-6.5	CHEMBL3361310	-6.4
DB04865	-6.7	CHEMBL578758	-6.6	CHEMBL404031	-6.5	CHEMBL340774	-6.4
DB04898	-6.7	CHEMBL85651	-6.6	CHEMBL404031	-6.5	CHEMBL382203	-6.4
DB04898	-6.7	CHEMBL85651	-6.6	CHEMBL404813	-6.5	CHEMBL382203	-6.4
DB04898	-6.7	DB00206	-6.6	CHEMBL426711	-6.5	CHEMBL404031	-6.4
DB05109	-6.7	DB00256	-6.6	CHEMBL426711	-6.5	CHEMBL404031	-6.4
DB06290	-6.7	DB00293	-6.6	CHEMBL434033	-6.5	CHEMBL404813	-6.4
DB08816	-6.7	DB00303	-6.6	CHEMBL442013	-6.5	CHEMBL404813	-6.4
DB08873	-6.7	DB00361	-6.6	CHEMBL554395	-6.5	CHEMBL445191	-6.4
DB08873	-6.7	DB00410	-6.6	CHEMBL554395	-6.5	CHEMBL54110	-6.4
DB08906	-6.7	DB00460	-6.6	CHEMBL569788	-6.5	CHEMBL569788	-6.4
DB09272	-6.7	DB00492	-6.6	CHEMBL569788	-6.5	CHEMBL578343	-6.4
CHEMBL1093632	-6.6	DB00492	-6.6	CHEMBL574931	-6.5	CHEMBL78459	-6.4
CHEMBL1093982	-6.6	DB00615	-6.6	CHEMBL578343	-6.5	CHEMBL78459	-6.4
CHEMBL1093982	-6.6	DB00947	-6.6	CHEMBL67944	-6.5	CHEMBL78459	-6.4
CHEMBL1790064	-6.6	DB01072	-6.6	CHEMBL67944	-6.5	CHEMBL78459	-6.4
CHEMBL1790064	-6.6	DB01180	-6.6	CHEMBL78459	-6.5	CHEMBL85651	-6.4
CHEMBL2112937	-6.6	DB01180	-6.6	CHEMBL85651	-6.5	CHEMBL85651	-6.4
CHEMBL2112937	-6.6	DB01180	-6.6	CHEMBL85651	-6.5	DB00183	-6.4
CHEMBL30521	-6.6	DB01229	-6.6	DB00183	-6.5	DB00256	-6.4
CHEMBL306947	-6.6	DB01229	-6.6	DB00183	-6.5	DB00256	-6.4
CHEMBL306947	-6.6	DB01229	-6.6	DB00183	-6.5	DB00410	-6.4
CHEMBL306947	-6.6	DB01248	-6.6	DB00183	-6.5	DB00460	-6.4
CHEMBL306947	-6.6	DB01248	-6.6	DB00206	-6.5	DB00460	-6.4
CHEMBL309507	-6.6	DB01301	-6.6	DB00256	-6.5	DB00460	-6.4
CHEMBL309507	-6.6	DB01319	-6.6	DB00256	-6.5	DB00492	-6.4
CHEMBL319844	-6.6	DB01602	-6.6	DB00293	-6.5	DB00895	-6.4
CHEMBL3344267	-6.6	DB01602	-6.6	DB00303	-6.5	DB00895	-6.4
CHEMBL3344267	-6.6	DB04845	-6.6	DB00309	-6.5	DB00895	-6.4
CHEMBL3344267	-6.6	DB06290	-6.6	DB00492	-6.5	DB00948	-6.4
CHEMBL3344267	-6.6	DB08816	-6.6	DB00895	-6.5	DB00976	-6.4
CHEMBL3344364	-6.6	DB08873	-6.6	DB00895	-6.5	DB01072	-6.4
CHEMBL3344364	-6.6	DB09026	-6.6	DB00976	-6.5	DB01072	-6.4
CHEMBL3344364	-6.6	DB09026	-6.6	DB01072	-6.5	DB01072	-6.4
CHEMBL335456	-6.6	DB09063	-6.6	DB01072	-6.5	DB01220	-6.4
CHEMBL3357964	-6.6	DB09272	-6.6	DB01072	-6.5	DB01220	-6.4
CHEMBL3357964	-6.6	DB09272	-6.6	DB01180	-6.5	DB01248	-6.4
CHEMBL3361310	-6.6	CHEMBL129334	-6.5	DB01180	-6.5	DB01248	-6.4
CHEMBL3361310	-6.6	CHEMBL1790064	-6.5	DB01180	-6.5	DB01319	-6.4

Ligand code	Docking score	Ligand code	Docking score	Ligand code	Docking score	Ligand code	Docking score
DB04845	-6.4	DB06439	-6.3	DB01045	-6.2	CHEMBL67944	-6.1
DB06772	-6.4	DB06439	-6.3	DB01076	-6.2	CHEMBL67944	-6.1
DB08884	-6.4	DB06772	-6.3	DB01076	-6.2	DB00361	-6.1
DB08906	-6.4	DB08873	-6.3	DB01229	-6.2	DB00410	-6.1
DB09026	-6.4	DB08906	-6.3	DB01248	-6.2	DB00615	-6.1
DB09026	-6.4	DB09026	-6.3	DB01248	-6.2	DB00743	-6.1
DB09063	-6.4	DB09026	-6.3	DB01602	-6.2	DB00743	-6.1
CHEMBL1093632	-6.3	CHEMBL1093632	-6.2	DB01602	-6.2	DB00746	-6.1
CHEMBL1093632	-6.3	CHEMBL1093632	-6.2	DB01602	-6.2	DB00746	-6.1
CHEMBL1093982	-6.3	CHEMBL1093982	-6.2	DB04845	-6.2	DB00864	-6.1
CHEMBL129334	-6.3	CHEMBL1093982	-6.2	DB06439	-6.2	DB00947	-6.1
CHEMBL129334	-6.3	CHEMBL1093982	-6.2	DB06827	-6.2	DB00947	-6.1
CHEMBL1790064	-6.3	CHEMBL2112937	-6.2	DB08873	-6.2	DB00976	-6.1
CHEMBL1790064	-6.3	CHEMBL287202	-6.2	DB08884	-6.2	DB00976	-6.1
CHEMBL1790064	-6.3	CHEMBL287202	-6.2	DB08884	-6.2	DB01076	-6.1
CHEMBL2112937	-6.3	CHEMBL287202	-6.2	DB08884	-6.2	DB01118	-6.1
CHEMBL287202	-6.3	CHEMBL30521	-6.2	DB08906	-6.2	DB04855	-6.1
CHEMBL30521	-6.3	CHEMBL30521	-6.2	DB08906	-6.2	DB05109	-6.1
CHEMBL320685	-6.3	CHEMBL30521	-6.2	DB09026	-6.2	DB05109	-6.1
CHEMBL330596	-6.3	CHEMBL30521	-6.2	DB09296	-6.2	DB06439	-6.1
CHEMBL331808	-6.3	CHEMBL320685	-6.2	CHEMBL1093982	-6.1	DB06439	-6.1
CHEMBL335456	-6.3	CHEMBL320685	-6.2	CHEMBL129334	-6.1	DB06439	-6.1
CHEMBL335456	-6.3	CHEMBL330596	-6.2	CHEMBL287202	-6.1	DB08884	-6.1
CHEMBL339562	-6.3	CHEMBL331808	-6.2	CHEMBL287202	-6.1	DB08884	-6.1
CHEMBL355777	-6.3	CHEMBL3357964	-6.2	CHEMBL287202	-6.1	DB09296	-6.1
CHEMBL382203	-6.3	CHEMBL340774	-6.2	CHEMBL287202	-6.1	CHEMBL129334	-6.0
CHEMBL382203	-6.3	CHEMBL340774	-6.2	CHEMBL293562	-6.1	CHEMBL287202	-6.0
CHEMBL404031	-6.3	CHEMBL340774	-6.2	CHEMBL330596	-6.1	CHEMBL330596	-6.0
CHEMBL404031	-6.3	CHEMBL340774	-6.2	CHEMBL330596	-6.1	CHEMBL330596	-6.0
CHEMBL404813	-6.3	CHEMBL355777	-6.2	CHEMBL331808	-6.1	CHEMBL3357964	-6.0
CHEMBL434033	-6.3	CHEMBL355777	-6.2	CHEMBL331808	-6.1	CHEMBL3357964	-6.0
CHEMBL434033	-6.3	CHEMBL404031	-6.2	CHEMBL339562	-6.1	CHEMBL339562	-6.0
CHEMBL434033	-6.3	CHEMBL404813	-6.2	CHEMBL340774	-6.1	CHEMBL382203	-6.0
CHEMBL54110	-6.3	CHEMBL404813	-6.2	CHEMBL340774	-6.1	CHEMBL382203	-6.0
CHEMBL578124	-6.3	CHEMBL404813	-6.2	CHEMBL382203	-6.1	CHEMBL432984	-6.0
CHEMBL578343	-6.3	CHEMBL432984	-6.2	CHEMBL404031	-6.1	CHEMBL432984	-6.0
CHEMBL67944	-6.3	CHEMBL54110	-6.2	CHEMBL404031	-6.1	CHEMBL434033	-6.0
CHEMBL78459	-6.3	CHEMBL54110	-6.2	CHEMBL404813	-6.1	CHEMBL54110	-6.0
CHEMBL78459	-6.3	CHEMBL574931	-6.2	CHEMBL432984	-6.1	CHEMBL574931	-6.0
DB00256	-6.3	CHEMBL574931	-6.2	CHEMBL432984	-6.1	CHEMBL578343	-6.0
DB00410	-6.3	CHEMBL578124	-6.2	CHEMBL432984	-6.1	CHEMBL578343	-6.0
DB00410	-6.3	CHEMBL578124	-6.2	CHEMBL434033	-6.1	CHEMBL58760	-6.0
DB00460	-6.3	CHEMBL578124	-6.2	CHEMBL434033	-6.1	CHEMBL58760	-6.0
DB00541	-6.3	CHEMBL578124	-6.2	CHEMBL454263	-6.1	CHEMBL58760	-6.0
DB00615	-6.3	CHEMBL578343	-6.2	CHEMBL454263	-6.1	DB00410	-6.0
DB00743	-6.3	CHEMBL67944	-6.2	CHEMBL54110	-6.1	DB00541	-6.0
DB00743	-6.3	CHEMBL67944	-6.2	CHEMBL54110	-6.1	DB00743	-6.0
DB00976	-6.3	CHEMBL78459	-6.2	CHEMBL574931	-6.1	DB00743	-6.0
DB00976	-6.3	CHEMBL85651	-6.2	CHEMBL574931	-6.1	DB00743	-6.0
DB01076	-6.3	DB00309	-6.2	CHEMBL574931	-6.1	DB00743	-6.0
DB01118	-6.3	DB00410	-6.2	CHEMBL574931	-6.1	DB00746	-6.0
DB01220	-6.3	DB00410	-6.2	CHEMBL578124	-6.1	DB00746	-6.0
DB01602	-6.3	DB00541	-6.2	CHEMBL578124	-6.1	DB00746	-6.0
DB04845	-6.3	DB00743	-6.2	CHEMBL578343	-6.1	DB00746	-6.0
DB04845	-6.3	DB00947	-6.2	CHEMBL58760	-6.1	DB00864	-6.0
DB06439	-6.3	DB00947	-6.2	CHEMBL67944	-6.1	DB00864	-6.0

Ligand code	Docking score	Ligand code	Docking score	Ligand code	Docking score	Ligand code	Docking score
DB00864	-6.0	CHEMBL320685	-5.8	DB00570	-5.5	DB01764	-5.1
DB00976	-6.0	CHEMBL320685	-5.8	DB00570	-5.5	DB05109	-5.1
DB00976	-6.0	CHEMBL320685	-5.8	DB01201	-5.5	DB08965	-5.1
DB01076	-6.0	CHEMBL320685	-5.8	DB05109	-5.5	DB09296	-5.1
DB01076	-6.0	CHEMBL320685	-5.8	DB06772	-5.5	DB09296	-5.1
DB01076	-6.0	CHEMBL331808	-5.8	DB06772	-5.5	DB00207	-5.0
DB01118	-6.0	CHEMBL3357964	-5.8	DB09049	-5.5	DB00570	-5.0
DB01118	-6.0	CHEMBL432984	-5.8	DB09049	-5.5	DB00615	-5.0
DB01118	-6.0	CHEMBL58760	-5.8	CHEMBL564642	-5.4	DB00868	-5.0
DB01118	-6.0	CHEMBL58760	-5.8	CHEMBL564642	-5.4	DB01045	-5.0
DB01220	-6.0	CHEMBL58760	-5.8	CHEMBL564642	-5.4	DB01201	-5.0
DB01220	-6.0	DB00207	-5.8	CHEMBL564642	-5.4	DB01201	-5.0
DB01229	-6.0	DB00361	-5.8	DB00207	-5.4	DB01764	-5.0
DB01229	-6.0	DB00361	-5.8	DB00207	-5.4	DB09296	-5.0
DB01229	-6.0	DB00541	-5.8	DB00309	-5.4	CHEMBL454263	-4.9
DB04855	-6.0	DB00746	-5.8	DB00309	-5.4	DB08965	-4.9
DB04855	-6.0	DB01076	-5.8	DB00309	-5.4	DB09296	-4.9
DB04855	-6.0	DB04845	-5.8	DB00361	-5.4	CHEMBL454263	-4.8
DB04855	-6.0	DB06827	-5.8	DB00361	-5.4	DB00207	-4.8
DB04855	-6.0	CHEMBL293562	-5.7	DB00538	-5.4	DB00361	-4.8
DB05109	-6.0	CHEMBL293562	-5.7	DB00538	-5.4	DB00361	-4.8
DB05109	-6.0	CHEMBL293562	-5.7	DB00615	-5.4	DB00868	-4.8
DB05109	-6.0	CHEMBL331808	-5.7	DB01201	-5.4	DB00868	-4.8
DB06439	-6.0	CHEMBL339562	-5.7	DB01220	-5.4	DB01045	-4.8
DB06439	-6.0	CHEMBL432984	-5.7	DB08965	-5.4	DB01201	-4.8
DB06772	-6.0	DB00309	-5.7	DB09296	-5.4	CHEMBL454263	-4.7
DB08884	-6.0	DB00361	-5.7	CHEMBL339562	-5.3	DB00868	-4.7
DB08884	-6.0	DB00541	-5.7	CHEMBL454263	-5.3	DB01045	-4.7
DB08884	-6.0	DB00570	-5.7	DB00207	-5.3	DB01045	-4.7
DB08906	-6.0	DB01076	-5.7	DB00207	-5.3	DB01201	-4.7
CHEMBL129334	-5.9	DB01220	-5.7	DB00309	-5.3	DB01764	-4.7
CHEMBL293562	-5.9	DB01764	-5.7	DB00538	-5.3	DB06804	-4.7
CHEMBL293562	-5.9	DB06772	-5.7	DB00538	-5.3	DB09296	-4.7
CHEMBL320685	-5.9	DB06772	-5.7	DB00538	-5.3	CHEMBL454263	-4.6
CHEMBL331808	-5.9	DB06772	-5.7	DB00541	-5.3	DB00868	-4.6
CHEMBL331808	-5.9	DB06827	-5.7	DB00570	-5.3	DB00868	-4.6
CHEMBL339562	-5.9	DB06827	-5.7	DB08965	-5.3	DB06804	-4.6
CHEMBL339562	-5.9	CHEMBL331808	-5.6	DB08965	-5.3	DB06804	-4.6
CHEMBL432984	-5.9	CHEMBL339562	-5.6	DB09049	-5.3	DB09296	-4.6
CHEMBL54110	-5.9	CHEMBL339562	-5.6	DB09049	-5.3	DB00868	-4.5
CHEMBL54110	-5.9	CHEMBL564642	-5.6	CHEMBL454263	-5.2	DB00868	-4.5
CHEMBL58760	-5.9	CHEMBL564642	-5.6	DB00207	-5.2	DB00868	-4.5
CHEMBL58760	-5.9	CHEMBL564642	-5.6	DB00541	-5.2	DB01045	-4.5
CHEMBL67944	-5.9	CHEMBL564642	-5.6	DB00541	-5.2	DB01045	-4.5
DB00746	-5.9	CHEMBL564642	-5.6	DB00570	-5.2	DB06804	-4.5
DB00746	-5.9	DB00538	-5.6	DB00570	-5.2	DB06804	-4.5
DB00864	-5.9	DB00538	-5.6	DB00615	-5.2	DB00615	-4.4
DB00947	-5.9	DB00570	-5.6	DB01045	-5.2	DB06804	-4.4
DB01118	-5.9	DB00947	-5.6	DB01764	-5.2	DB06804	-4.4
DB04855	-5.9	DB00947	-5.6	DB05109	-5.2	DB06804	-4.4
DB04855	-5.9	DB01764	-5.6	DB06772	-5.2	DB06804	-4.4
DB04855	-5.9	DB08965	-5.6	DB09049	-5.2	DB08965	-4.2
DB06827	-5.9	DB09049	-5.6	DB09049	-5.2	DB00615	-4.1
DB09049	-5.9	DB00207	-5.5	DB09049	-5.2	DB01201	-4.0
CHEMBL129334	-5.8	DB00309	-5.5	CHEMBL454263	-5.1	DB08965	-4.0
CHEMBL293562	-5.8	DB00538	-5.5	DB00570	-5.1	DB08965	-4.0
CHEMBL293562	-5.8	DB00538	-5.5	DB00615	-5.1	DB01201	-3.7
CHEMBL293562	-5.8	DB00541	-5.5	DB01045	-5.1	DB01201	-3.7

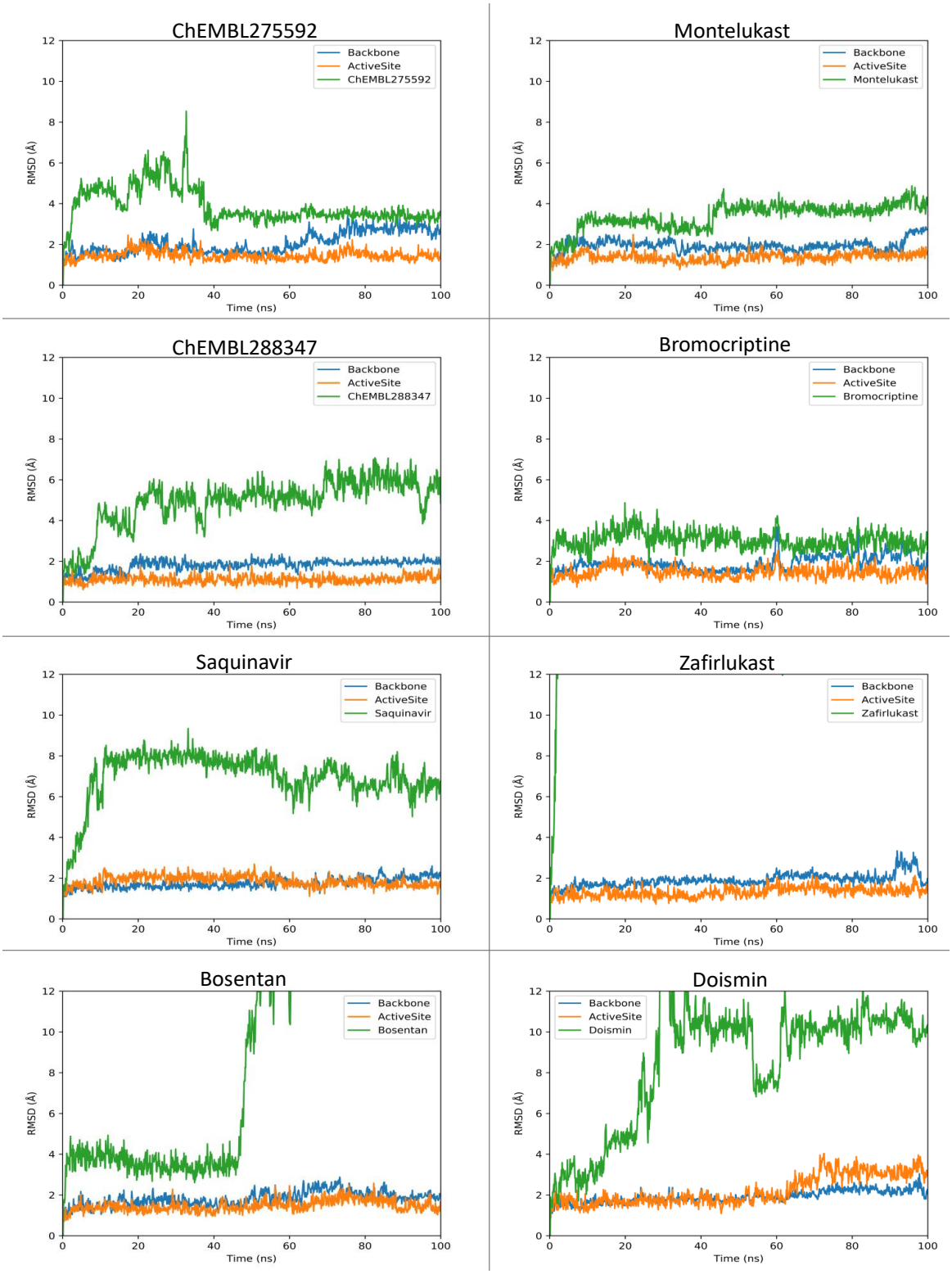

Figure B.1: RMSD analysis of the top docking compounds complexed individually with the Mpro.

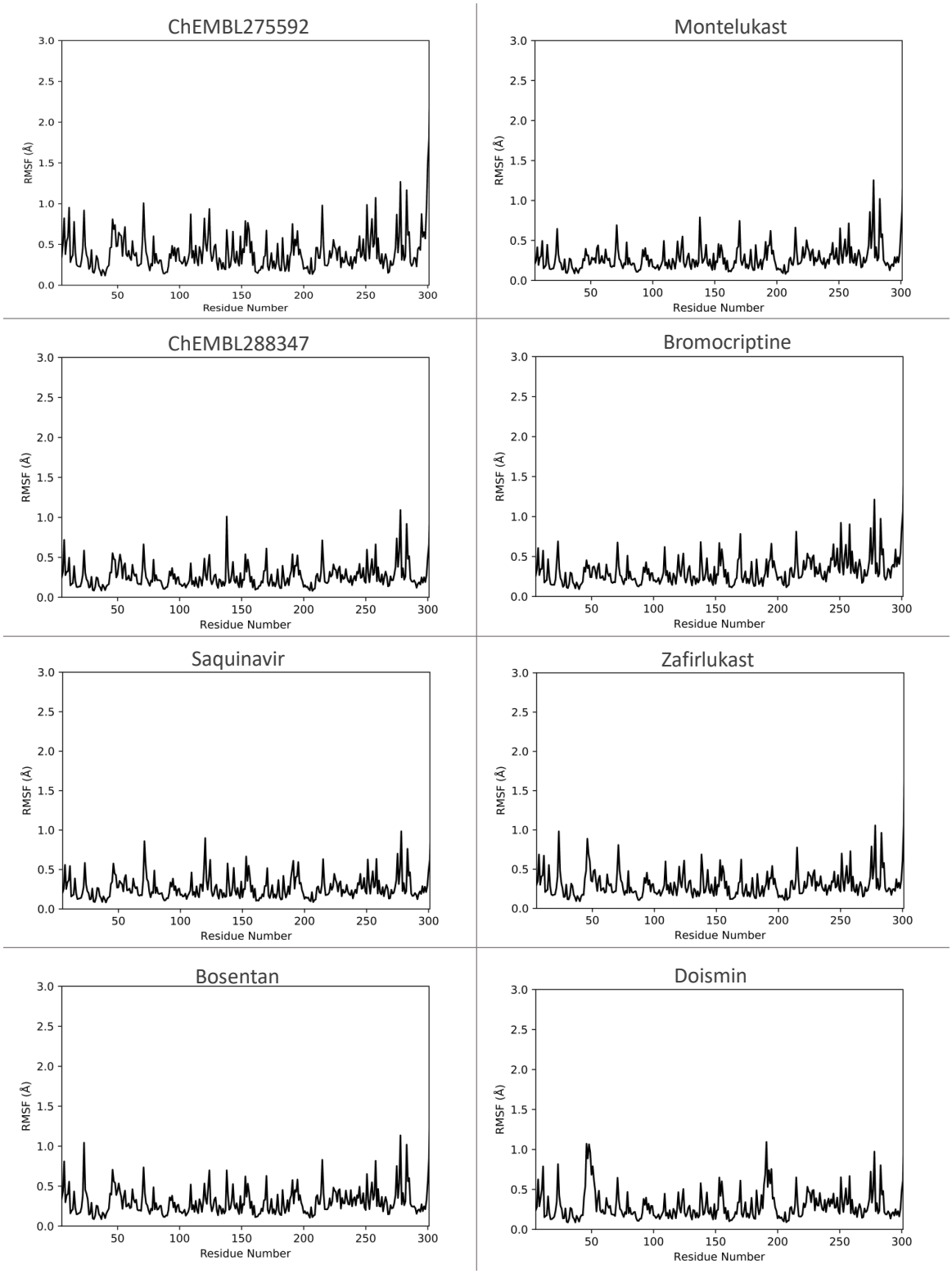

Figure B.2: RMSF analysis of the top docking compounds complexed individually with the Mpro.

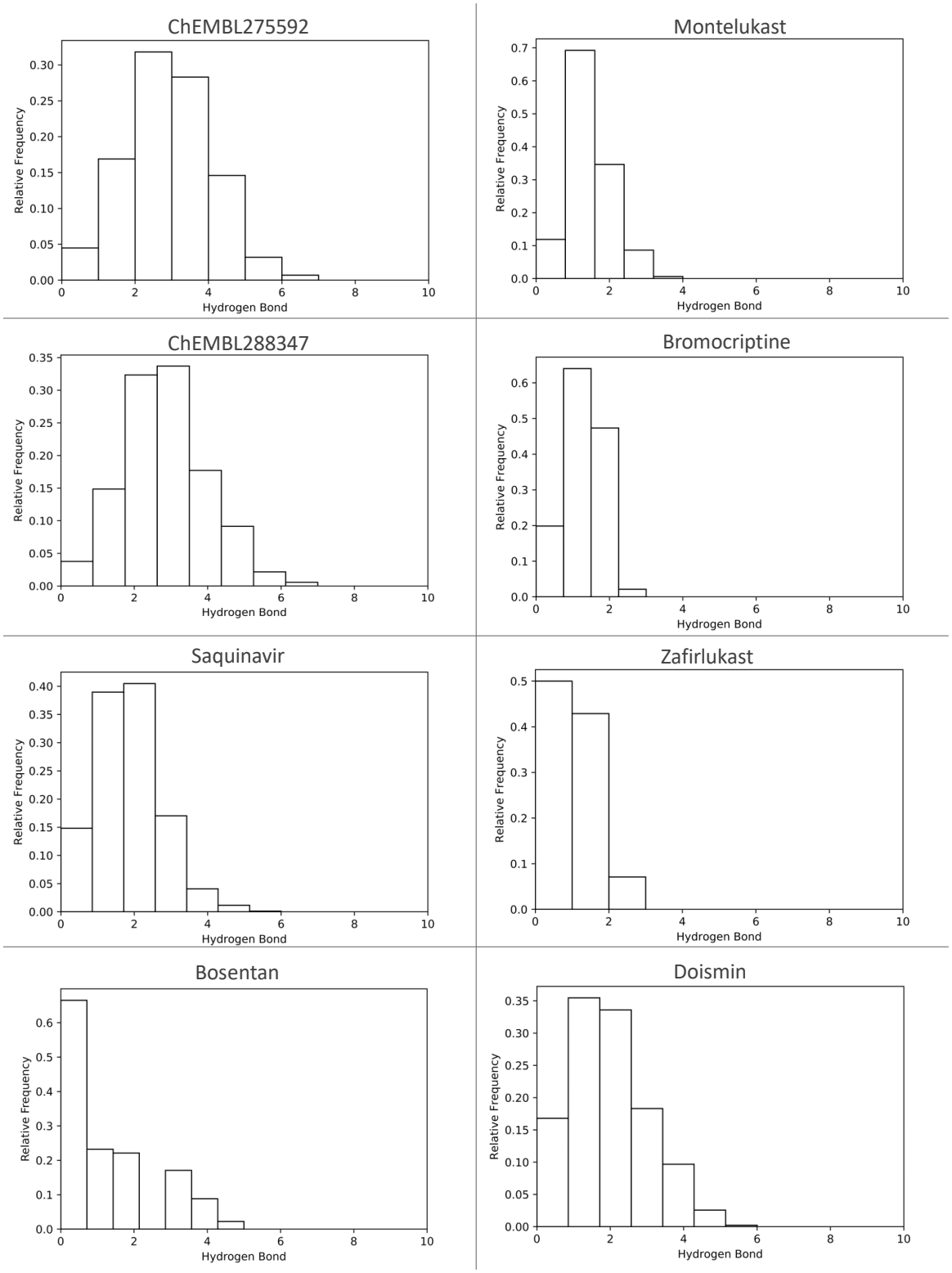

Figure B.3: Averaged hydrogen bond interactions of the top docking compounds complexed individually with the Mpro during the 100 ns NPT ensemble.

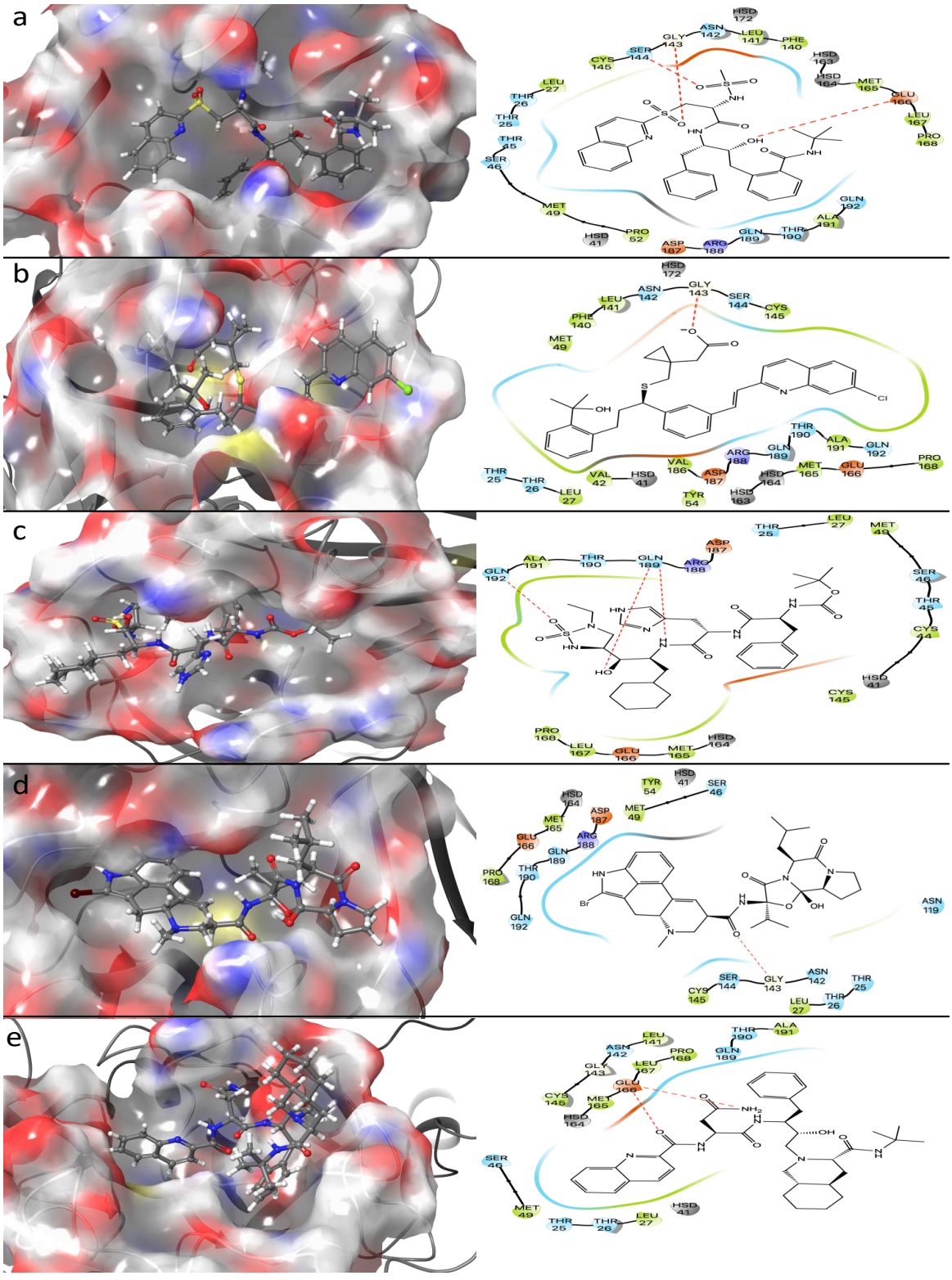

Figure B.4: (a) ChEMBL275592, (b) montelukast, (c) ChEMBL288347, (d) bromocriptine, (e) saquinavir. (Left) representative pose of the stable compounds of the last frame of the 100 ns NPT ensemble, where, the protein surface is colored based on the electrostatic potential. (Right) the red dashed line represents hydrogen bond interactions of the stable compounds in complex with the Mpro.

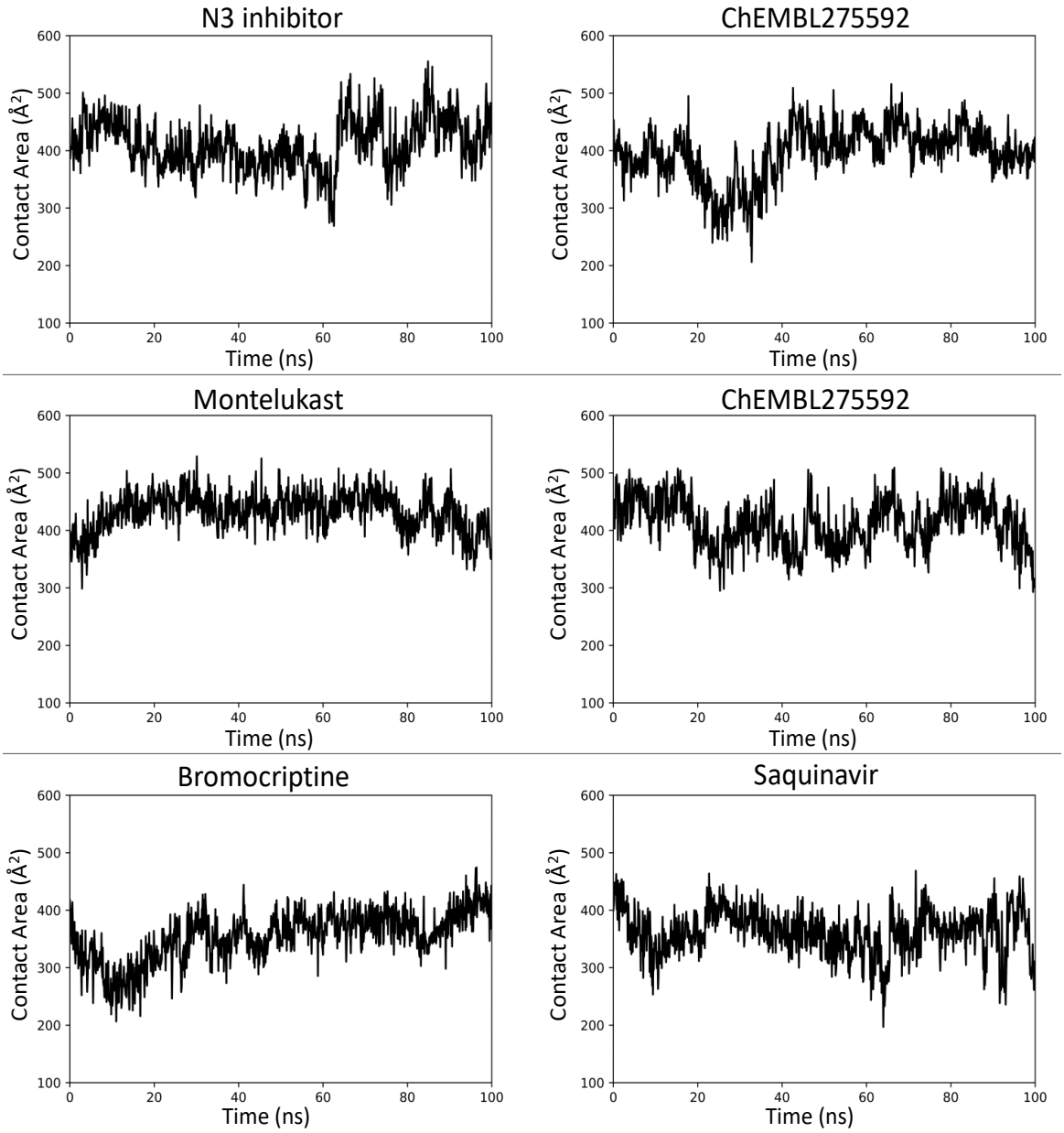

Figure B.5: The time-dependent evolution of the contact surface area during the 100 ns NPT ensemble.

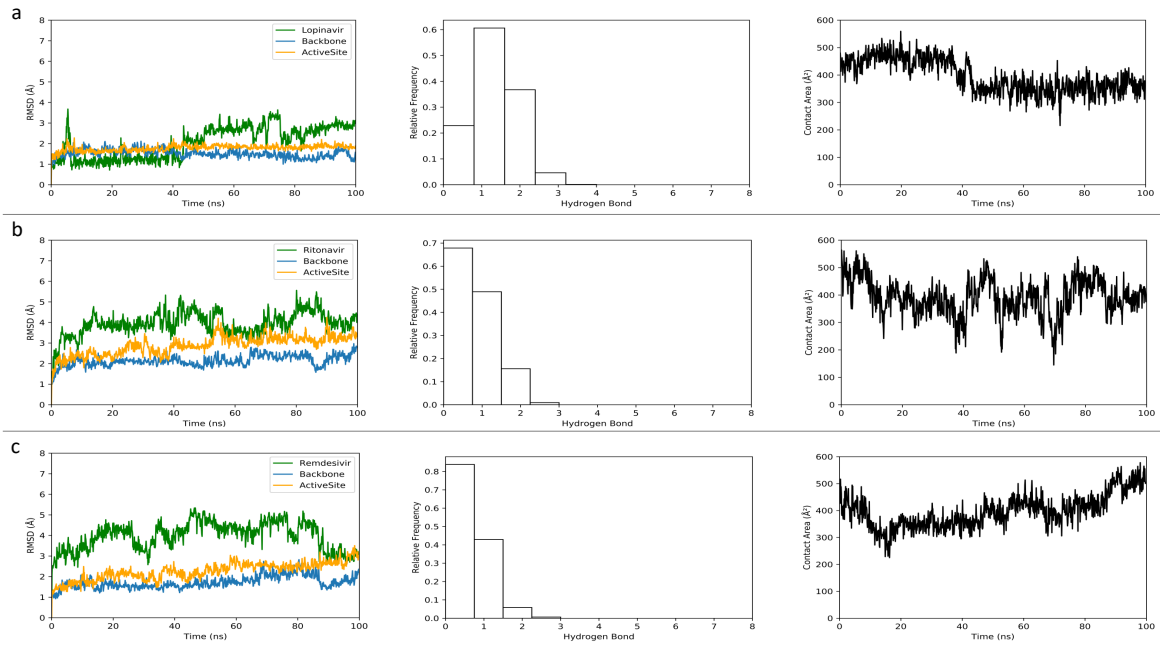

Figure B.6: RMSD, averaged hydrogen bond interaction, and the contact surface area of lopinavir (a), ritonavir (b), and remdesivir (c) complexed individually with the Mpro.

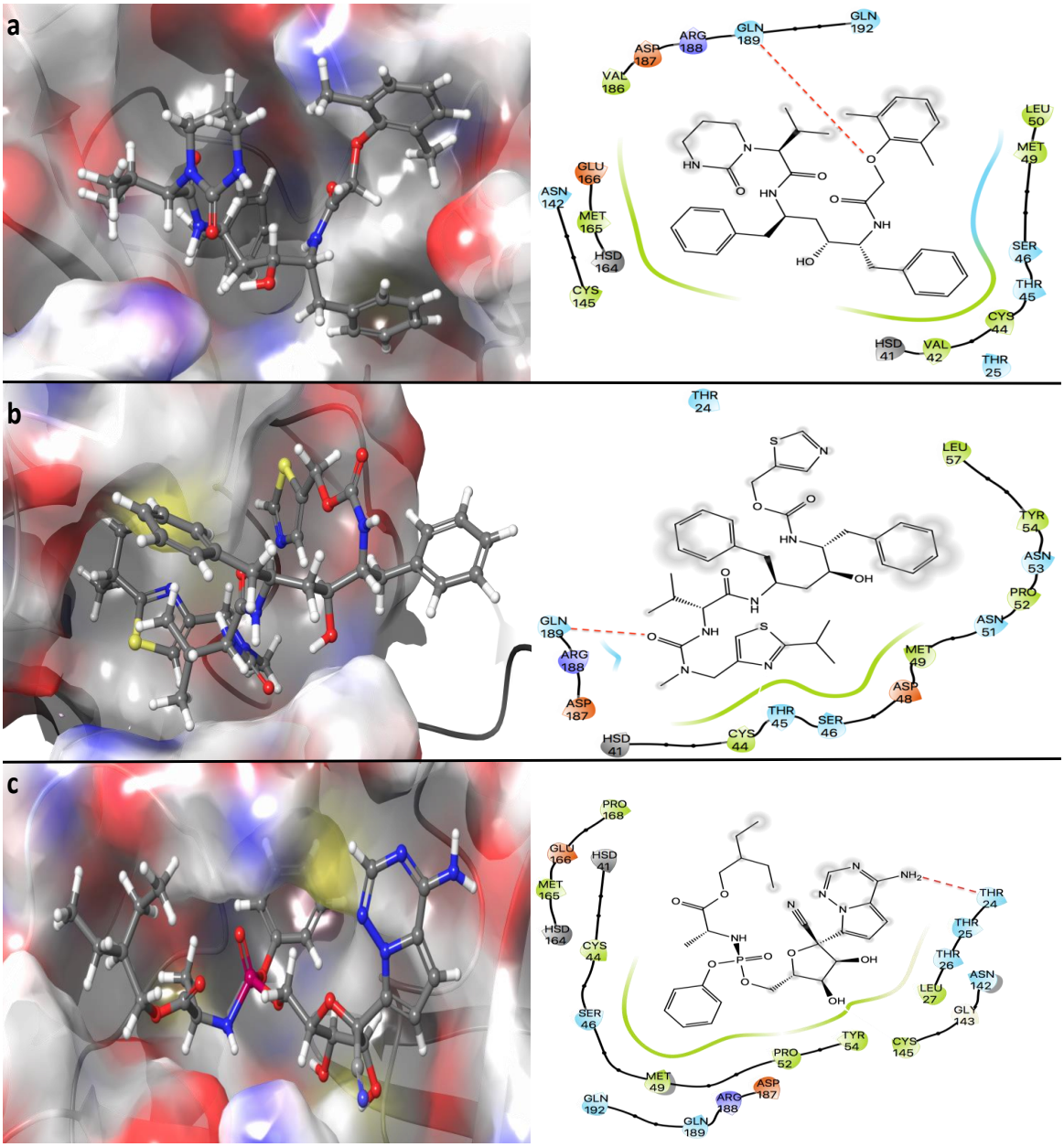

Figure B.7: (a) lopinavir, (b) ritonavir, (c) remdesivir. (Left) representative pose of antiviral drugs of the last frame of the 100 ns NPT ensemble, where, the protein surface is colored based on the electrostatic potential. (Right) the red dashed line represents hydrogen bond interactions of antiviral drugs in complex with the Mpro.

C

Discovery of Potent Inhibitors for SARS-CoV-2's Spike Protein

Table C.1: Docking results of compounds in kcal mol^{-1} for SARS-CoV-2 Spike RBD

Ligand (ZINC ID)	Docking scores			Ligand (ZINC ID)	Docking scores			Ligand (ZINC ID)	Docking scores		
	Vina	Kdeep	Consensus		Vina	Kdeep	Consensus		Vina	Kdeep	Consensus
ZINC000006717782	-9.2	-9.4	-9.3	ZINC000095617639	-7.7	-9.1	-8.4	ZINC000100045486	-8.3	-8.0	-8.2
ZINC000095628821	-8.7	-9.8	-9.3	ZINC000003841623	-7.4	-9.4	-8.4	ZINC000072131401	-7.6	-8.7	-8.2
ZINC000253638647	-8.3	-10.1	-9.2	ZINC000034016416	-7.8	-9.0	-8.4	ZINC000150339331	-7.5	-8.8	-8.2
ZINC000003979524	-8.6	-9.7	-9.2	ZINC000242548690	-8.1	-8.7	-8.4	ZINC000072190231	-7.2	-9.1	-8.2
ZINC000253387884	-8.4	-9.8	-9.1	ZINC000685933070	-6.2	-10.6	-8.4	ZINC000085536932	-6.7	-9.6	-8.2
ZINC000255977094	-8.7	-9.4	-9.1	ZINC000060392779	-7.9	-8.9	-8.4	ZINC000014879999	-7.8	-8.5	-8.2
ZINC000150339052	-8.8	-9.3	-9.1	ZINC000095617641	-7.8	-9.0	-8.4	ZINC000100370145	-7.7	-8.6	-8.2
ZINC000261494659	-8.3	-9.8	-9.1	ZINC000084758235	-7.9	-8.8	-8.4	ZINC000085537053	-7.6	-8.7	-8.2
ZINC000936069565	-8.1	-9.9	-9.0	ZINC000256630463	-8.2	-8.5	-8.4	ZINC000261494652	-7.4	-8.9	-8.2
ZINC000051951669	-8.9	-9.0	-9.0	ZINC000169362009	-5.9	-10.8	-8.4	ZINC000002005848	-7.7	-8.5	-8.1
ZINC000049637509	-7.7	-10.2	-9.0	ZINC000085563461	-7.2	-9.5	-8.4	ZINC000257362202	-7.8	-8.4	-8.1
ZINC000261494658	-8.0	-9.9	-9.0	ZINC000100014909	-7.7	-9.0	-8.4	ZINC000299841502	-7.7	-8.5	-8.1
ZINC000095617623	-7.7	-10.2	-9.0	ZINC000001494900	-8.8	-7.9	-8.4	ZINC000096178757	-7.1	-9.1	-8.1
ZINC000118915216	-9.0	-8.8	-8.9	ZINC000026985532	-8.4	-8.3	-8.4	ZINC000261494653	-7.6	-8.6	-8.1
ZINC000118915217	-9.0	-8.8	-8.9	ZINC000095609799	-7.2	-9.5	-8.4	ZINC000085563455	-7.2	-9.0	-8.1
ZINC000017837457	-7.4	-10.4	-8.9	ZINC000098043800	-7.7	-9.0	-8.4	ZINC000049783788	-7.4	-8.8	-8.1
ZINC000100285161	-8.6	-9.2	-8.9	ZINC000003939013	-8.1	-8.6	-8.4	ZINC000299818013	-7.2	-9.0	-8.1
ZINC000043203371	-9.5	-8.2	-8.9	ZINC000028232746	-8.1	-8.6	-8.4	ZINC000011616154	-7.8	-8.4	-8.1
ZINC000095617622	-8.0	-9.7	-8.9	ZINC000159897988	-8.3	-8.4	-8.4	ZINC000024811973	-7.4	-8.8	-8.1
ZINC000118915214	-9.1	-8.6	-8.9	ZINC000169676912	-7.5	-9.1	-8.3	ZINC000169292272	-6.2	-10.0	-8.1
ZINC000072190221	-8.1	-9.6	-8.9	ZINC000410428645	-7.7	-8.9	-8.3	ZINC000085432544	-6.9	-9.3	-8.1
ZINC000001538857	-7.2	-10.4	-8.8	ZINC000036701290	-7.7	-8.9	-8.3	ZINC000169677010	-7.0	-9.2	-8.1
ZINC000011616153	-8.1	-9.5	-8.8	ZINC000014768469	-8.4	-8.2	-8.3	ZINC000256015223	-7.2	-9.0	-8.1
ZINC000043195317	-9.0	-8.6	-8.8	ZINC000043205655	-7.3	-9.3	-8.3	ZINC000100054232	-9.0	-7.2	-8.1
ZINC000256630449	-8.5	-9.1	-8.8	ZINC000004633134	-8.6	-8.0	-8.3	ZINC000034016204	-7.0	-9.2	-8.1
ZINC000095617624	-8.0	-9.5	-8.8	ZINC000003939238	-7.4	-9.2	-8.3	ZINC000095619124	-7.7	-8.5	-8.1
ZINC000043100810	-8.4	-9.1	-8.8	ZINC000005328059	-7.8	-8.8	-8.3	ZINC000085563452	-8.2	-8.0	-8.1
ZINC000205341959	-8.1	-9.4	-8.8	ZINC000068120928	-7.0	-9.6	-8.3	ZINC000043129461	-6.8	-9.4	-8.1
ZINC000255977092	-9.1	-8.4	-8.8	ZINC000072318121	-8.4	-8.2	-8.3	ZINC000169368439	-7.2	-9.0	-8.1
ZINC000003954692	-7.4	-10.0	-8.7	ZINC000006717510	-7.8	-8.7	-8.3	ZINC000031597289	-6.9	-9.2	-8.1
ZINC000255977093	-8.2	-9.2	-8.7	ZINC000256109538	-7.9	-8.6	-8.3	ZINC000169737128	-8.5	-7.6	-8.1
ZINC000014210642	-8.0	-9.4	-8.7	ZINC000261494651	-7.9	-8.6	-8.3	ZINC000072190171	-7.2	-8.9	-8.1
ZINC000011616152	-7.6	-9.8	-8.7	ZINC000150564146	-6.6	-9.9	-8.3	ZINC000009574552	-8.0	-8.1	-8.1
ZINC000003977803	-8.1	-9.3	-8.7	ZINC000169734975	-6.8	-9.7	-8.3	ZINC000005328058	-7.8	-8.3	-8.1
ZINC000095627892	-7.9	-9.4	-8.7	ZINC000072316197	-8.1	-8.4	-8.3	ZINC000091302264	-7.2	-8.9	-8.1
ZINC000261494656	-8.0	-9.3	-8.7	ZINC000150339325	-8.1	-8.4	-8.3	ZINC000200157567	-7.0	-9.1	-8.1
ZINC000169289417	-7.7	-9.6	-8.7	ZINC000135667247	-7.8	-8.7	-8.3	ZINC000299872475	-6.9	-9.2	-8.1
ZINC000150339320	-7.4	-9.9	-8.7	ZINC000261527110	-8.7	-7.8	-8.3	ZINC000936070151	-6.9	-9.2	-8.1
ZINC000013986815	-8.4	-8.8	-8.6	ZINC000022443609	-7.0	-9.5	-8.3	ZINC000031597285	-7.0	-9.1	-8.1
ZINC000095617626	-7.3	-9.9	-8.6	ZINC000053006885	-7.3	-9.2	-8.3	ZINC000135667290	-7.2	-8.9	-8.1
ZINC000058540931	-8.0	-9.2	-8.6	ZINC000003917787	-6.6	-9.9	-8.3	ZINC000028232755	-7.5	-8.5	-8.0
ZINC000261494590	-6.0	-11.2	-8.6	ZINC000095617679	-6.7	-9.8	-8.3	ZINC000003918583	-8.1	-7.9	-8.0
ZINC000085537142	-8.2	-9.0	-8.6	ZINC000004099104	-7.9	-8.6	-8.3	ZINC000027420855	-7.3	-8.7	-8.0
ZINC000602986377	-8.5	-8.7	-8.6	ZINC000095617637	-7.5	-9.0	-8.3	ZINC000685933074	-6.9	-9.1	-8.0
ZINC000164528615	-8.8	-8.4	-8.6	ZINC000159898174	-7.7	-8.8	-8.3	ZINC000072266997	-7.1	-8.9	-8.0
ZINC000003831231	-7.8	-9.3	-8.6	ZINC000198558594	-8.3	-8.2	-8.3	ZINC000150341961	-5.9	-10.1	-8.0
ZINC000206179007	-8.6	-8.5	-8.6	ZINC000095618743	-8.1	-8.4	-8.3	ZINC000003873936	-7.2	-8.8	-8.0
ZINC000095539929	-6.6	-10.5	-8.6	ZINC000299888511	-6.2	-10.2	-8.2	ZINC000028232750	-7.5	-8.5	-8.0
ZINC000013660214	-8.6	-8.4	-8.5	ZINC000003935603	-7.9	-8.5	-8.2	ZINC000256015224	-6.2	-9.8	-8.0
ZINC000299841484	-7.1	-9.9	-8.5	ZINC000016697102	-6.7	-9.7	-8.2	ZINC000095609798	-6.8	-9.2	-8.0
ZINC000299841511	-7.4	-9.6	-8.5	ZINC000299818020	-8.4	-8.0	-8.2	ZINC000095618867	-7.5	-8.5	-8.0
ZINC000252474776	-8.1	-8.9	-8.5	ZINC000026664090	-7.9	-8.5	-8.2	ZINC000003994495	-7.8	-8.2	-8.0
ZINC000095618827	-8.3	-8.7	-8.5	ZINC000001490807	-7.2	-9.2	-8.2	ZINC000087496183	-6.5	-9.5	-8.0
ZINC000085432549	-6.7	-10.3	-8.5	ZINC000003842872	-7.3	-9.1	-8.2	ZINC000100071772	-7.5	-8.5	-8.0
ZINC000150354122	-7.2	-9.8	-8.5	ZINC000038141706	-7.7	-8.7	-8.2	ZINC000014096578	-7.1	-8.9	-8.0
ZINC000248087828	-7.0	-10.0	-8.5	ZINC000118915215	-7.5	-8.9	-8.2	ZINC000095618866	-7.6	-8.3	-8.0
ZINC000256630457	-8.3	-8.7	-8.5	ZINC000013478606	-7.6	-8.8	-8.2	ZINC000003926844	-7.8	-8.1	-8.0
ZINC000024447427	-8.1	-8.8	-8.5	ZINC000028639340	-7.5	-8.9	-8.2	ZINC000026844771	-6.9	-9.0	-8.0
ZINC000085536958	-7.2	-9.7	-8.5	ZINC000255990532	-6.8	-9.6	-8.2	ZINC000100054212	-7.5	-8.4	-8.0
ZINC000049757175	-8.3	-8.6	-8.5	ZINC000003938482	-7.4	-8.9	-8.2	ZINC000008214621	-7.0	-8.9	-8.0
ZINC000029571072	-7.9	-9.0	-8.5	ZINC000095618689	-8.2	-8.1	-8.2	ZINC000299841496	-7.0	-8.9	-8.0
ZINC000009574770	-7.6	-9.3	-8.5	ZINC000043202140	-6.7	-9.6	-8.2	ZINC000014175498	-7.9	-8.0	-8.0
ZINC000003941496	-7.7	-9.1	-8.4	ZINC000685933136	-7.9	-8.4	-8.2	ZINC000256015222	-6.7	-9.2	-8.0
ZINC000095618916	-7.6	-9.2	-8.4	ZINC000085537024	-6.8	-9.5	-8.2	ZINC000299873007	-7.1	-8.8	-8.0

Ligand (ZINC ID)	Docking scores			Ligand (ZINC ID)	Docking scores			Ligand (ZINC ID)	Docking scores		
	Vina	Kdeep	Consensus		Vina	Kdeep	Consensus		Vina	Kdeep	Consensus
ZINC000035310420	-8.0	-7.9	-8.0	ZINC000261494572	-6.5	-9.0	-7.8	ZINC000095618672	-6.9	-8.4	-7.7
ZINC000064622628	-6.9	-9.0	-8.0	ZINC000008143568	-8.2	-7.3	-7.8	ZINC000100054201	-6.9	-8.4	-7.7
ZINC000003834191	-6.8	-9.1	-8.0	ZINC000065731488	-6.8	-8.7	-7.8	ZINC000101687676	-5.8	-9.5	-7.7
ZINC000003946372	-7.2	-8.7	-8.0	ZINC000038913962	-6.4	-9.1	-7.8	ZINC000195913944	-6.6	-8.7	-7.7
ZINC000043128366	-7.9	-8.0	-8.0	ZINC000003951740	-7.0	-8.5	-7.8	ZINC000095618662	-6.5	-8.8	-7.7
ZINC000299841503	-7.0	-8.9	-8.0	ZINC000043208634	-7.6	-7.9	-7.8	ZINC000077300876	-7.3	-8.0	-7.7
ZINC000068267814	-8.3	-7.5	-7.9	ZINC000096061888	-5.9	-9.6	-7.8	ZINC000169292819	-7.4	-7.9	-7.7
ZINC000299841497	-8.3	-7.5	-7.9	ZINC000261106252	-7.0	-8.5	-7.8	ZINC000299841535	-7.4	-7.9	-7.7
ZINC000003916787	-7.6	-8.2	-7.9	ZINC000085540202	-7.3	-8.2	-7.8	ZINC000095618745	-7.0	-8.3	-7.7
ZINC000253668332	-7.5	-8.3	-7.9	ZINC000004149248	-6.6	-8.9	-7.8	ZINC000095627834	-7.1	-8.2	-7.7
ZINC000095618881	-7.6	-8.2	-7.9	ZINC000095617636	-7.8	-7.7	-7.8	ZINC000003929793	-8.5	-6.7	-7.6
ZINC000299841510	-6.9	-8.9	-7.9	ZINC000169289419	-6.6	-8.9	-7.8	ZINC000039187987	-6.6	-8.6	-7.6
ZINC000029058869	-7.7	-8.1	-7.9	ZINC000003918087	-6.8	-8.7	-7.8	ZINC000085548251	-7.3	-7.9	-7.6
ZINC000169360219	-6.7	-9.1	-7.9	ZINC000043103796	-6.8	-8.7	-7.8	ZINC000169742991	-8.3	-6.9	-7.6
ZINC000252441679	-7.1	-8.7	-7.9	ZINC000085540119	-8.1	-7.4	-7.8	ZINC000169621219	-7.4	-7.8	-7.6
ZINC000253947047	-7.0	-8.8	-7.9	ZINC000118915220	-7.3	-8.2	-7.8	ZINC000049841054	-7.0	-8.2	-7.6
ZINC000094303244	-6.5	-9.3	-7.9	ZINC000169289411	-6.6	-8.9	-7.8	ZINC000150339587	-7.4	-7.8	-7.6
ZINC000095627836	-7.5	-8.3	-7.9	ZINC000114022496	-7.3	-8.2	-7.8	ZINC000003925398	-6.5	-8.7	-7.6
ZINC000114367761	-7.0	-8.8	-7.9	ZINC000096095661	-5.8	-9.7	-7.8	ZINC000003961863	-5.9	-9.3	-7.6
ZINC000169292343	-7.0	-8.7	-7.9	ZINC000118913657	-7.3	-8.2	-7.8	ZINC000004097459	-6.6	-8.6	-7.6
ZINC000003915154	-7.1	-8.6	-7.9	ZINC000195961425	-6.9	-8.6	-7.8	ZINC000043211394	-6.1	-9.1	-7.6
ZINC000042921858	-8.3	-7.4	-7.9	ZINC000198051674	-8.0	-7.5	-7.8	ZINC000169307271	-6.5	-8.7	-7.6
ZINC000113476229	-6.9	-8.8	-7.9	ZINC000200157407	-6.6	-8.8	-7.7	ZINC000261494619	-6.6	-8.6	-7.6
ZINC000169362007	-7.0	-8.7	-7.9	ZINC000299818012	-6.9	-8.5	-7.7	ZINC000169344691	-7.9	-7.3	-7.6
ZINC000195932465	-7.2	-8.5	-7.9	ZINC000885764928	-9.0	-6.4	-7.7	ZINC000245224178	-6.7	-8.5	-7.6
ZINC000299841534	-7.3	-8.4	-7.9	ZINC000003920372	-7.1	-8.3	-7.7	ZINC000261494616	-6.6	-8.6	-7.6
ZINC000003955219	-7.1	-8.6	-7.9	ZINC000003830431	-7.1	-8.3	-7.7	ZINC000013916432	-5.9	-9.3	-7.6
ZINC000001482077	-7.6	-8.1	-7.9	ZINC000085540112	-6.7	-8.7	-7.7	ZINC000003978005	-9.7	-5.5	-7.6
ZINC000001612996	-7.9	-7.8	-7.9	ZINC000085540154	-6.4	-9.0	-7.7	ZINC000261494632	-6.1	-9.1	-7.6
ZINC000100054208	-6.3	-9.4	-7.9	ZINC000095544807	-6.4	-9.0	-7.7	ZINC000261494691	-7.1	-8.1	-7.6
ZINC000169369935	-6.3	-9.4	-7.9	ZINC000252548735	-5.9	-9.5	-7.7	ZINC000016052714	-7.7	-7.5	-7.6
ZINC000195752095	-5.8	-9.9	-7.9	ZINC000043153259	-7.6	-7.8	-7.7	ZINC000029562299	-7.1	-8.1	-7.6
ZINC000003917481	-7.1	-8.6	-7.9	ZINC000299888871	-7.4	-8.0	-7.7	ZINC000003994828	-7.2	-8.0	-7.6
ZINC000095618868	-6.6	-9.1	-7.9	ZINC000685933073	-5.9	-9.5	-7.7	ZINC000006716615	-6.0	-9.2	-7.6
ZINC000261494626	-6.6	-9.1	-7.9	ZINC000118915335	-7.3	-8.1	-7.7	ZINC000008234351	-7.1	-8.1	-7.6
ZINC000003817327	-8.6	-7.1	-7.9	ZINC000072284069	-6.9	-8.5	-7.7	ZINC000118913655	-7.4	-7.8	-7.6
ZINC000000643153	-7.1	-8.6	-7.9	ZINC000008215434	-7.2	-8.2	-7.7	ZINC000253855706	-6.5	-8.7	-7.6
ZINC000003914982	-7.1	-8.6	-7.9	ZINC000118795962	-7.9	-7.5	-7.7	ZINC000206792055	-7.0	-8.1	-7.6
ZINC000014943121	-7.2	-8.5	-7.9	ZINC000118915221	-7.7	-7.7	-7.7	ZINC000003977942	-7.2	-7.9	-7.6
ZINC000028864451	-8.6	-7.1	-7.9	ZINC000043195938	-7.6	-7.8	-7.7	ZINC000169356816	-6.3	-8.8	-7.6
ZINC000169737127	-7.8	-7.9	-7.9	ZINC000169292415	-5.9	-9.5	-7.7	ZINC000000643046	-5.1	-10.0	-7.6
ZINC000095092799	-8.5	-7.1	-7.8	ZINC000256079353	-7.4	-8.0	-7.7	ZINC000036126689	-7.5	-7.6	-7.6
ZINC000100472223	-7.0	-8.6	-7.8	ZINC000096006020	-7.1	-8.3	-7.7	ZINC000163677483	-7.7	-7.4	-7.6
ZINC000256109542	-7.6	-8.0	-7.8	ZINC000003807172	-6.1	-9.3	-7.7	ZINC000042893657	-7.6	-7.5	-7.6
ZINC000100036919	-6.7	-8.9	-7.8	ZINC000022058728	-7.7	-7.7	-7.7	ZINC000218037687	-7.1	-8.0	-7.6
ZINC000087496429	-6.9	-8.7	-7.8	ZINC000095618746	-7.0	-8.4	-7.7	ZINC000043202993	-7.5	-7.6	-7.6
ZINC000150338703	-6.2	-9.4	-7.8	ZINC000085914855	-7.3	-8.0	-7.7	ZINC000077313075	-8.1	-7.0	-7.6
ZINC000043202455	-7.4	-8.2	-7.8	ZINC000096258164	-7.7	-7.6	-7.7	ZINC000095610808	-7.0	-8.1	-7.6
ZINC000014261579	-7.3	-8.3	-7.8	ZINC000118868440	-6.8	-8.5	-7.7	ZINC000139868161	-7.4	-7.7	-7.6
ZINC000100067477	-7.4	-8.2	-7.8	ZINC000085537068	-8.1	-7.2	-7.7	ZINC000003809192	-6.9	-8.2	-7.6
ZINC000003872994	-7.3	-8.3	-7.8	ZINC000222108067	-6.7	-8.6	-7.7	ZINC000003989268	-7.4	-7.7	-7.6
ZINC000095551509	-7.9	-7.7	-7.8	ZINC000256079355	-7.4	-7.9	-7.7	ZINC000135848905	-6.1	-9.0	-7.6
ZINC000003932085	-6.9	-8.7	-7.8	ZINC000100053651	-6.4	-8.9	-7.7	ZINC000014768568	-7.6	-7.5	-7.6
ZINC000001485409	-7.2	-8.4	-7.8	ZINC000299841487	-6.3	-9.0	-7.7	ZINC000095618749	-7.8	-7.3	-7.6
ZINC000043211396	-7.4	-8.2	-7.8	ZINC000169734819	-7.8	-7.5	-7.7	ZINC000004098512	-7.6	-7.5	-7.6
ZINC000299818016	-7.7	-7.9	-7.8	ZINC000003950898	-7.0	-8.3	-7.7	ZINC000004215257	-7.2	-7.9	-7.6
ZINC000095618869	-6.4	-9.2	-7.8	ZINC000036412221	-7.5	-7.8	-7.7	ZINC000049852136	-5.8	-9.3	-7.6
ZINC000207704741	-7.5	-8.1	-7.8	ZINC000043131420	-6.7	-8.6	-7.7	ZINC000203757351	-8.2	-6.9	-7.6
ZINC000058660990	-7.3	-8.3	-7.8	ZINC000095538159	-6.4	-8.9	-7.7	ZINC000255991347	-7.0	-8.1	-7.6
ZINC000085537008	-6.3	-9.3	-7.8	ZINC000113459996	-7.7	-7.6	-7.7	ZINC000195988313	-6.7	-8.4	-7.6
ZINC000003931527	-7.5	-8.0	-7.8	ZINC000299888867	-8.0	-7.3	-7.7	ZINC000040165257	-7.6	-7.5	-7.6
ZINC000003774999	-6.5	-9.0	-7.8	ZINC000095627868	-6.1	-9.2	-7.7	ZINC000064490563	-8.1	-7.0	-7.6
ZINC000111460375	-7.4	-8.1	-7.8	ZINC000150339055	-6.8	-8.5	-7.7	ZINC000049942502	-6.7	-8.4	-7.6
ZINC000257362266	-7.5	-8.0	-7.8	ZINC000160587624	-8.0	-7.3	-7.7	ZINC000095618804	-5.9	-9.2	-7.6

Ligand (ZINC ID)	Docking scores			Ligand (ZINC ID)	Docking scores			Ligand (ZINC ID)	Docking scores		
	Vina	Kdeep	Consensus		Vina	Kdeep	Consensus		Vina	Kdeep	Consensus
ZINC000100054527	-7.3	-7.8	-7.6	ZINC000208938373	-7.6	-7.2	-7.4	ZINC000003920027	-5.9	-8.7	-7.3
ZINC000150339966	-7.1	-8.0	-7.6	ZINC000001485626	-6.8	-8.0	-7.4	ZINC000035985971	-8.4	-6.2	-7.3
ZINC000257362220	-6.9	-8.2	-7.6	ZINC000068246506	-6.8	-8.0	-7.4	ZINC000068106569	-5.4	-9.2	-7.3
ZINC000004099008	-7.0	-8.1	-7.6	ZINC000003917445	-7.1	-7.7	-7.4	ZINC000100054519	-6.9	-7.7	-7.3
ZINC000098052868	-7.5	-7.6	-7.6	ZINC000054053579	-5.8	-9.0	-7.4	ZINC000043206033	-6.9	-7.7	-7.3
ZINC000169621211	-7.2	-7.9	-7.6	ZINC000085537084	-6.6	-8.2	-7.4	ZINC000094303245	-6.9	-7.7	-7.3
ZINC000261494713	-6.3	-8.8	-7.6	ZINC000095618883	-7.3	-7.5	-7.4	ZINC000253848650	-7.4	-7.2	-7.3
ZINC000000643143	-6.8	-8.2	-7.5	ZINC000096077632	-6.3	-8.5	-7.4	ZINC000003952216	-7.6	-7.0	-7.3
ZINC000008143614	-7.5	-7.5	-7.5	ZINC000100054067	-6.9	-7.9	-7.4	ZINC000004102171	-6.9	-7.7	-7.3
ZINC000043450326	-6.8	-8.2	-7.5	ZINC000261527109	-8.5	-6.3	-7.4	ZINC000004474682	-5.9	-8.7	-7.3
ZINC000095618879	-7.8	-7.2	-7.5	ZINC000003994903	-7.5	-7.3	-7.4	ZINC000095618882	-7.4	-7.2	-7.3
ZINC000100073786	-7.3	-7.7	-7.5	ZINC000299841501	-7.4	-7.4	-7.4	ZINC000100053654	-6.5	-8.1	-7.3
ZINC000144743928	-6.7	-8.3	-7.5	ZINC000008214420	-6.7	-8.1	-7.4	ZINC000169733140	-7.3	-7.3	-7.3
ZINC000004215812	-8.5	-6.5	-7.5	ZINC000072206342	-6.9	-7.9	-7.4	ZINC000245190611	-7.7	-6.9	-7.3
ZINC000118915219	-6.9	-8.1	-7.5	ZINC000072284064	-7.1	-7.7	-7.4	ZINC000299888870	-6.9	-7.7	-7.3
ZINC000001491002	-7.2	-7.8	-7.5	ZINC000085537120	-5.7	-9.1	-7.4	ZINC000149481739	-6.7	-7.9	-7.3
ZINC000003938746	-6.5	-8.5	-7.5	ZINC000058591422	-6.9	-7.9	-7.4	ZINC000028136291	-7.3	-7.3	-7.3
ZINC000253613242	-7.4	-7.6	-7.5	ZINC000003951627	-6.1	-8.7	-7.4	ZINC000003946366	-5.8	-8.7	-7.3
ZINC000000643138	-6.7	-8.3	-7.5	ZINC000299841529	-6.1	-8.7	-7.4	ZINC000085537017	-6.3	-8.2	-7.3
ZINC000167574450	-7.7	-7.3	-7.5	ZINC000003871927	-6.4	-8.4	-7.4	ZINC000139868282	-6.8	-7.7	-7.3
ZINC000095618690	-8.2	-6.8	-7.5	ZINC000072190153	-7.0	-7.8	-7.4	ZINC000299841499	-7.6	-6.9	-7.3
ZINC000256315106	-7.0	-8.0	-7.5	ZINC000085563443	-7.3	-7.5	-7.4	ZINC000009164421	-6.5	-8.0	-7.3
ZINC000014879963	-6.7	-8.3	-7.5	ZINC000256445978	-6.9	-7.9	-7.4	ZINC000003941829	-6.8	-7.7	-7.3
ZINC000095628210	-6.0	-9.0	-7.5	ZINC000261494581	-6.3	-8.5	-7.4	ZINC000028815572	-7.2	-7.3	-7.3
ZINC000003915265	-6.9	-8.1	-7.5	ZINC000053683148	-6.6	-8.2	-7.4	ZINC000150338506	-6.2	-8.3	-7.3
ZINC000150564784	-5.6	-9.4	-7.5	ZINC000003948997	-7.1	-7.7	-7.4	ZINC000138332392	-7.6	-6.9	-7.3
ZINC000029747110	-8.5	-6.5	-7.5	ZINC000003976535	-7.7	-7.1	-7.4	ZINC000028827350	-8.1	-6.4	-7.3
ZINC000256015225	-6.3	-8.7	-7.5	ZINC000095618801	-5.6	-9.2	-7.4	ZINC000040165256	-7.3	-7.2	-7.3
ZINC000261494704	-6.4	-8.5	-7.5	ZINC000150339328	-7.8	-7.0	-7.4	ZINC000100030312	-5.7	-8.8	-7.3
ZINC000100285156	-7.2	-7.7	-7.5	ZINC000169362874	-6.0	-8.8	-7.4	ZINC000150338698	-6.6	-7.9	-7.3
ZINC000077311862	-5.7	-9.2	-7.5	ZINC000008214644	-6.7	-8.0	-7.4	ZINC000936069425	-7.3	-7.2	-7.3
ZINC000256315101	-7.0	-7.9	-7.5	ZINC000014880002	-8.9	-5.8	-7.4	ZINC000253613241	-7.3	-7.2	-7.3
ZINC000115193490	-6.8	-8.1	-7.5	ZINC000033889315	-7.6	-7.1	-7.4	ZINC000022448680	-5.7	-8.8	-7.3
ZINC000004099009	-7.1	-7.8	-7.5	ZINC000053683271	-6.4	-8.3	-7.4	ZINC000072284071	-6.2	-8.3	-7.3
ZINC000022453472	-7.6	-7.3	-7.5	ZINC000072190199	-6.1	-8.6	-7.4	ZINC000140739150	-5.4	-9.1	-7.3
ZINC000068249103	-7.0	-7.9	-7.5	ZINC000095618744	-8.1	-6.6	-7.4	ZINC000095803251	-6.2	-8.3	-7.3
ZINC000029416466	-8.0	-6.9	-7.5	ZINC000118913658	-7.2	-7.5	-7.4	ZINC000035308284	-7.7	-6.8	-7.3
ZINC000100014880	-6.7	-8.2	-7.5	ZINC000004215255	-7.4	-7.3	-7.4	ZINC000072315510	-7.6	-6.9	-7.3
ZINC000261494620	-6.9	-8.0	-7.5	ZINC000150338708	-8.1	-6.6	-7.4	ZINC000238730528	-6.7	-7.8	-7.3
ZINC000003786262	-6.4	-8.5	-7.5	ZINC000096006019	-5.9	-8.8	-7.4	ZINC000001532934	-7.9	-6.6	-7.3
ZINC000169338351	-6.6	-8.3	-7.5	ZINC000261494660	-6.6	-8.1	-7.4	ZINC000072190219	-7.9	-6.6	-7.3
ZINC000008674218	-7.6	-7.3	-7.5	ZINC000003842421	-6.8	-7.9	-7.4	ZINC000095618681	-5.8	-8.7	-7.3
ZINC000098208444	-6.8	-8.1	-7.5	ZINC000014087429	-7.7	-7.0	-7.4	ZINC000100054334	-7.2	-7.3	-7.3
ZINC000003979756	-6.3	-8.6	-7.5	ZINC000261494701	-6.8	-7.9	-7.4	ZINC000003825437	-6.5	-8.0	-7.3
ZINC000003992480	-6.8	-8.1	-7.5	ZINC000299818021	-7.9	-6.8	-7.4	ZINC000085536956	-6.7	-7.8	-7.3
ZINC000068120810	-7.8	-7.1	-7.5	ZINC000003938642	-6.3	-8.4	-7.4	ZINC000252548734	-6.7	-7.8	-7.3
ZINC000238730506	-6.9	-8.0	-7.5	ZINC000008216695	-5.7	-9.0	-7.4	ZINC000019862646	-7.3	-7.2	-7.3
ZINC000065731166	-7.2	-7.7	-7.5	ZINC000113648937	-6.7	-8.0	-7.4	ZINC000084727380	-6.7	-7.8	-7.3
ZINC000003995616	-8.8	-6.1	-7.5	ZINC000169737880	-8.3	-6.4	-7.4	ZINC000118915218	-6.7	-7.8	-7.3
ZINC000150346620	-6.8	-8.1	-7.5	ZINC000059228279	-6.5	-8.2	-7.4	ZINC000299841552	-7.0	-7.5	-7.3
ZINC000150572205	-7.4	-7.5	-7.5	ZINC000014211051	-6.6	-8.1	-7.4	ZINC000100064834	-6.4	-8.0	-7.2
ZINC000165019779	-8.8	-6.1	-7.5	ZINC000049769733	-5.7	-9.0	-7.4	ZINC000003914596	-7.7	-6.7	-7.2
ZINC000299888869	-7.1	-7.8	-7.5	ZINC000096015174	-7.1	-7.6	-7.4	ZINC000252517142	-7.3	-7.1	-7.2
ZINC000031416001	-6.4	-8.5	-7.5	ZINC000256445982	-7.5	-7.2	-7.4	ZINC000261494689	-7.2	-7.2	-7.2
ZINC000118930567	-8.4	-6.5	-7.5	ZINC000003936474	-7.2	-7.5	-7.4	ZINC000022448696	-6.3	-8.1	-7.2
ZINC000003930732	-6.7	-8.1	-7.4	ZINC000095546207	-7.7	-7.0	-7.4	ZINC000100053092	-6.2	-8.2	-7.2
ZINC000003966030	-7.7	-7.1	-7.4	ZINC000003960893	-7.2	-7.4	-7.3	ZINC000230122970	-6.9	-7.5	-7.2
ZINC000095803296	-7.4	-7.4	-7.4	ZINC000068009799	-6.0	-8.6	-7.3	ZINC000085552177	-6.0	-8.4	-7.2
ZINC000003938744	-6.9	-7.9	-7.4	ZINC000261494650	-7.3	-7.3	-7.3	ZINC000253476137	-6.5	-7.9	-7.2
ZINC000028467879	-6.9	-7.9	-7.4	ZINC000150339083	-6.2	-8.4	-7.3	ZINC000068077856	-6.1	-8.3	-7.2
ZINC000169289386	-6.5	-8.3	-7.4	ZINC000003992662	-6.6	-8.0	-7.3	ZINC000085601496	-6.6	-7.8	-7.2
ZINC000072284066	-6.8	-8.0	-7.4	ZINC000008214629	-4.4	-10.2	-7.3	ZINC000100054319	-7.3	-7.1	-7.2
ZINC000238730529	-6.5	-8.3	-7.4	ZINC000043100709	-7.6	-7.0	-7.3	ZINC000138332532	-7.4	-7.0	-7.2
ZINC000095619120	-7.4	-7.4	-7.4	ZINC000068247898	-7.4	-7.2	-7.3	ZINC000261494703	-5.8	-8.6	-7.2

Ligand (ZINC ID)	Docking scores			Ligand (ZINC ID)	Docking scores			Ligand (ZINC ID)	Docking scores		
	Vina	Kdeep	Consensus		Vina	Kdeep	Consensus		Vina	Kdeep	Consensus
ZINC000261494692	-7.5	-6.9	-7.2	ZINC000150339050	-8.3	-5.9	-7.1	ZINC000003796018	-5.9	-8.1	-7.0
ZINC000043130902	-6.4	-8.0	-7.2	ZINC000169291448	-6.6	-7.6	-7.1	ZINC000085551979	-5.9	-8.1	-7.0
ZINC000195761836	-5.7	-8.7	-7.2	ZINC000008214681	-6.3	-7.9	-7.1	ZINC000095539256	-7.4	-6.6	-7.0
ZINC000196071834	-6.5	-7.9	-7.2	ZINC000067887077	-6.0	-8.2	-7.1	ZINC000100054755	-7.5	-6.5	-7.0
ZINC000042833251	-7.1	-7.3	-7.2	ZINC000095803295	-6.4	-7.8	-7.1	ZINC000195936110	-7.6	-6.4	-7.0
ZINC000085537042	-7.1	-7.3	-7.2	ZINC000261494592	-5.9	-8.3	-7.1	ZINC000256109534	-7.6	-6.4	-7.0
ZINC000049799668	-6.6	-7.8	-7.2	ZINC000095617640	-7.2	-7.0	-7.1	ZINC000095618733	-7.3	-6.7	-7.0
ZINC000003915428	-7.3	-7.1	-7.2	ZINC000095618880	-7.3	-6.9	-7.1	ZINC000261494716	-6.8	-7.2	-7.0
ZINC000004097186	-7.3	-7.1	-7.2	ZINC000299841504	-6.8	-7.4	-7.1	ZINC000261494663	-6.4	-7.6	-7.0
ZINC000004212945	-7.0	-7.4	-7.2	ZINC000013546270	-6.7	-7.5	-7.1	ZINC000095618832	-6.3	-7.7	-7.0
ZINC000100054071	-6.6	-7.8	-7.2	ZINC000072190136	-6.3	-7.9	-7.1	ZINC000150346926	-6.8	-7.2	-7.0
ZINC000100053656	-6.5	-7.9	-7.2	ZINC000150338912	-7.5	-6.6	-7.1	ZINC000009232419	-7.3	-6.7	-7.0
ZINC000238730521	-7.9	-6.5	-7.2	ZINC000256109530	-7.7	-6.4	-7.1	ZINC000095610824	-6.8	-7.2	-7.0
ZINC000261494591	-5.9	-8.5	-7.2	ZINC000004245665	-7.1	-7.0	-7.1	ZINC000095618608	-6.7	-7.3	-7.0
ZINC000003830413	-6.4	-8.0	-7.2	ZINC000072267022	-7.1	-7.0	-7.1	ZINC000160486141	-5.9	-8.1	-7.0
ZINC000043200381	-6.3	-8.1	-7.2	ZINC000003939935	-7.0	-7.1	-7.1	ZINC000299841498	-7.7	-6.3	-7.0
ZINC000096014967	-7.0	-7.4	-7.2	ZINC000003964224	-6.8	-7.3	-7.1	ZINC000095862725	-6.5	-7.4	-7.0
ZINC000049783754	-7.2	-7.1	-7.2	ZINC000027520427	-6.7	-7.4	-7.1	ZINC000100053657	-6.8	-7.1	-7.0
ZINC000004394349	-7.1	-7.2	-7.2	ZINC000261106255	-6.3	-7.8	-7.1	ZINC000118915334	-7.1	-6.8	-7.0
ZINC000248025601	-6.4	-7.9	-7.2	ZINC000261494690	-7.3	-6.8	-7.1	ZINC000261494609	-7.0	-6.9	-7.0
ZINC000095598449	-5.7	-8.6	-7.2	ZINC000004215648	-8.3	-5.8	-7.1	ZINC000261494675	-6.5	-7.4	-7.0
ZINC000095618810	-6.0	-8.3	-7.2	ZINC000006744584	-6.7	-7.4	-7.1	ZINC000085479227	-6.6	-7.3	-7.0
ZINC000253685437	-7.5	-6.8	-7.2	ZINC000053229445	-6.2	-7.9	-7.1	ZINC000095618682	-6.0	-7.9	-7.0
ZINC000253946951	-6.9	-7.4	-7.2	ZINC000252286877	-7.8	-6.3	-7.1	ZINC000060392785	-5.8	-8.1	-7.0
ZINC000003921098	-6.9	-7.4	-7.2	ZINC000003922077	-7.1	-7.0	-7.1	ZINC000253733842	-6.6	-7.3	-7.0
ZINC000014191768	-5.6	-8.7	-7.2	ZINC000261494617	-7.1	-7.0	-7.1	ZINC000118930568	-6.7	-7.2	-7.0
ZINC000036184574	-6.4	-7.9	-7.2	ZINC000003977777	-7.9	-6.2	-7.1	ZINC000004215770	-7.1	-6.8	-7.0
ZINC000043130908	-7.0	-7.3	-7.2	ZINC000095618821	-6.7	-7.4	-7.1	ZINC000100054746	-7.2	-6.7	-7.0
ZINC000056898863	-6.1	-8.2	-7.2	ZINC000053294258	-7.6	-6.5	-7.1	ZINC000256097227	-5.2	-8.7	-7.0
ZINC000085536940	-7.0	-7.3	-7.2	ZINC000067887079	-5.6	-8.5	-7.1	ZINC000004422978	-6.1	-7.8	-7.0
ZINC000100054321	-7.4	-6.9	-7.2	ZINC000100005150	-7.6	-6.5	-7.1	ZINC000098208963	-7.0	-6.9	-7.0
ZINC000003919807	-6.8	-7.5	-7.2	ZINC000100735958	-7.6	-6.5	-7.1	ZINC000008214401	-6.3	-7.6	-7.0
ZINC000003831996	-7.2	-7.1	-7.2	ZINC000003938704	-6.8	-7.3	-7.1	ZINC000038154034	-7.3	-6.6	-7.0
ZINC000261494702	-6.4	-7.9	-7.2	ZINC000004426028	-5.9	-8.2	-7.1	ZINC000043100782	-7.0	-6.9	-7.0
ZINC000042834847	-7.7	-6.6	-7.2	ZINC000060183170	-6.4	-7.7	-7.1	ZINC000072317493	-7.0	-6.9	-7.0
ZINC000056898810	-8.2	-6.1	-7.2	ZINC000060183860	-7.5	-6.6	-7.1	ZINC000100014666	-6.4	-7.5	-7.0
ZINC000261494661	-6.6	-7.7	-7.2	ZINC000095617628	-7.1	-7.0	-7.1	ZINC000043128334	-5.9	-8.0	-7.0
ZINC000095618817	-7.8	-6.5	-7.2	ZINC000095618900	-6.3	-7.8	-7.1	ZINC000060183167	-6.2	-7.7	-7.0
ZINC000015951916	-7.1	-7.2	-7.2	ZINC000169345692	-6.0	-8.1	-7.1	ZINC000095618891	-6.8	-7.1	-7.0
ZINC000261106254	-6.1	-8.2	-7.2	ZINC000253685418	-7.1	-7.0	-7.1	ZINC000102820038	-7.0	-6.9	-7.0
ZINC000001543181	-6.9	-7.4	-7.2	ZINC000003992105	-6.7	-7.4	-7.1	ZINC000256097213	-5.0	-8.9	-7.0
ZINC000014210455	-6.2	-8.1	-7.2	ZINC000008215403	-7.2	-6.9	-7.1	ZINC000014210886	-6.4	-7.4	-6.9
ZINC000150346618	-7.3	-7.0	-7.2	ZINC000052245489	-7.3	-6.8	-7.1	ZINC000034015946	-6.0	-7.8	-6.9
ZINC000256445975	-7.1	-7.2	-7.2	ZINC000299808959	-6.0	-8.1	-7.1	ZINC000095618756	-6.9	-6.9	-6.9
ZINC000003831120	-7.7	-6.5	-7.1	ZINC000003935130	-6.8	-7.3	-7.1	ZINC000031415993	-6.3	-7.5	-6.9
ZINC000003925368	-7.5	-6.7	-7.1	ZINC000003965107	-6.5	-7.6	-7.1	ZINC000059697694	-7.6	-6.2	-6.9
ZINC000206179143	-6.0	-8.2	-7.1	ZINC000139805602	-5.8	-8.3	-7.1	ZINC000003929532	-6.1	-7.7	-6.9
ZINC000257811376	-5.7	-8.5	-7.1	ZINC000245224599	-8.0	-6.1	-7.1	ZINC000026011099	-5.8	-8.0	-6.9
ZINC000014191207	-7.5	-6.7	-7.1	ZINC000003612878	-7.5	-6.6	-7.1	ZINC000253387843	-8.0	-5.8	-6.9
ZINC000063539231	-6.9	-7.3	-7.1	ZINC000027094928	-6.0	-8.1	-7.1	ZINC000003938681	-6.3	-7.5	-6.9
ZINC000095616595	-8.0	-6.2	-7.1	ZINC000100054210	-6.8	-7.3	-7.1	ZINC000084386263	-7.3	-6.5	-6.9
ZINC000014140454	-6.8	-7.4	-7.1	ZINC000053684118	-7.0	-7.0	-7.0	ZINC000100371951	-5.6	-8.2	-6.9
ZINC000100317046	-6.9	-7.3	-7.1	ZINC000095617625	-6.9	-7.1	-7.0	ZINC000254134439	-6.5	-7.3	-6.9
ZINC000261527108	-8.0	-6.2	-7.1	ZINC000003830432	-6.9	-7.1	-7.0	ZINC000003952532	-5.8	-8.0	-6.9
ZINC000033359785	-9.3	-4.9	-7.1	ZINC000003948095	-6.7	-7.3	-7.0	ZINC000022010625	-7.1	-6.7	-6.9
ZINC000043200832	-6.9	-7.3	-7.1	ZINC000085552114	-6.6	-7.4	-7.0	ZINC000255965157	-6.1	-7.7	-6.9
ZINC000299818014	-7.7	-6.5	-7.1	ZINC000095618683	-5.8	-8.2	-7.0	ZINC000095605999	-7.0	-6.8	-6.9
ZINC000410428646	-7.1	-7.1	-7.1	ZINC000261494676	-6.9	-7.1	-7.0	ZINC000087496092	-6.6	-7.2	-6.9
ZINC000004097458	-6.5	-7.7	-7.1	ZINC000261494570	-5.6	-8.4	-7.0	ZINC000034002084	-5.9	-7.9	-6.9
ZINC000043206251	-8.6	-5.6	-7.1	ZINC000003915526	-6.6	-7.4	-7.0	ZINC000095618719	-5.8	-8.0	-6.9
ZINC000003952747	-5.9	-8.3	-7.1	ZINC000068246504	-6.7	-7.3	-7.0	ZINC000100378061	-8.2	-5.6	-6.9
ZINC000014210457	-6.3	-7.9	-7.1	ZINC000255965156	-7.2	-6.8	-7.0	ZINC000161527403	-5.3	-8.5	-6.9
ZINC000085534336	-6.1	-8.1	-7.1	ZINC000095870481	-6.8	-7.2	-7.0	ZINC000029237800	-7.0	-6.8	-6.9
ZINC000085552699	-6.3	-7.9	-7.1	ZINC000247910399	-5.9	-8.1	-7.0	ZINC000085534098	-6.4	-7.3	-6.9

Ligand (ZINC ID)	Docking scores			Ligand (ZINC ID)	Docking scores			Ligand (ZINC ID)	Docking scores		
	Vina	Kdeep	Consensus		Vina	Kdeep	Consensus		Vina	Kdeep	Consensus
ZINC000230123065	-6.2	-7.5	-6.9	ZINC000100054205	-6.8	-6.7	-6.8	ZINC000253637382	-7.9	-5.3	-6.6
ZINC000261527107	-7.9	-5.8	-6.9	ZINC000299841517	-8.0	-5.5	-6.8	ZINC000008551963	-6.5	-6.7	-6.6
ZINC000003871960	-6.4	-7.3	-6.9	ZINC000003990418	-7.4	-6.1	-6.8	ZINC000060183168	-5.6	-7.6	-6.6
ZINC000306122005	-6.2	-7.5	-6.9	ZINC000006717478	-7.3	-6.2	-6.8	ZINC000139929783	-7.8	-5.4	-6.6
ZINC000003842702	-7.2	-6.5	-6.9	ZINC000164493111	-5.9	-7.6	-6.8	ZINC000261494625	-6.6	-6.6	-6.6
ZINC000261494714	-6.8	-6.9	-6.9	ZINC000003993846	-6.4	-7.1	-6.8	ZINC000003807298	-7.8	-5.4	-6.6
ZINC000072190138	-5.9	-7.8	-6.9	ZINC000003926620	-6.5	-7.0	-6.8	ZINC000003919685	-6.8	-6.4	-6.6
ZINC000195837865	-6.1	-7.6	-6.9	ZINC000160486003	-6.5	-7.0	-6.8	ZINC000100005148	-7.0	-6.2	-6.6
ZINC000299818022	-7.8	-5.9	-6.9	ZINC000004424091	-7.1	-6.4	-6.8	ZINC000137550260	-6.4	-6.8	-6.6
ZINC000410428644	-5.7	-8.0	-6.9	ZINC000101178759	-6.1	-7.4	-6.8	ZINC000161527507	-5.4	-7.8	-6.6
ZINC000095929260	-6.7	-7.0	-6.9	ZINC000008214470	-6.9	-6.6	-6.8	ZINC000095617635	-8.3	-4.9	-6.6
ZINC000003929810	-6.7	-7.0	-6.9	ZINC000043171152	-7.9	-5.6	-6.8	ZINC000068206930	-7.5	-5.7	-6.6
ZINC000071928291	-6.0	-7.7	-6.9	ZINC000164888446	-6.7	-6.8	-6.8	ZINC000096014306	-6.1	-7.1	-6.6
ZINC000100341584	-7.9	-5.8	-6.9	ZINC000095618655	-6.5	-7.0	-6.8	ZINC000138930200	-6.8	-6.4	-6.6
ZINC000003929892	-6.6	-7.1	-6.9	ZINC000261494664	-7.8	-5.7	-6.8	ZINC000212529587	-7.1	-6.1	-6.6
ZINC000029134545	-5.5	-8.2	-6.9	ZINC000003936307	-6.9	-6.6	-6.8	ZINC000030691548	-6.0	-7.2	-6.6
ZINC000261494657	-8.0	-5.7	-6.9	ZINC000072190144	-7.5	-6.0	-6.8	ZINC000003807186	-7.6	-5.6	-6.6
ZINC000169292271	-7.9	-5.8	-6.9	ZINC000103297739	-6.6	-6.9	-6.8	ZINC000004214612	-7.9	-5.3	-6.6
ZINC000003830434	-7.3	-6.4	-6.9	ZINC000003938684	-7.4	-6.0	-6.7	ZINC000247910418	-6.0	-7.2	-6.6
ZINC000003915259	-6.8	-6.9	-6.9	ZINC000031416005	-6.5	-6.9	-6.7	ZINC000072315511	-7.3	-5.8	-6.6
ZINC000003995845	-7.2	-6.5	-6.9	ZINC000001488757	-7.4	-6.0	-6.7	ZINC000261494624	-6.5	-6.6	-6.6
ZINC000254102438	-5.8	-7.9	-6.9	ZINC000100054235	-7.5	-5.9	-6.7	ZINC000095617638	-7.1	-6.0	-6.6
ZINC000004098459	-6.7	-7.0	-6.9	ZINC000101195251	-6.6	-6.8	-6.7	ZINC000410428673	-5.3	-7.8	-6.6
ZINC000053683151	-9.0	-4.7	-6.9	ZINC000003830421	-6.6	-6.8	-6.7	ZINC000118713970	-6.5	-6.6	-6.6
ZINC000256097222	-4.9	-8.7	-6.8	ZINC000008214528	-7.1	-6.3	-6.7	ZINC000100053086	-6.1	-7.0	-6.6
ZINC000261494673	-6.7	-6.9	-6.8	ZINC000049918329	-7.3	-6.1	-6.7	ZINC000043450324	-6.5	-6.6	-6.6
ZINC000003874605	-5.3	-8.3	-6.8	ZINC000252286876	-7.2	-6.2	-6.7	ZINC000137358975	-6.1	-7.0	-6.6
ZINC000027428713	-7.5	-6.1	-6.8	ZINC000253794828	-6.7	-6.7	-6.7	ZINC000150376965	-6.6	-6.5	-6.6
ZINC000238730518	-8.3	-5.3	-6.8	ZINC000003830445	-5.9	-7.5	-6.7	ZINC000043127515	-5.7	-7.4	-6.6
ZINC000299841485	-6.3	-7.3	-6.8	ZINC000013984697	-6.0	-7.4	-6.7	ZINC000136592824	-8.0	-5.1	-6.6
ZINC000139935181	-7.9	-5.7	-6.8	ZINC000137550409	-6.8	-6.6	-6.7	ZINC000150338908	-6.9	-6.2	-6.6
ZINC000077301904	-7.7	-5.9	-6.8	ZINC000003951152	-6.8	-6.6	-6.7	ZINC000060183177	-6.5	-6.6	-6.6
ZINC000229983969	-6.2	-7.4	-6.8	ZINC000103592703	-6.5	-6.9	-6.7	ZINC000100054194	-7.0	-6.1	-6.6
ZINC000261494633	-6.6	-7.0	-6.8	ZINC000146905479	-7.4	-6.0	-6.7	ZINC000003830957	-5.1	-8.0	-6.6
ZINC000003871946	-6.5	-7.1	-6.8	ZINC000105576134	-6.4	-7.0	-6.7	ZINC000008035377	-4.9	-8.2	-6.6
ZINC000072190220	-7.9	-5.7	-6.8	ZINC000008551087	-6.3	-7.1	-6.7	ZINC000100054214	-6.2	-6.9	-6.6
ZINC000022442861	-7.7	-5.9	-6.8	ZINC000068014156	-7.8	-5.6	-6.7	ZINC000169372474	-6.7	-6.4	-6.6
ZINC000100054069	-6.2	-7.4	-6.8	ZINC000031415997	-6.0	-7.4	-6.7	ZINC000253661026	-6.4	-6.7	-6.6
ZINC000253687865	-6.4	-7.2	-6.8	ZINC000003935633	-6.6	-6.8	-6.7	ZINC000253685434	-7.2	-5.9	-6.6
ZINC000096006012	-7.8	-5.8	-6.8	ZINC000299888510	-6.4	-7.0	-6.7	ZINC000252286878	-7.2	-5.9	-6.6
ZINC000003951737	-6.5	-7.1	-6.8	ZINC000004102194	-5.9	-7.4	-6.7	ZINC000003922715	-7.5	-5.5	-6.5
ZINC000038144598	-6.3	-7.3	-6.8	ZINC000084668739	-7.9	-5.4	-6.7	ZINC000242548680	-5.4	-7.6	-6.5
ZINC000003830442	-6.7	-6.9	-6.8	ZINC000168212088	-6.6	-6.7	-6.7	ZINC000253987407	-6.1	-6.9	-6.5
ZINC000003831157	-6.8	-6.8	-6.8	ZINC000100053097	-6.0	-7.3	-6.7	ZINC000261494623	-6.6	-6.4	-6.5
ZINC000095618878	-7.7	-5.9	-6.8	ZINC000100054198	-6.8	-6.5	-6.7	ZINC000004172330	-6.3	-6.7	-6.5
ZINC000096178622	-6.6	-7.0	-6.8	ZINC000137281876	-6.4	-6.9	-6.7	ZINC000118417120	-7.1	-5.9	-6.5
ZINC000083923170	-7.3	-6.3	-6.8	ZINC000253613240	-6.0	-7.3	-6.7	ZINC000229984054	-6.0	-7.0	-6.5
ZINC000100054230	-7.6	-6.0	-6.8	ZINC000059817101	-7.0	-6.3	-6.7	ZINC000030691552	-5.8	-7.2	-6.5
ZINC000100054332	-6.9	-6.7	-6.8	ZINC000200430428	-7.9	-5.4	-6.7	ZINC000105414985	-7.1	-5.9	-6.5
ZINC000137550338	-6.5	-7.1	-6.8	ZINC000256315111	-7.0	-6.3	-6.7	ZINC000137550489	-6.6	-6.4	-6.5
ZINC000253685426	-7.5	-6.1	-6.8	ZINC000261494593	-5.5	-7.8	-6.7	ZINC000169621220	-7.5	-5.5	-6.5
ZINC000003913937	-7.4	-6.2	-6.8	ZINC000004365621	-7.1	-6.2	-6.7	ZINC000060184545	-5.8	-7.2	-6.5
ZINC000003917722	-6.7	-6.9	-6.8	ZINC000060325170	-7.3	-6.0	-6.7	ZINC000003995599	-6.1	-6.8	-6.5
ZINC000229984288	-5.5	-8.1	-6.8	ZINC000150340331	-7.7	-5.6	-6.7	ZINC000014210883	-6.6	-6.3	-6.5
ZINC000044308337	-7.1	-6.4	-6.8	ZINC000008552159	-5.5	-7.8	-6.7	ZINC000022454221	-5.7	-7.2	-6.5
ZINC000072283897	-7.1	-6.4	-6.8	ZINC000263632870	-5.4	-7.9	-6.7	ZINC000059817095	-7.1	-5.8	-6.5
ZINC000095618656	-6.5	-7.0	-6.8	ZINC000004096846	-6.6	-6.7	-6.7	ZINC000052955754	-9.0	-3.9	-6.5
ZINC000248025606	-5.5	-8.0	-6.8	ZINC000030691556	-5.8	-7.5	-6.7	ZINC000147513579	-6.8	-6.1	-6.5
ZINC000256097218	-5.0	-8.5	-6.8	ZINC000299818015	-7.1	-6.2	-6.7	ZINC000150338771	-6.0	-6.9	-6.5
ZINC000003830959	-5.0	-8.5	-6.8	ZINC000038141705	-6.7	-6.5	-6.6	ZINC000299841528	-6.0	-6.9	-6.5
ZINC000029124639	-7.6	-5.9	-6.8	ZINC000245190610	-7.1	-6.1	-6.6	ZINC000003833846	-6.0	-6.9	-6.5
ZINC000003830635	-5.7	-7.8	-6.8	ZINC000150363615	-7.5	-5.7	-6.6	ZINC000212677395	-6.2	-6.7	-6.5
ZINC000096006023	-7.3	-6.2	-6.8	ZINC000253661029	-6.2	-7.0	-6.6	ZINC000299888868	-7.3	-5.6	-6.5
ZINC000096941868	-5.9	-7.6	-6.8	ZINC000245190612	-6.9	-6.3	-6.6	ZINC000034001955	-7.3	-5.6	-6.5

Ligand (ZINC ID)	Docking scores			Ligand (ZINC ID)	Docking scores			Ligand (ZINC ID)	Docking scores		
	Vina	Kdeep	Consensus		Vina	Kdeep	Consensus		Vina	Kdeep	Consensus
ZINC000299841545	-5.8	-7.1	-6.5	ZINC000022010579	-7.2	-5.3	-6.3	ZINC000245190613	-6.8	-5.4	-6.1
ZINC000136639443	-6.4	-6.5	-6.5	ZINC000145401681	-6.9	-5.6	-6.3	ZINC000043202141	-5.9	-6.3	-6.1
ZINC000003830427	-7.2	-5.7	-6.5	ZINC000003874604	-5.2	-7.3	-6.3	ZINC000091302266	-6.9	-5.3	-6.1
ZINC000118913649	-7.0	-5.9	-6.5	ZINC000299841527	-6.0	-6.5	-6.3	ZINC000100374472	-7.2	-5.0	-6.1
ZINC000255991346	-6.9	-6.0	-6.5	ZINC000140063261	-7.6	-4.9	-6.3	ZINC000003870129	-5.3	-6.9	-6.1
ZINC000169372473	-6.4	-6.4	-6.4	ZINC000003955058	-7.4	-5.1	-6.3	ZINC000096309558	-6.0	-6.2	-6.1
ZINC000029212828	-6.8	-6.0	-6.4	ZINC000043177324	-6.6	-5.9	-6.3	ZINC000003830441	-7.0	-5.2	-6.1
ZINC000060183173	-5.7	-7.1	-6.4	ZINC000003873832	-5.9	-6.6	-6.3	ZINC000095618747	-6.3	-5.9	-6.1
ZINC000096014307	-6.2	-6.6	-6.4	ZINC000022447798	-4.9	-7.6	-6.3	ZINC000096014304	-6.6	-5.6	-6.1
ZINC000100054749	-7.9	-4.9	-6.4	ZINC000035077050	-6.6	-5.9	-6.3	ZINC000004215234	-6.5	-5.7	-6.1
ZINC000256445970	-6.9	-5.9	-6.4	ZINC000100052151	-6.5	-6.0	-6.3	ZINC000003918145	-6.1	-6.0	-6.1
ZINC000299841516	-7.9	-4.9	-6.4	ZINC000011616852	-7.6	-4.9	-6.3	ZINC000004261765	-7.2	-4.9	-6.1
ZINC000072693284	-6.4	-6.4	-6.4	ZINC000096270862	-5.8	-6.7	-6.3	ZINC000008214413	-5.2	-6.9	-6.1
ZINC000118913648	-7.0	-5.8	-6.4	ZINC000118930569	-6.3	-6.2	-6.3	ZINC000003830960	-4.6	-7.5	-6.1
ZINC000004097185	-6.7	-6.1	-6.4	ZINC000003938759	-7.5	-5.0	-6.3	ZINC000169621223	-7.5	-4.6	-6.1
ZINC000256079356	-7.4	-5.4	-6.4	ZINC000043196550	-6.5	-6.0	-6.3	ZINC000196037206	-5.7	-6.4	-6.1
ZINC000072190174	-5.5	-7.3	-6.4	ZINC000095618691	-7.6	-4.9	-6.3	ZINC000003930376	-6.0	-6.1	-6.1
ZINC000169372472	-6.2	-6.6	-6.4	ZINC000205877056	-6.5	-6.0	-6.3	ZINC000003935423	-6.2	-5.9	-6.1
ZINC000253613243	-7.4	-5.4	-6.4	ZINC000206181179	-5.3	-7.1	-6.2	ZINC000261494715	-7.2	-4.9	-6.1
ZINC000004097476	-5.3	-7.5	-6.4	ZINC000261494566	-7.0	-5.4	-6.2	ZINC000253617708	-5.8	-6.3	-6.1
ZINC000261527196	-7.0	-5.8	-6.4	ZINC000030731084	-7.1	-5.3	-6.2	ZINC000169660599	-5.7	-6.4	-6.1
ZINC000013679213	-6.3	-6.5	-6.4	ZINC000255962815	-7.4	-5.0	-6.2	ZINC000003830933	-5.1	-7.0	-6.1
ZINC000085537026	-5.6	-7.2	-6.4	ZINC000299841486	-6.4	-6.0	-6.2	ZINC000003830993	-5.8	-6.3	-6.1
ZINC000030691561	-5.7	-7.1	-6.4	ZINC000003830276	-4.7	-7.7	-6.2	ZINC000003830999	-6.1	-6.0	-6.1
ZINC000053682936	-7.1	-5.7	-6.4	ZINC000008035395	-5.1	-7.3	-6.2	ZINC000043203165	-7.3	-4.8	-6.1
ZINC000003811810	-7.2	-5.5	-6.4	ZINC000079216653	-6.7	-5.7	-6.2	ZINC000008214662	-4.1	-8.0	-6.1
ZINC000043170287	-6.0	-6.7	-6.4	ZINC000095617677	-6.5	-5.9	-6.2	ZINC000196037215	-5.3	-6.8	-6.1
ZINC000003830994	-5.7	-7.0	-6.4	ZINC000248025612	-5.9	-6.5	-6.2	ZINC000256079354	-7.3	-4.7	-6.0
ZINC000006920404	-5.8	-6.9	-6.4	ZINC000095618609	-7.1	-5.3	-6.2	ZINC000003938624	-6.1	-5.9	-6.0
ZINC000028957444	-7.3	-5.4	-6.4	ZINC000253617704	-5.9	-6.5	-6.2	ZINC000004099050	-7.0	-5.0	-6.0
ZINC000095618803	-6.2	-6.5	-6.4	ZINC000261494612	-6.8	-5.6	-6.2	ZINC000030731261	-5.8	-6.2	-6.0
ZINC000140739334	-5.7	-7.0	-6.4	ZINC000150340720	-4.7	-7.7	-6.2	ZINC000085540215	-5.2	-6.8	-6.0
ZINC000003874606	-5.5	-7.2	-6.4	ZINC000003831116	-5.4	-7.0	-6.2	ZINC000003830961	-5.0	-7.0	-6.0
ZINC000008220909	-6.9	-5.8	-6.4	ZINC000299818007	-5.9	-6.4	-6.2	ZINC000008214407	-4.6	-7.4	-6.0
ZINC000003917708	-6.4	-6.3	-6.4	ZINC000003830944	-5.1	-7.2	-6.2	ZINC000248025593	-6.0	-6.0	-6.0
ZINC000252286875	-7.2	-5.5	-6.4	ZINC000163535243	-7.8	-4.5	-6.2	ZINC000001654736	-6.8	-5.2	-6.0
ZINC000255991345	-5.9	-6.8	-6.4	ZINC000073488511	-7.3	-5.0	-6.2	ZINC000049918330	-6.8	-5.2	-6.0
ZINC000003830947	-5.1	-7.6	-6.4	ZINC000253633751	-7.1	-5.2	-6.2	ZINC000095564694	-5.3	-6.7	-6.0
ZINC000004824235	-7.1	-5.6	-6.4	ZINC000100053665	-5.9	-6.4	-6.2	ZINC000056898832	-5.9	-6.1	-6.0
ZINC000001536124	-6.6	-6.1	-6.4	ZINC000255975179	-7.4	-4.9	-6.2	ZINC000263621850	-5.4	-6.6	-6.0
ZINC000003914388	-7.2	-5.5	-6.4	ZINC000238730520	-7.3	-5.0	-6.2	ZINC000008214585	-6.0	-6.0	-6.0
ZINC000299804398	-6.0	-6.7	-6.4	ZINC000253617706	-6.0	-6.3	-6.2	ZINC000212677333	-5.6	-6.4	-6.0
ZINC000003830428	-6.8	-5.9	-6.4	ZINC000685933067	-7.3	-5.0	-6.2	ZINC000072178696	-7.4	-4.6	-6.0
ZINC000004212626	-6.8	-5.9	-6.4	ZINC000169736889	-5.4	-6.9	-6.2	ZINC000238730505	-6.2	-5.8	-6.0
ZINC000100716042	-6.7	-6.0	-6.4	ZINC000077293241	-6.1	-6.2	-6.2	ZINC000095618735	-6.3	-5.6	-6.0
ZINC000085552312	-5.9	-6.7	-6.3	ZINC000096006041	-5.3	-7.0	-6.2	ZINC000014879972	-7.0	-4.9	-6.0
ZINC000161527636	-5.2	-7.4	-6.3	ZINC000150339413	-5.0	-7.3	-6.2	ZINC000014879975	-6.2	-5.7	-6.0
ZINC000253617699	-6.2	-6.4	-6.3	ZINC000003812144	-6.4	-5.9	-6.2	ZINC000028108825	-6.1	-5.8	-6.0
ZINC000253675861	-5.9	-6.7	-6.3	ZINC000003972069	-5.9	-6.4	-6.2	ZINC000095862733	-7.8	-4.1	-6.0
ZINC000003989256	-6.7	-5.9	-6.3	ZINC000005706503	-7.0	-5.3	-6.2	ZINC000008674217	-7.5	-4.4	-6.0
ZINC000008214483	-5.9	-6.7	-6.3	ZINC000261494618	-6.2	-6.1	-6.2	ZINC000068246816	-7.3	-4.6	-6.0
ZINC000043131754	-5.5	-7.1	-6.3	ZINC000034893919	-6.0	-6.3	-6.2	ZINC000003944268	-5.5	-6.4	-6.0
ZINC000263632871	-4.8	-7.8	-6.3	ZINC000008674216	-7.4	-4.8	-6.1	ZINC000169621215	-7.2	-4.7	-6.0
ZINC000003781623	-6.9	-5.7	-6.3	ZINC000014210876	-5.9	-6.3	-6.1	ZINC000261494674	-7.3	-4.6	-6.0
ZINC000137030541	-6.4	-6.2	-6.3	ZINC000096077628	-5.8	-6.4	-6.1	ZINC000003929022	-5.4	-6.5	-6.0
ZINC000137524101	-7.5	-5.1	-6.3	ZINC000035328520	-6.4	-5.8	-6.1	ZINC000004098458	-6.4	-5.5	-6.0
ZINC000003917540	-6.8	-5.8	-6.3	ZINC000095749871	-7.2	-5.0	-6.1	ZINC000238730530	-6.9	-5.0	-6.0
ZINC000196084258	-7.4	-5.2	-6.3	ZINC000003830943	-4.9	-7.3	-6.1	ZINC000003831000	-5.9	-5.9	-5.9
ZINC000009575047	-5.7	-6.9	-6.3	ZINC000003918134	-6.6	-5.6	-6.1	ZINC000095617627	-6.4	-5.4	-5.9
ZINC000095618755	-6.5	-6.1	-6.3	ZINC000008674215	-7.5	-4.7	-6.1	ZINC000100053670	-6.1	-5.7	-5.9
ZINC000014192433	-7.5	-5.1	-6.3	ZINC000095618736	-6.4	-5.8	-6.1	ZINC000161527281	-5.7	-6.1	-5.9
ZINC000003938850	-7.6	-5.0	-6.3	ZINC000238730507	-6.2	-6.0	-6.1	ZINC000003917388	-7.3	-4.5	-5.9
ZINC000095615286	-5.1	-7.5	-6.3	ZINC000095618748	-6.5	-5.7	-6.1	ZINC000014950391	-7.4	-4.4	-5.9
ZINC000004836283	-7.3	-5.2	-6.3	ZINC000100074252	-7.1	-5.1	-6.1	ZINC000100053660	-6.6	-5.2	-5.9

Ligand (ZINC ID)	Docking scores			Ligand (ZINC ID)	Docking scores			Ligand (ZINC ID)	Docking scores		
	Vina	Kdeep	Consensus		Vina	Kdeep	Consensus		Vina	Kdeep	Consensus
ZINC000049694463	-6.7	-5.1	-5.9	ZINC000143736826	-6.3	-5.0	-5.7	ZINC000008214414	-5.0	-5.6	-5.3
ZINC000004393164	-5.3	-6.5	-5.9	ZINC000008552164	-4.7	-6.6	-5.7	ZINC000033965961	-5.5	-5.1	-5.3
ZINC000026295482	-6.4	-5.3	-5.9	ZINC000017545546	-7.4	-3.9	-5.7	ZINC000085540223	-4.9	-5.6	-5.3
ZINC000095618734	-5.9	-5.8	-5.9	ZINC000685933068	-6.3	-5.0	-5.7	ZINC000299818008	-5.4	-5.1	-5.3
ZINC000068150640	-5.5	-6.2	-5.9	ZINC000003830931	-5.2	-6.0	-5.6	ZINC000021982937	-5.5	-5.0	-5.3
ZINC000072190137	-6.3	-5.4	-5.9	ZINC000003830962	-4.8	-6.4	-5.6	ZINC000256315095	-6.7	-3.8	-5.3
ZINC000095618775	-7.3	-4.4	-5.9	ZINC000261494717	-6.7	-4.5	-5.6	ZINC000261494648	-7.3	-3.2	-5.3
ZINC000064622163	-5.5	-6.2	-5.9	ZINC000299888509	-7.1	-4.1	-5.6	ZINC000085540178	-5.9	-4.5	-5.2
ZINC000199509587	-6.1	-5.6	-5.9	ZINC000169304823	-5.8	-5.4	-5.6	ZINC000256787842	-4.6	-5.8	-5.2
ZINC000014114502	-5.5	-6.2	-5.9	ZINC000238730519	-7.0	-4.2	-5.6	ZINC000077286494	-6.8	-3.6	-5.2
ZINC000026981703	-5.8	-5.9	-5.9	ZINC000022851765	-5.6	-5.5	-5.6	ZINC000096006016	-6.1	-4.3	-5.2
ZINC000261494569	-6.3	-5.4	-5.9	ZINC000299872478	-6.8	-4.3	-5.6	ZINC000011525623	-5.4	-5.0	-5.2
ZINC000261494662	-6.8	-4.9	-5.9	ZINC000014880013	-6.3	-4.8	-5.6	ZINC000085555528	-6.4	-4.0	-5.2
ZINC000003831595	-5.0	-6.6	-5.8	ZINC000008217411	-5.9	-5.1	-5.5	ZINC000008143866	-4.9	-5.5	-5.2
ZINC000014880004	-7.2	-4.4	-5.8	ZINC000199516791	-5.4	-5.6	-5.5	ZINC000334138264	-6.7	-3.6	-5.2
ZINC000003831594	-5.1	-6.5	-5.8	ZINC000299818006	-5.1	-5.9	-5.5	ZINC000008445713	-5.0	-5.3	-5.2
ZINC000685933137	-6.8	-4.8	-5.8	ZINC000085552271	-7.1	-3.9	-5.5	ZINC000003830946	-4.9	-5.4	-5.2
ZINC000004217580	-5.8	-5.8	-5.8	ZINC000084726167	-7.8	-3.2	-5.5	ZINC000008552163	-5.0	-5.3	-5.2
ZINC000004097460	-6.3	-5.3	-5.8	ZINC000028815574	-6.7	-4.3	-5.5	ZINC000150339323	-5.1	-5.2	-5.2
ZINC000100053667	-6.1	-5.5	-5.8	ZINC000140056542	-5.9	-5.1	-5.5	ZINC000261494647	-6.0	-4.2	-5.1
ZINC000014768621	-6.9	-4.7	-5.8	ZINC000238730526	-6.4	-4.5	-5.5	ZINC000096006021	-6.1	-4.1	-5.1
ZINC000150339412	-4.5	-7.1	-5.8	ZINC000261494631	-6.1	-4.8	-5.5	ZINC000008552165	-4.5	-5.6	-5.1
ZINC000004099164	-5.3	-6.3	-5.8	ZINC000410428667	-6.4	-4.5	-5.5	ZINC000195932745	-5.5	-4.6	-5.1
ZINC000014209964	-8.1	-3.5	-5.8	ZINC000229984031	-5.7	-5.2	-5.5	ZINC000095618802	-5.9	-4.1	-5.0
ZINC000022448097	-6.0	-5.5	-5.8	ZINC000008143723	-5.5	-5.4	-5.5	ZINC000215581115	-4.7	-5.3	-5.0
ZINC000100054074	-6.1	-5.4	-5.8	ZINC000003830945	-4.8	-6.0	-5.4	ZINC000004095814	-4.9	-5.0	-5.0
ZINC000004217203	-6.5	-5.0	-5.8	ZINC000003979512	-7.2	-3.6	-5.4	ZINC000085540219	-5.1	-4.8	-5.0
ZINC000096014305	-6.3	-5.2	-5.8	ZINC000003830950	-4.9	-5.9	-5.4	ZINC000085599303	-6.4	-3.5	-5.0
ZINC000100053090	-6.2	-5.3	-5.8	ZINC000003833858	-6.5	-4.3	-5.4	ZINC000215581164	-5.0	-4.9	-5.0
ZINC000299818005	-5.0	-6.5	-5.8	ZINC000004215466	-7.4	-3.4	-5.4	ZINC000004217406	-5.7	-4.2	-5.0
ZINC000230122748	-6.1	-5.4	-5.8	ZINC000003830958	-4.9	-5.9	-5.4	ZINC000238730525	-5.6	-4.3	-5.0
ZINC000003830932	-4.9	-6.5	-5.7	ZINC000003830949	-4.9	-5.8	-5.4	ZINC000247910405	-6.1	-3.6	-4.9
ZINC000003988394	-6.1	-5.3	-5.7	ZINC000085540244	-5.5	-5.2	-5.4	ZINC000195988310	-6.3	-3.4	-4.9
ZINC000247910383	-6.3	-5.1	-5.7	ZINC000150340729	-4.9	-5.8	-5.4	ZINC000150485244	-5.5	-4.2	-4.9
ZINC000150338767	-6.2	-5.2	-5.7	ZINC000238730527	-5.9	-4.8	-5.4	ZINC000261494571	-5.3	-4.2	-4.8
ZINC000299872477	-6.8	-4.6	-5.7	ZINC000238730524	-5.9	-4.8	-5.4	ZINC000008143864	-4.5	-4.9	-4.7
ZINC000004217265	-6.2	-5.2	-5.7	ZINC000011525622	-5.3	-5.4	-5.4	ZINC000005822389	-4.9	-4.5	-4.7
ZINC000206413987	-6.3	-5.1	-5.7	ZINC000261494649	-7.1	-3.6	-5.4	ZINC000103591702	-6.1	-3.1	-4.6
ZINC000238730522	-7.2	-4.2	-5.7	ZINC000004216615	-5.2	-5.5	-5.4	ZINC000101687674	-5.2	-3.9	-4.6
ZINC000043177322	-6.0	-5.3	-5.7	ZINC000150340281	-7.1	-3.6	-5.4	ZINC000150369722	-4.9	-3.6	-4.3
ZINC000085537051	-5.7	-5.6	-5.7	ZINC000008552162	-4.6	-6.0	-5.3	ZINC000008214418	-4.5	-4.0	-4.3
ZINC000014806497	-7.2	-4.1	-5.7	ZINC000299872476	-6.8	-3.8	-5.3	ZINC000150339603	-4.5	-3.7	-4.1

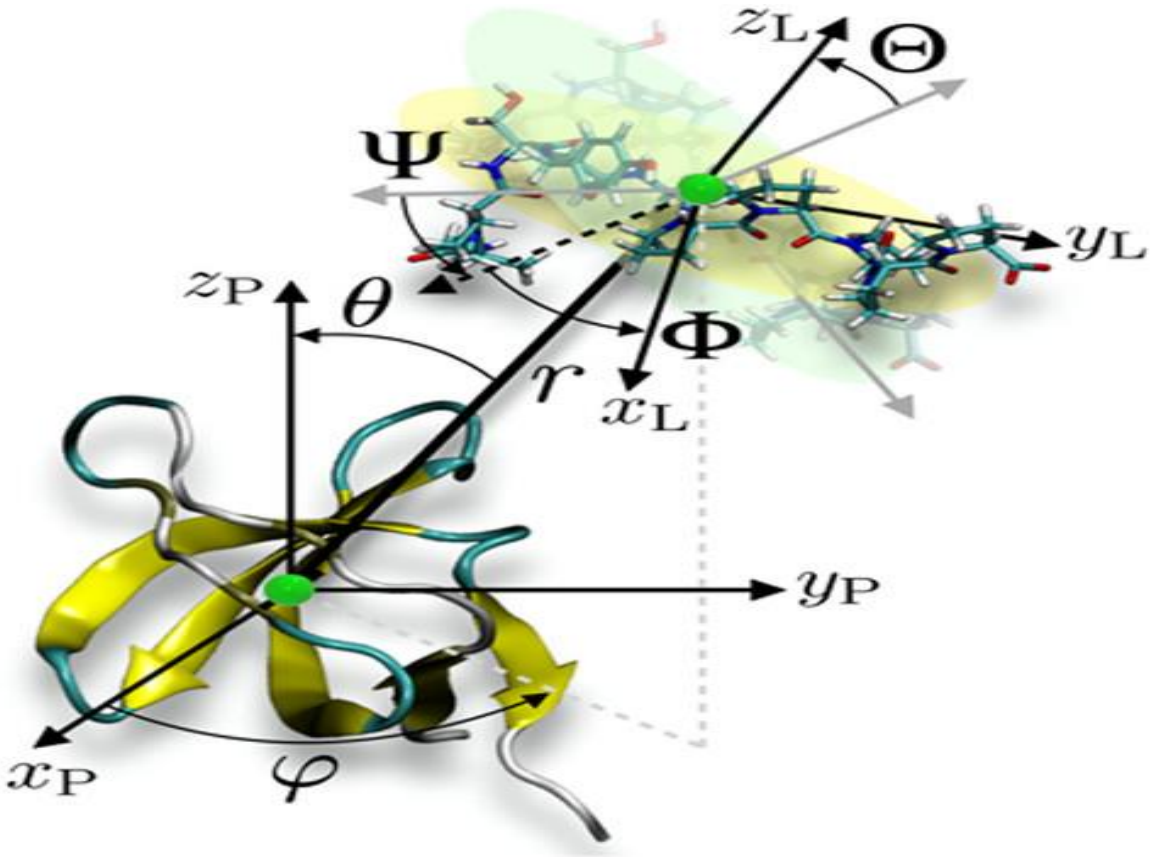

Figure C.1: Degrees of freedom used in the absolute binding energy protocol. Θ, Φ, and Ψ represent the Euler angles, and θ, φ, and r are the spherical coordinates. The ligand conformation is determined by the RMSD distance with respect to its equilibrated reference structure of the protein–ligand complex. Adapted with permission from (*J. Chem. Theory Comput.* 2017, 13, 11, 5173–5178). Copyright (2017) American Chemical Society.

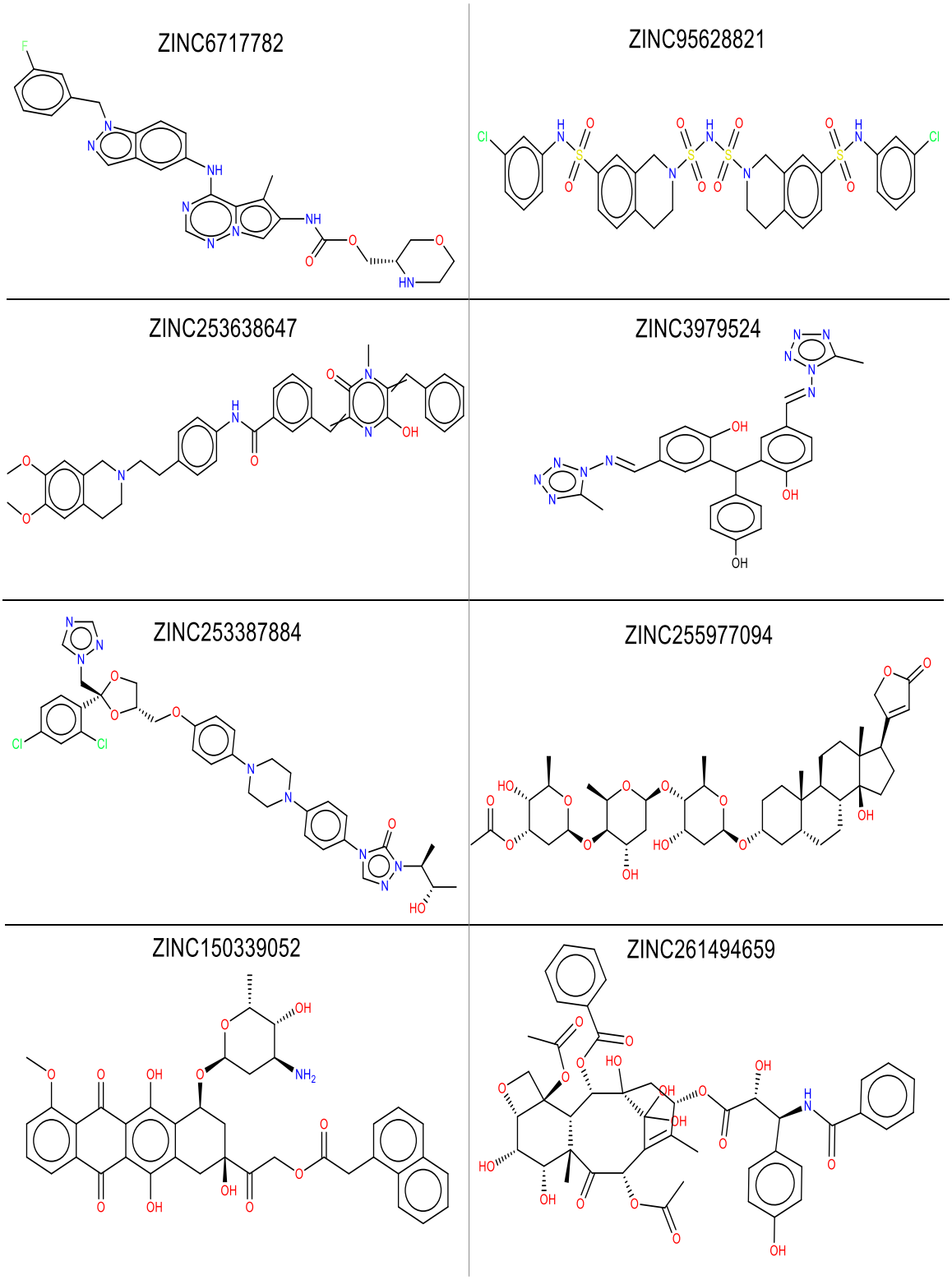

Figure C.2: Two-dimensional structures of selected compounds with the highest spike RBD binding affinity resulting from the molecular docking.

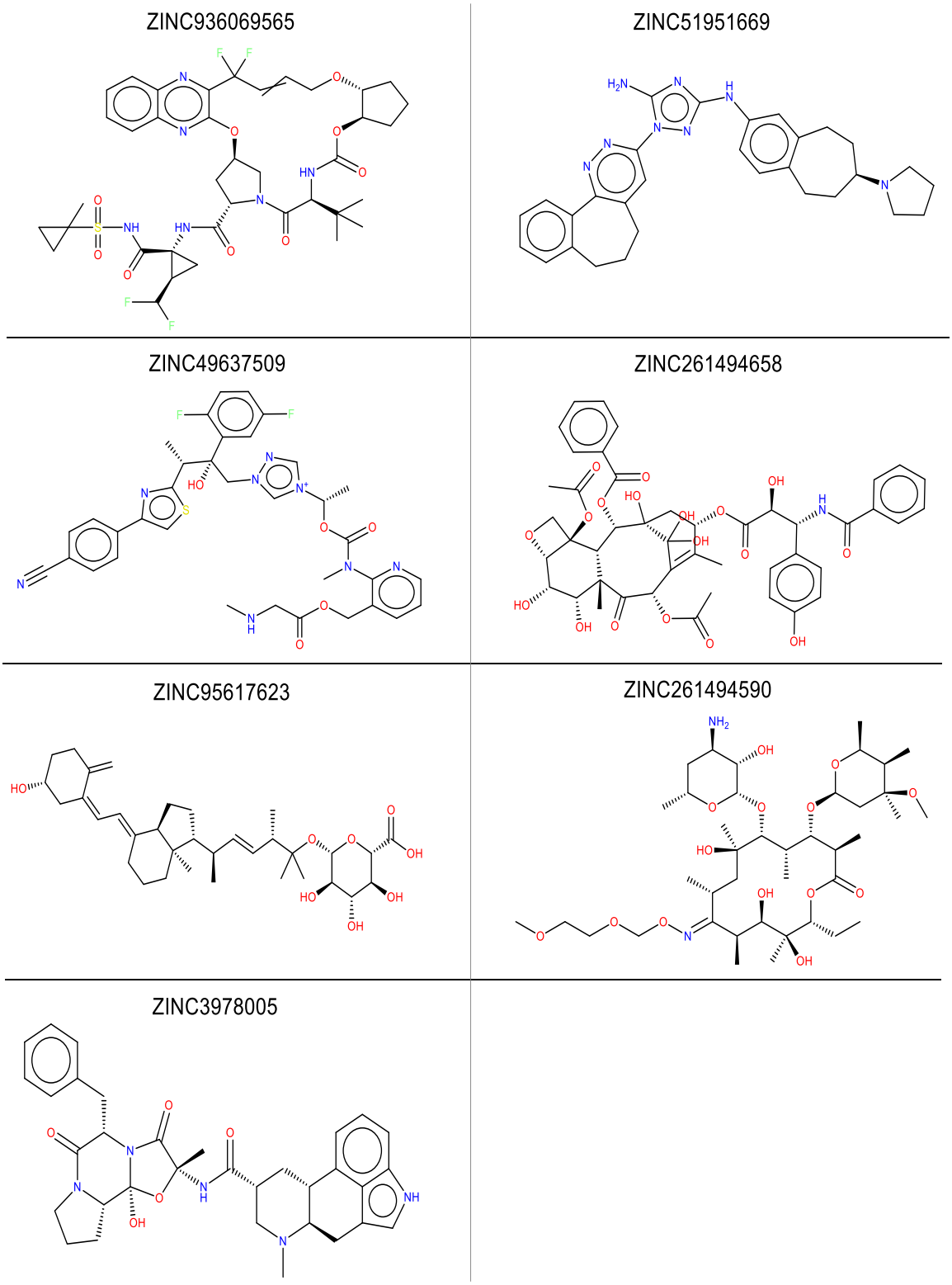

Figure C.3: Two-dimensional structures of selected compounds with the highest spike RBD binding affinity resulting from the molecular docking.

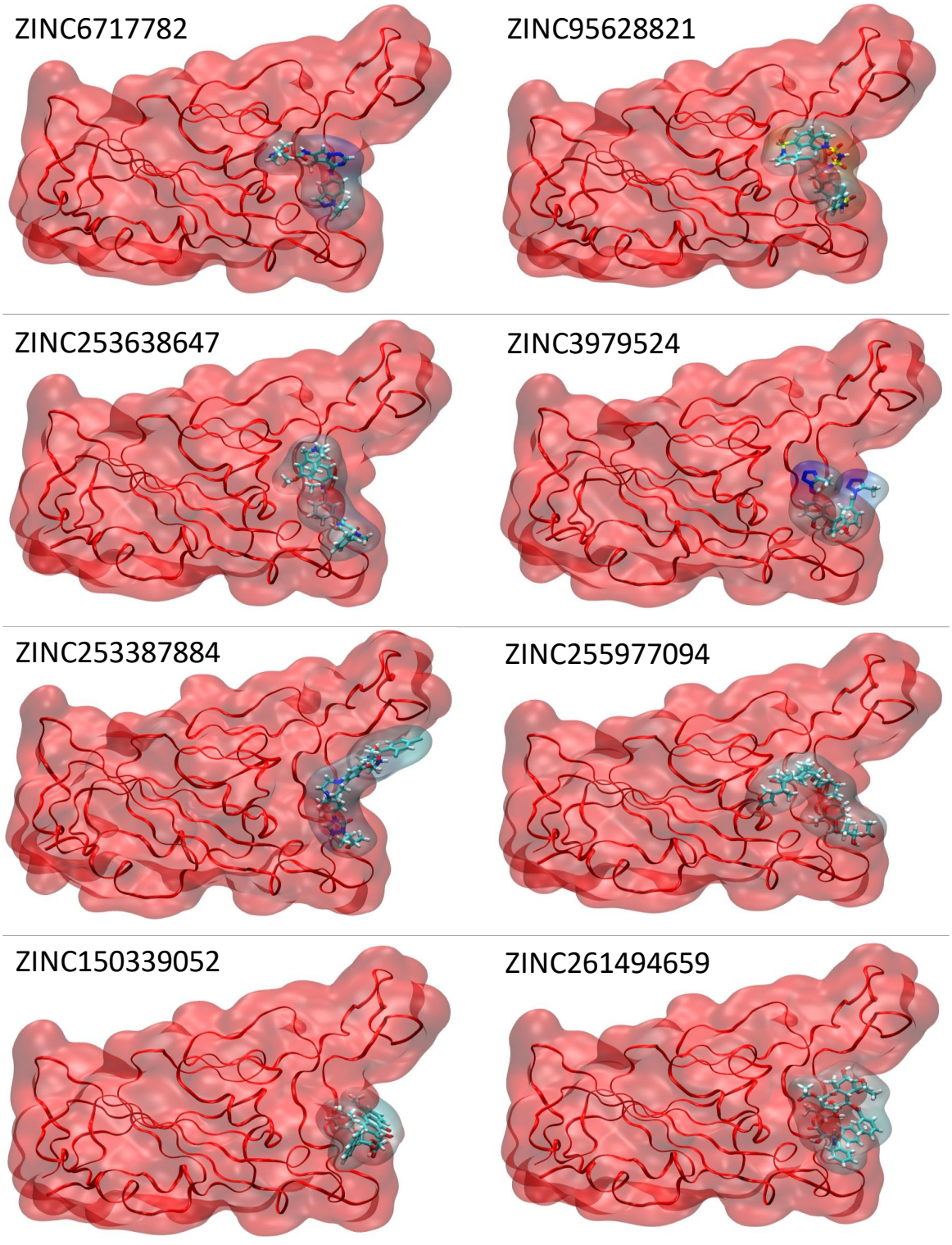

Figure C.4: Three-dimensional docked conformations of selected compounds with the highest spike RBD binding affinity resulting from the molecular docking.

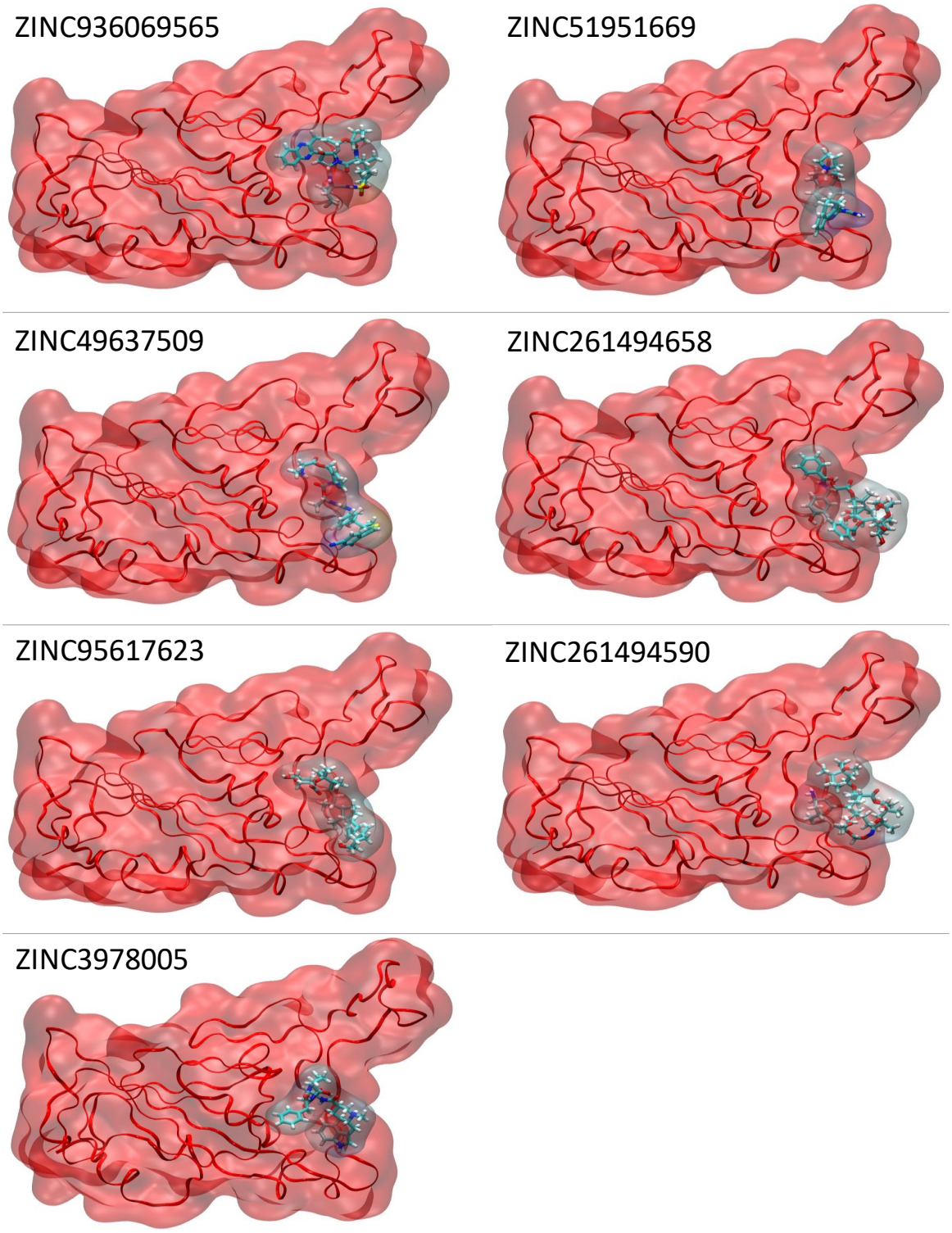

Figure C.5: Three-dimensional docked conformations of selected compounds with the highest spike RBD binding affinity resulting from the molecular docking.

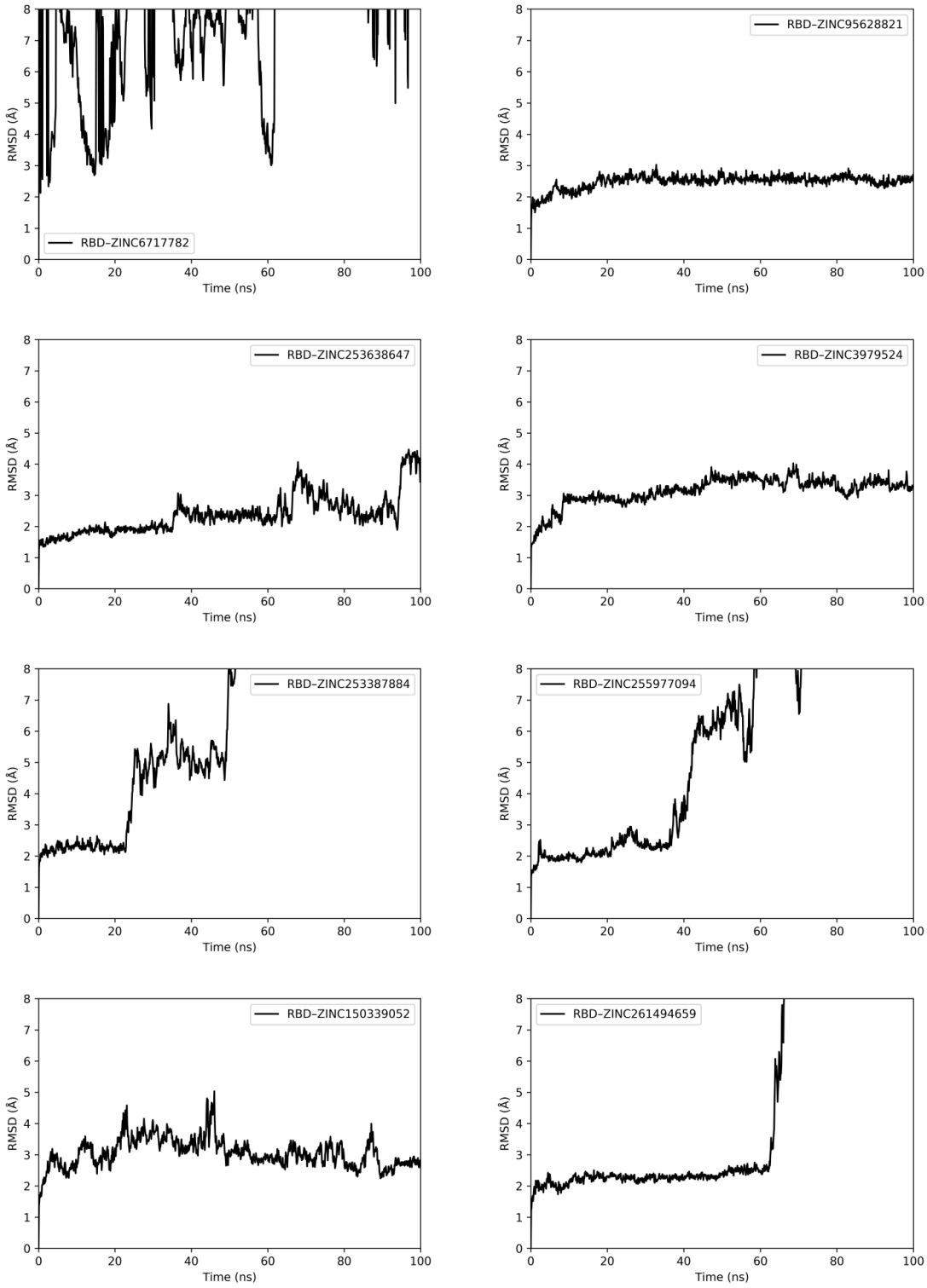

Figure C.6: RMSD results of the spike RBD-ligand complexes during 100 ns MD simulations.

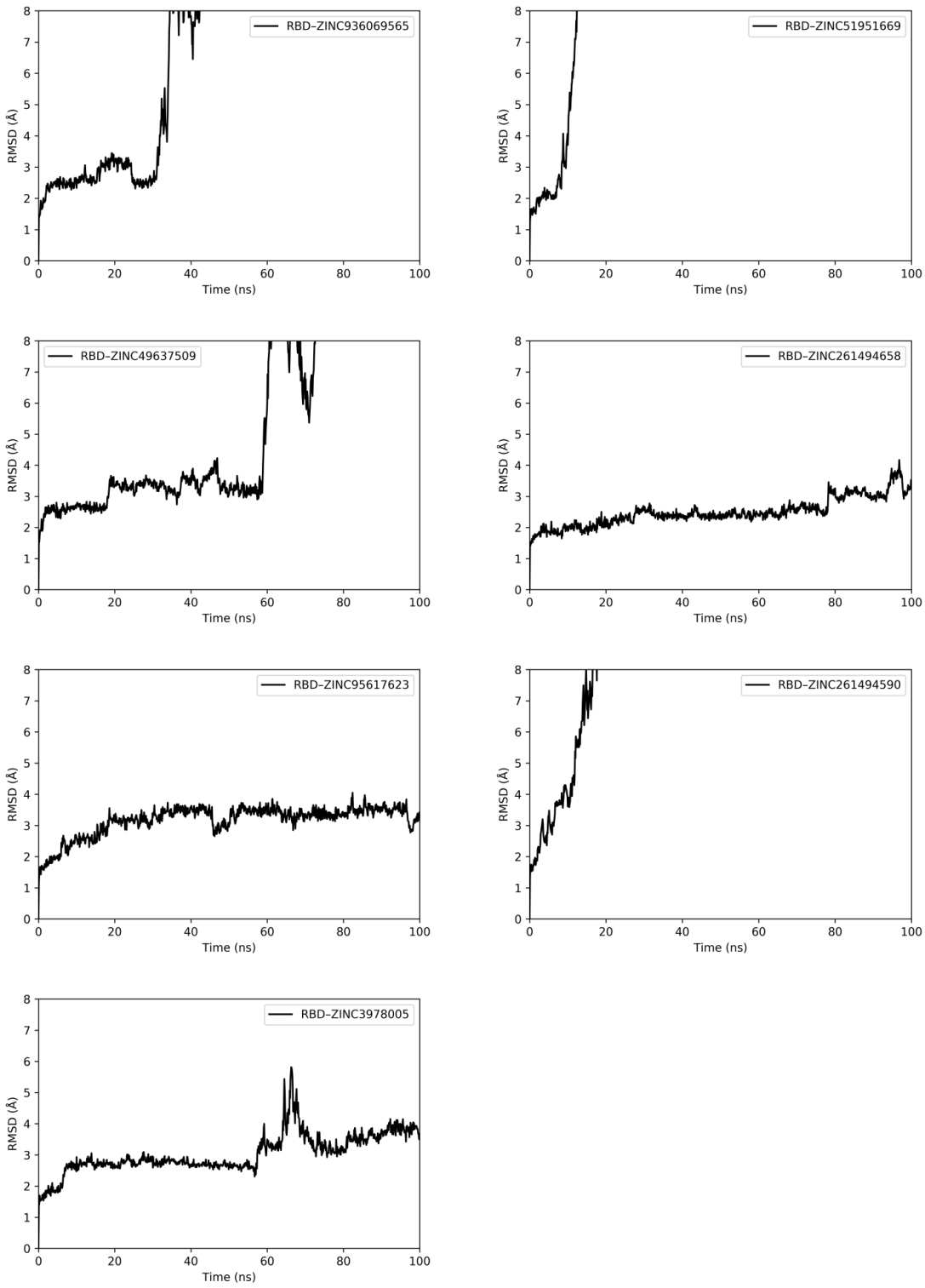

Figure C.7: RMSD results of the spike RBD-ligand complexes during 100 ns MD simulations.

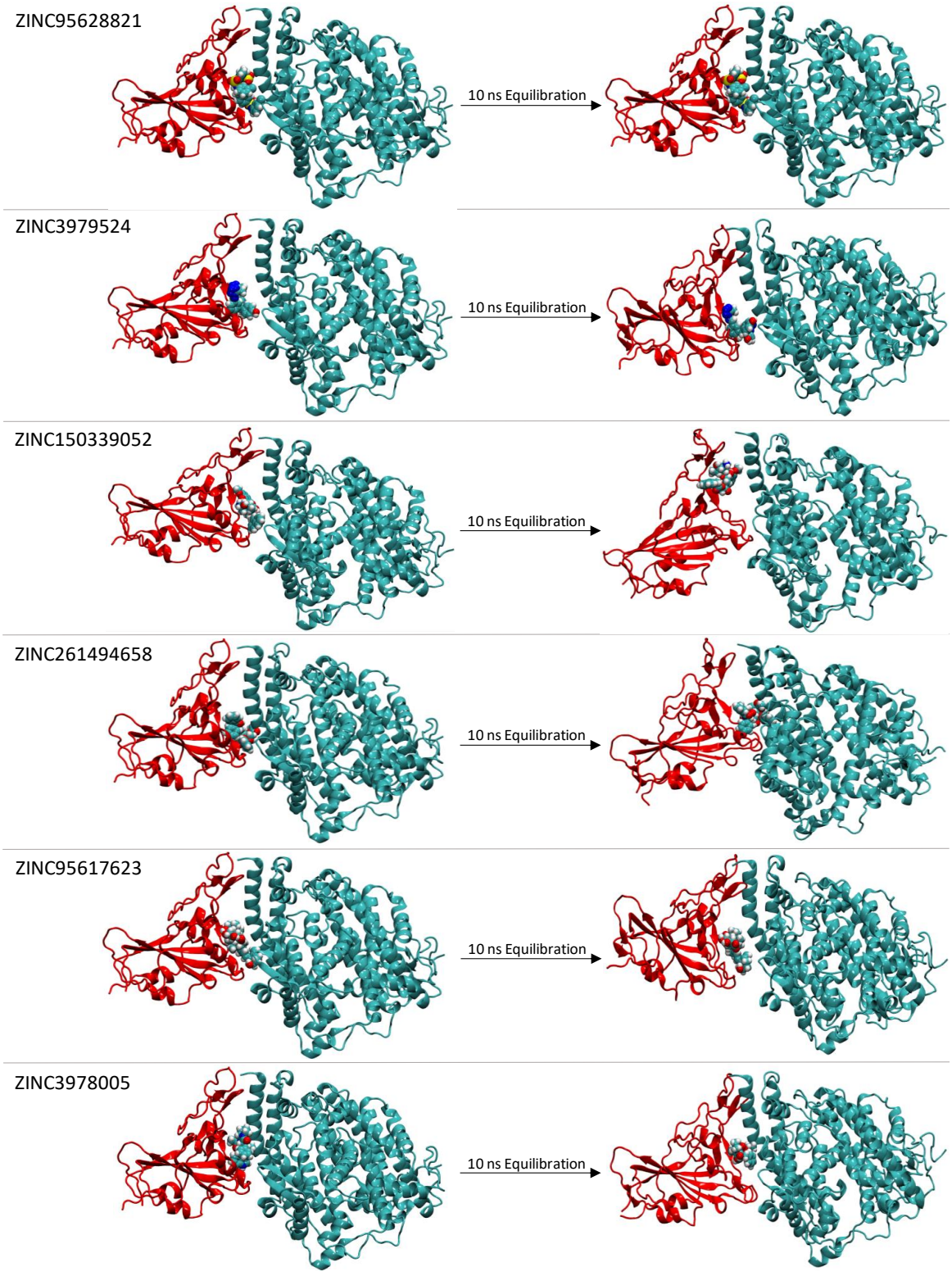

Figure C.8: RMSD results of the spike RBD-ligand complexes during 100 ns MD simulations.